

**The dynamics of transforming charges into chemical bonds at the solid-liquid interface**

by

Xihan Chen

A dissertation submitted in partial satisfaction of the  
requirements for the degree of

Doctor of Philosophy

in

Chemistry

in the

Graduate Division

of the

University of California, Berkeley

Committee in charge:

Assistant Professor Tanja Cuk, Chair

Professor Richard Saykally

Professor Ali Javey

Summer 2017

**The dynamics of transforming charges into chemical bonds at solid-liquid interface**

Copyright 2017  
by  
Xihan Chen

The dissertation of Xihan Chen, titled the dynamics of transforming charges into chemical bonds at solid-liquid interface, is approved by:

Chair \_\_\_\_\_ Date \_\_\_\_\_

\_\_\_\_\_ Date \_\_\_\_\_

\_\_\_\_\_ Date \_\_\_\_\_

University of California, Berkeley

## Abstract

### **The dynamics of transforming charges into chemical bonds at solid-liquid interface**

by

Xihan Chen

Doctor of Philosophy in Chemistry

University of California, Berkeley

Assistant Professor Tanja Cuk, Chair

How charges transform chemical bonds at the solid-liquid interface is at the heart of energy storage technologies today. In these technologies, electrical charges transform into an energy dense product. At this interface, the transformation process happens by localizing photogenerated charges in radical forms at ultrafast time scale. Later in the microsecond time scale, the generated radicals react with liquid to form new chemical bonds and complete catalytic cycle. The goal is to dynamically deconstruct the mechanism of this process. To do that, lots of areas of chemistry such as electrochemistry, inorganic chemistry and spectroscopy have to be combined.

In this dissertation, I focused on studying charge (hole) dynamics in heterogenous water oxidation reaction, which is crucial in renewable energy application, at n-SrTiO<sub>3</sub>/aqueous interface. Several methods including ultrafast optical spectroscopy, ultrafast infrared spectroscopy and microsecond optical spectroscopy are applied to investigate how photogenerated holes transform water into oxygen gas.

In ultrafast time scale, by applying an ultrafast near infrared probe (800 nm) to isolate intra-band transitions, the dynamics of holes transfer from valance band to surface is revealed. By applying an ultrafast infrared probe to isolate interfacial vibrations and a sub band-gap probe (400 nm and white light) to isolate the mid-gap transitions, the initial formation dynamics of radicals are identified. Together with theoretical calculation, the initial formation dynamics, with a  $1.3 \pm 0.2$  ps time constant, is assigned to two radical classes, the titanium oxyl (Ti-O•) which has been assigned through sub-surface vibration at 800 cm<sup>-1</sup> and the in-plane bridge radical

(Ti-O•-Ti) which has been assigned through its in-plane optical transition dipole. Interestingly, time constants of 1.3 ps is characteristic of hydroxyl stretch relaxation in H-bonded water network, indicating stabilization of radicals by hydrogen bonding.

In microsecond time scale, by applying a sub band-gap probe (400 nm) to isolate the mid-gap transitions, the dynamics of radicals transforming into new chemical bond are found to involve two distinctive processes. The fast process is mainly affected by solution ionic strength. The slower process also has an H/D isotope effect with D lengthened the reaction rate constant.

Together, these works provide vital information towards understanding how charges transform chemical bonds at the solid-liquid interface.

To my loving parents and my great wife

# Table of content

<b>Acknowledgements .....</b>	<b>iv</b>
<b>Chapter 1 Introduction.....</b>	<b>1</b>
1.1 Artificial photosynthesis .....	1
1.2 Semiconductor photoelectrode.....	3
1.3 Overview .....	4
<b>Chapter 2 Experimental techniques.....</b>	<b>5</b>
2.1 Time-resolved laser spectroscopy .....	5
2.2 Photoelectrochemistry.....	6
2.3 Other characterization techniques .....	7
<b>Chapter 3 Photocarrier dynamics and surface potential of n-SrTiO<sub>3</sub>.....</b>	<b>8</b>
3.1 Introduction .....	8
3.2 Experimental configuration.....	10
3.3 Results .....	13
3.3.1 Optical properties of SrTiO <sub>3</sub> .....	13
3.3.2 Electrochemical properties of n-SrTiO <sub>3</sub> .....	14
3.3.3 Photoelectrochemical properties of n-SrTiO <sub>3</sub> – Shifting energy band position with applied voltage.....	16
3.3.4 Charge transfer reaction on n-SrTiO <sub>3</sub> – Open circuit kinetics of interfacial hole transfer .....	21
3.3.5 Charge transfer reaction on n-SrTiO <sub>3</sub> – Kinetics of interfacial hole transfer as a function of overpotential .....	24
3.4 Discussion .....	29
3.5 Conclusion.....	31
<b>Chapter 4 Probing initial intermediates of water oxidation on n-SrTiO<sub>3</sub> with vibrational spectroscopy.....</b>	<b>32</b>
4.1 Introduction .....	32
4.2 Experimental Configuration.....	33
4.3 Results .....	36
4.3.1 Subsurface Ti-O vibration reports on the oxyl radical Ti-O• .....	37
4.3.2 Coupling to Electronic and Librational Continua.....	41

4.3.3 Theory of Interfacial Ti-O• and its Surface Modes .....	50
4.4 Discussion .....	54
4.5 Conclusion.....	54
<b>Chapter 5 Probing initial intermediates of water oxidation on n-SrTiO<sub>3</sub> with electronic spectroscopy.....</b>	<b>55</b>
5.1 Introduction .....	55
5.2 Experimental Configuration .....	57
5.3 Results .....	58
5.3.1 Formation time constant of Oxyl & Bridge Radicals .....	62
5.3.2 Theoretical calculation of transition optical dipoles of Bridge & Oxyl radicals.....	70
5.3.3 Radical Distribution & Surface-Limited Reaction Kinetics: Voltage dependence with 400 nm probe .....	73
5.3.4 Charge transfer kinetics of Radicals & VB holes: Decomposition of white light probe with applied voltage.....	77
5.4 Discussion .....	81
5.5 Conclusion.....	86
<b>Chapter 6 The dynamics of transforming initial water oxidation intermediates at n-SrTiO<sub>3</sub>/aqueous interface .....</b>	<b>87</b>
6.1 Introduction .....	87
6.2 Experimental setup .....	88
6.3 Results .....	89
6.3.1 Transformation of Oxyl & Bridge Radicals .....	90
6.3.2 Ionic strength influence on the transformation dynamics .....	91
6.3.3 pH dependence .....	92
6.3.4 Kinetic isotope effect.....	93
6.4 Discussion .....	94
6.5 Conclusion.....	96
<b>Bibliography .....</b>	<b>97</b>
<b>Appendices.....</b>	<b>106</b>

## Acknowledgements

I am grateful to my advisor Professor Tanja Cuk for her mentorship and feedback. It was an honor to be her graduate student. I also extend thanks to my committee members, Professor Richard Saykally and Professor Ali Javey for their support and guidance. I would like to acknowledge financial support from the Department of Energy and the Chemistry Department at the University of California, Berkeley. Thanks to my undergraduate research advisor at the Hong Kong University of Science and Technology, Professor Zhenyang Lin and Professor Benzong Tang, for introducing me to the exciting world of research and encouraging me to explore it further at the graduate level.

I would also like to thank my colleagues and peers in the Cuk group. Thank you for your encouragement and conversation, especially Dr. Matthias Waegele and Dr. David Herlihy who has been a friend and peer since the beginning of my graduate career. I'm glad I got to share the many adventures of science, all the good, the bad, and the ugly together.

Collaboration is an important part of my research. Many people outside the group helped me on my project. Especially, I want to thank Dr. David Prendergast and Dr. Das Pemmaraju at the Molecular Foundry who performed theoretical calculations for my projects and answered all my questions.

Finally, I would like to extend my deepest thanks to my parents and wife. Thank you my parents, for supporting me through graduate school. Thank you my wife, Winnie Hui Qing, for showing me unbelievable patience and unconditional support. I am forever grateful for her presence in my life and I am so glad I got to experience the Bay Area with her at my side.

# Chapter 1

## Introduction

World energy consumption has doubled over the past two decades. According to an estimate by IEA, in 2013, the world consumes  $3.89 \times 10^{20}$  joules of energy, equal to an average power consumption of 12.3 terawatts.<sup>1</sup> Over 80% of the energy consumed is generated from fossil fuel, which results in a large quantity of greenhouse gas CO<sub>2</sub> emission. CO<sub>2</sub> is considered as the primary cause for global warming, a major problem human beings is facing in the 21<sup>st</sup> century.<sup>2</sup> There is a need to find CO<sub>2</sub> free energy source to power the human civilization. Solar energy is a great candidate. There are two ways to utilize solar energy. Route one is to use photovoltaic that transforms solar energy directly into electricity.<sup>3</sup> Route two is to use catalyst that transforms solar energy into renewable H<sub>2</sub> or CH<sub>3</sub>OH fuel.<sup>4</sup> My research focus on solar to fuel generation. And one method to generate fuel is artificial photosynthesis.

### 1.1 Artificial photosynthesis

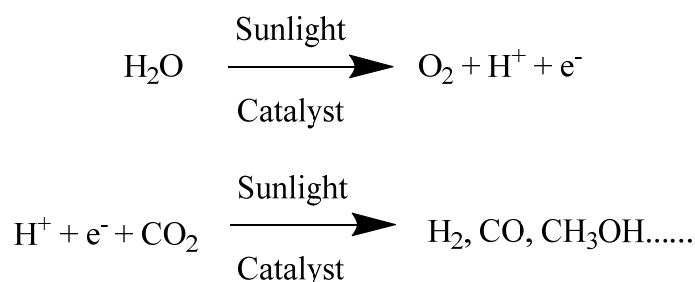


**Figure 1.1:** Reactions in artificial photosynthesis. The upper one represents water splitting reaction and the lower on represents CO<sub>2</sub> reduction reaction.

Artificial photosynthesis is a process that converts H<sub>2</sub>O and CO<sub>2</sub> into O<sub>2</sub> and fuel. Two separate reactions are involved in artificial photosynthesis, water splitting and CO<sub>2</sub> reduction.<sup>5</sup> The reactions are shown in figure 1.1. Both reactions can happen in either homogeneous fashion, i.e. reactions happen in single phase or heterogeneous

fashion, i.e. reactions happen in two or more different phases. My research is about heterogeneous artificial photosynthesis with focus on water splitting reaction.

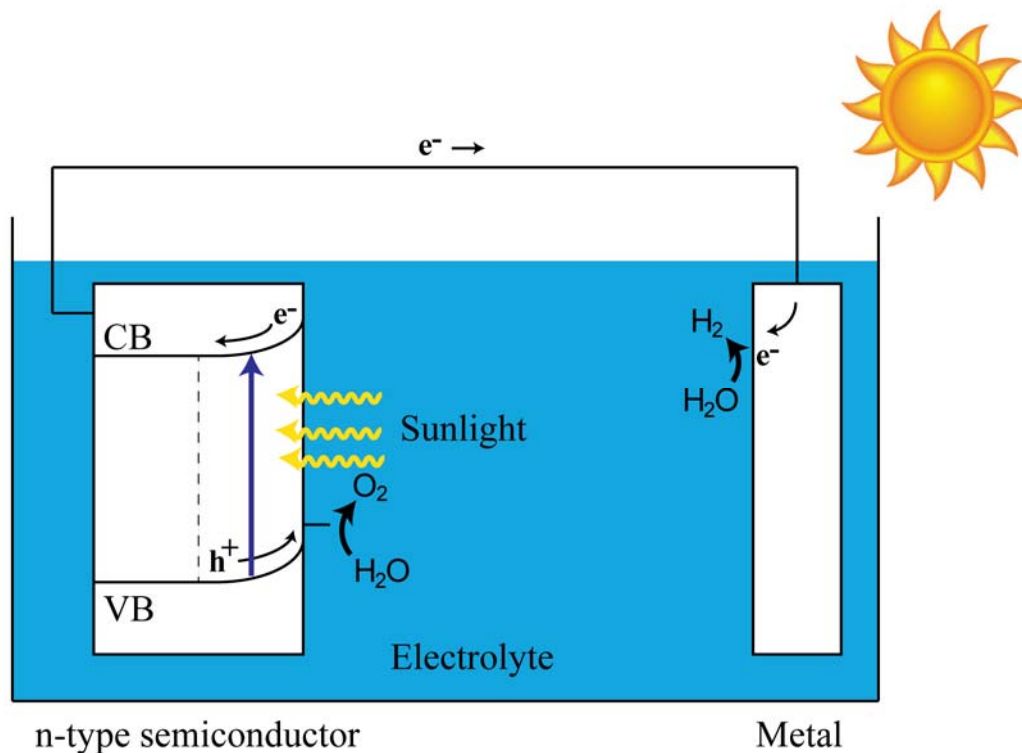
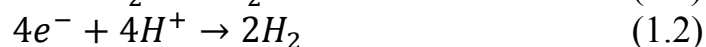


**Figure 1.2:** A representation of photoelectrochemical water splitting cell

Figure 1.2 shows a water splitting cell used in artificial photosynthesis. The original design for this type of cell can date back to 1972 when Honda and Fujishima discovered  $\text{TiO}_2$  photoelectrode.<sup>6</sup> The cell use n-type semiconductor as an anode and noble metal as cathode. Upon light excitation, charge carriers, electrons and holes, are generated within the semiconductor. Holes migrate to semiconductor anode and complete oxidation of water (1.1). Electrons travel to metal cathode and complete reduction of water (1.2).



Semiconductor material is used because it will form depletion region at electrolyte interface that can separate photogenerated charges at interface and prevent recombination. More details about semiconductor material will be introduced later.

## 1.2 Semiconductor photoelectrode

Semiconducting crystals are widely used in all industries today. In semiconductors, atomic orbitals interact and form energy bands.<sup>7</sup> The conduction band is a collection of vacant lowest electron energy states and the valance band is a collection of the highest occupied electron energy state. An energy gap,  $E_g$  is present between the top of valance band and the bottom of conduction band. Semiconductor is also characterized by its Fermi level  $E_F$ , the total chemical potential of electrons. For intrinsic semiconductors, the fermi level is generally in the middle of the band gap. For n-type semiconductor, electron donating material is introduced into the lattice, resulting in extra electrons in the conduction band and an elevated fermi level from middle of the gap. For p-type semiconductor, electron accepting material is introduced into the lattice, resulting in extra holes in the valance band and a lowered fermi level from middle of the gap.<sup>8</sup> In an electrochemical cell, n-type semiconductor is generally used as photoanode, i.e. carry out oxidation reaction. P-type semiconductor is generally used as photo cathode, i.e. carry out reduction reaction. This is due to the direction of interfacial electric field at semiconductor/electrolyte interface. For n-type semiconductor, electric field direction is towards the electrolyte, such that holes move to the interface. For p-type semiconductor, electric field direction is towards the semiconductor material, such that electrons move to the interface.

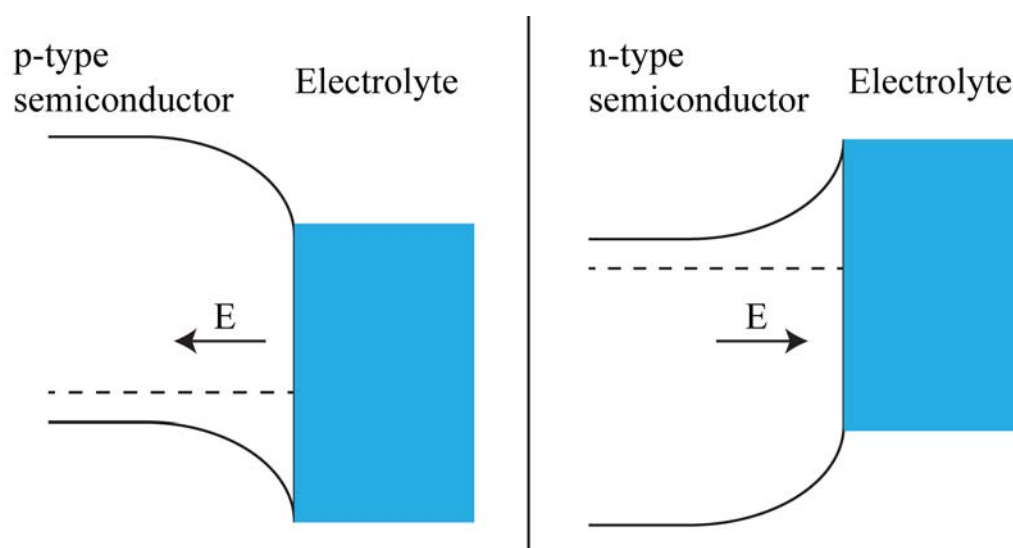


**Figure 1.3:** Electric field direction at semiconductor/electrolyte interface

Two categories of semiconducting material are generally used as photoelectrode. One category is metal oxide material such as  $\text{TiO}_2$ ,  $\text{SrTiO}_3$  and  $\text{Co}_3\text{O}_4$ .<sup>6,9,10</sup> The other is III to V group semiconductor such as GaAs, Si and GaN.<sup>11-13</sup> Both categories have achieved success in constructing efficient water splitting cell. And earth abundance, stability in solution and high efficiency makes transition metal oxide a promising material for photoelectrode.

### 1.3 Overview

To construct a viable artificial photosynthetic system, a very important aspect is to understand how interfacial properties at solid state/reactant interfaces guide catalytic reactions. The central research question is to determine how the charge dynamics in the transition metal oxide induce reaction intermediates, and conversely, how reaction intermediates influence charge dynamics in solid state catalysts. Understanding solid/reactant interface will provide us information on charge carriers' lifetime, movement, reaction intermediates formed by charge carriers and reaction intermediates' lifetime. All this information can feedback into the design of next generation high efficiency artificial photosynthesis system.

The goal of my research is to understand the interfacial charge dynamics of photocatalysis. I chose n- $\text{SrTiO}_3$  water oxidation photoelectrode as my model system. I divide my thesis into five different chapters. In chapter 2, I will briefly introduce the experimental techniques to capture interfacial dynamics and characterization techniques for semiconductors on the properties at the semiconductor/electrolyte interface. In chapter 3, I will discuss charge transfer dynamics from n- $\text{SrTiO}_3$  valance band to reactant and how valance band carriers influence interfacial voltage distribution using surface sensitive ultrafast transient optical spectroscopy. In chapter 4, I will discuss the first reaction intermediates formed on n- $\text{SrTiO}_3$  as a result of valance band carriers charge transfer using ultrafast transient infrared spectroscopy. In chapter 5, I will discuss initial reaction intermediates formed on n- $\text{SrTiO}_3$  surface from localizing charge carriers probed by transient optical spectroscopy. In the final chapter, chapter 6, I will discuss how the initial intermediates transform and form critical reaction intermediates for water oxidation reaction on n- $\text{SrTiO}_3$ . This will provide a full picture of heterogeneous water oxidation reaction on n- $\text{SrTiO}_3$ .

## Chapter 2

# Experimental techniques

### 2.1 Time-resolved laser spectroscopy

Time-resolved laser spectroscopy is a technique that uses ultrashort pulse lasers for the study of dynamics on extremely short time scales. The commonly used laser source is Ti:Al<sub>2</sub>O<sub>3</sub> (Ti:Sapphire) laser since its introduction in the 1980's.<sup>14</sup> Time-resolved spectroscopy works by using a pump laser pulse to excite a material's electrons from their ground states to higher-energy excited states. After a time-delay, a probing light source, another laser pulse, is used to interact with the excited material and gather required information. Typical data gathered from time-resolved experiment is a change in signal plotted against delay time, from which kinetic information can be extracted. Also, at any given delay time, if the probe pulse contains multi wavelength, a time-resolved spectrum can be obtained contains information on material's interaction with different wavelength of the light. A representative data plot of a transient experiment is shown in Figure 2.1.

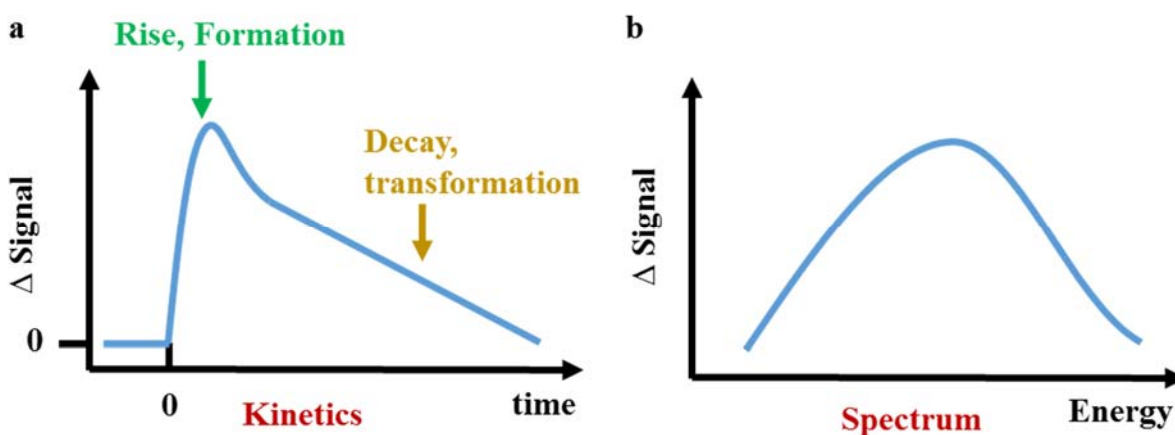


**Figure 2.1:** **a**, Representative kinetic plot of a transient experiment. The rise indicates formation of new species and the decay indicates the transformation of newly formed species. **b**, Representative spectrum at a given delay time of a transient experiment.

Time-resolved laser spectroscopy can be performed with many different geometry. The most common ones are transient absorption (TA) and reflection (TR) spectroscopy. Transient absorption measures the change in complex index of refraction by measuring the change in transmitted light or reflected light. Visible to near infrared wavelength is used to monitor electron dynamics in the material while mid-far infrared wavelength is used to monitor vibrations of chemical species on material surface. Generally, for transient absorption, the change in signal is determined as:

$$\Delta \text{Signal} = -\log\left(\frac{I_{\text{pump-on}}}{I_{\text{pump-off}}}\right) \quad (2.1)$$

where  $I_{\text{pump-on}}$  is the probe light intensity after pump light excitation and  $I_{\text{pump-off}}$  is the probe intensity without the pump light excitation. By tracking change in signal in the time domain, new species formed after pump light excitation can be identified and this information is vital to study heterogeneous photocatalysis.

## 2.2 Photoelectrochemistry

Photoelectrochemical techniques are applied to characterize the material's properties and how those properties change under light excitation. One of the most used one is Cyclic Voltammetry (CV). CV measures the current that develops under a varying applied potential that is sweeping in both the forward and reverse direction. The resulting voltammograms provide information about the potential the reaction occurs on semiconductor electrode surface and the current density. For the case of n-SrTiO<sub>3</sub>, a large anodic (negative) current indicate O<sub>2</sub> evolution and the potential at which negative current develops indicates the onset potential for oxidation reaction.

Another very important technique is electrochemical impedance spectroscopy (EIS). EIS probes the capacitance at the semiconductor/electrolyte interface based on the response to an alternating current at a defined frequency. By plotting the  $\frac{1}{C^2}$  over applied potential, many important parameters can be extracted from Mott-Schottky relationship<sup>15</sup> defined as:

$$\frac{1}{C^2} = \frac{2}{\epsilon\epsilon_0|e_0|N_dA^2} \left( U - U_{fb} - \frac{kT}{e_0} \right) \quad (2.2)$$

where  $\epsilon$  is the vacuum permittivity,  $\epsilon_0$  is the relative dielectric constant of n-SrTiO<sub>3</sub>,  $|e_0|$  is the elementary charge,  $A^2$  is the electrode area and U is the applied potential. From EIS measurement, both  $N_d$  and  $U_{fb}$  can be determined from the slope and intercept, respectively. Under light excitation, EIS can provide vital information about interfacial capacitance change as a result of light generated carriers. Many details about how light can change interfacial capacitance can be find in chapter 3.

### **2.3 Other characterization techniques**

Apart from time-resolved spectroscopy and photoelectrochemistry, many other characterization techniques are involved in characterizing semiconductor electrode. To summarize, ellipsometry is used to investigate optical constant on semiconductor electrode. Infrared absorption/reflection spectroscopy is used to characterize vibration and phonon spectrum. Low energy electron diffraction is used to determine the surface structure of semiconductor electrode. Inductively coupled plasma atomic emission spectroscopy is used to determine photo dissolution of semiconductor electrode. All these techniques contribute to the study of photocatalysis.

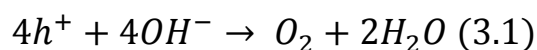
## Chapter 3

# Photocarrier dynamics and surface potential of n-SrTiO<sub>3</sub>

*Portions of the content and figures of this chapter are reprinted or adapted with permission from Waegele, M. M; Chen, X.; Herlihy, D. M. and Cuk, T. J. Am. Chem. Soc. 136, 10632 (2014).*

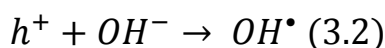
### 3.1 Introduction

Solid metal oxide photocatalysts of earth abundant metals is a promising candidate for heterogeneous water oxidation for O<sub>2</sub> evolution.<sup>16,17</sup> The full process of water oxidation takes four steps to complete. Under basic conditions, the reaction that happens is:



It is important to understand fundamentally the full water oxidation process as it can feed back into the design of more efficient solid metal oxide photocatalyst. To achieve the goal of understanding the process of water oxidation, ultrafast optical spectroscopy is applied to study oxidation of water step by step as it can follow the reaction from time zero and differentiate the kinetics of the disparate physical processes involved.

The first step of water oxidation on metal oxide surface is thought to be a charge transfer process defined as



where OH• represents a hydroxyl radical that may be bound to the metal oxide surface or be free in solution. The first step of water oxidation defines the landscape of the full catalytic cycle as it defines the absolute energy and activation barrier for the reactive holes. Previously, with the use of time-resolved optical spectroscopy a range of interfacial hole transfer time constants has been assigned from 500 ps<sup>16,18,19</sup> at the

n-TiO<sub>2</sub> to hundreds of ms<sup>20</sup> for n-Fe<sub>2</sub>O<sub>3</sub> aqueous interfaces. Many of these studies were conducted with low quantum efficiency for O<sub>2</sub> evolution (0.1% to 5%),<sup>19,21</sup> such that the true interfacial kinetics is difficult to separate from electron hole recombination kinetics within the semiconductor. Further, these studies were conducted at a single surface hole potential, determined by the valence band edge at the aqueous interface.<sup>22-25</sup> Therefore, the kinetics could not be followed as a function of the free energy difference between the reactants and products. This prevents attributing the kinetics to a single step of the reaction and understanding its activation barrier through a tunable free energy.

To overcome the problem of low quantum efficiency and single surface hole potential, we select n-SrTiO<sub>3</sub> as our target material as it can operate in a high quantum efficiency (> 75%) condition for water oxidation due to its interfacial electric field that can shuttle photo-generated holes to aqueous interface. Also, an in-situ electrochemical cell is combined with surface sensitive (< 25 nm) time-resolved optical spectroscopy that reveals the kinetics of interfacial hole transfer as a function of the surface hole potential. n-SrTiO<sub>3</sub> is a representative transition metal oxide-based photo-anode, and is ideally suited for time-resolved pump-probe spectroscopy due to its high-quantum efficiency for O<sub>2</sub> evolution with < 320 nm excitation. Continuous tuning of the surface hole potential on the electrochemical cell is achieved by a voltage and laser-induced process<sup>25,26</sup> that moves the position of the valence band edge at the aqueous interface with the applied potential on the electrochemical cell.

To give a glimpse of the result, transient kinetics reveal a single interfacial charge transfer rate constant with an exponential dependence on the surface hole potential, spanning time scales from 3 ns to 8 ps over a ~1 V increase. This allows us to map an activation barrier for a single step of the water oxidation reaction, differentiating the first hole transfer from the rest. The activation barrier for this first hole transfer, suggested to be the OH<sup>-</sup>/OH<sup>•</sup> reaction, is quantified by a hole transfer coefficient, that determines how efficiently increasing the free energy difference reduces the activation barrier and by a rate constant,  $k_0$ , that relates to its magnitude when the free energy difference is zero, or the Nernstian potential. Further, the data also suggest a Nernstian potential for the OH<sup>-</sup>/OH<sup>•</sup> reaction in solution that is in rough agreement with gas-phase studies in a hydrated environment, supporting the assignment of reaction (3.2) to the initial step of the water oxidation reaction and to the kinetics being probed here. Following the first hole transfer, the kinetics reveal a much longer time scale, possibly related to the formation of a metal oxo intermediate and further showing that multiple steps of the cycle can be differentiated.

### 3.2 Experimental configuration

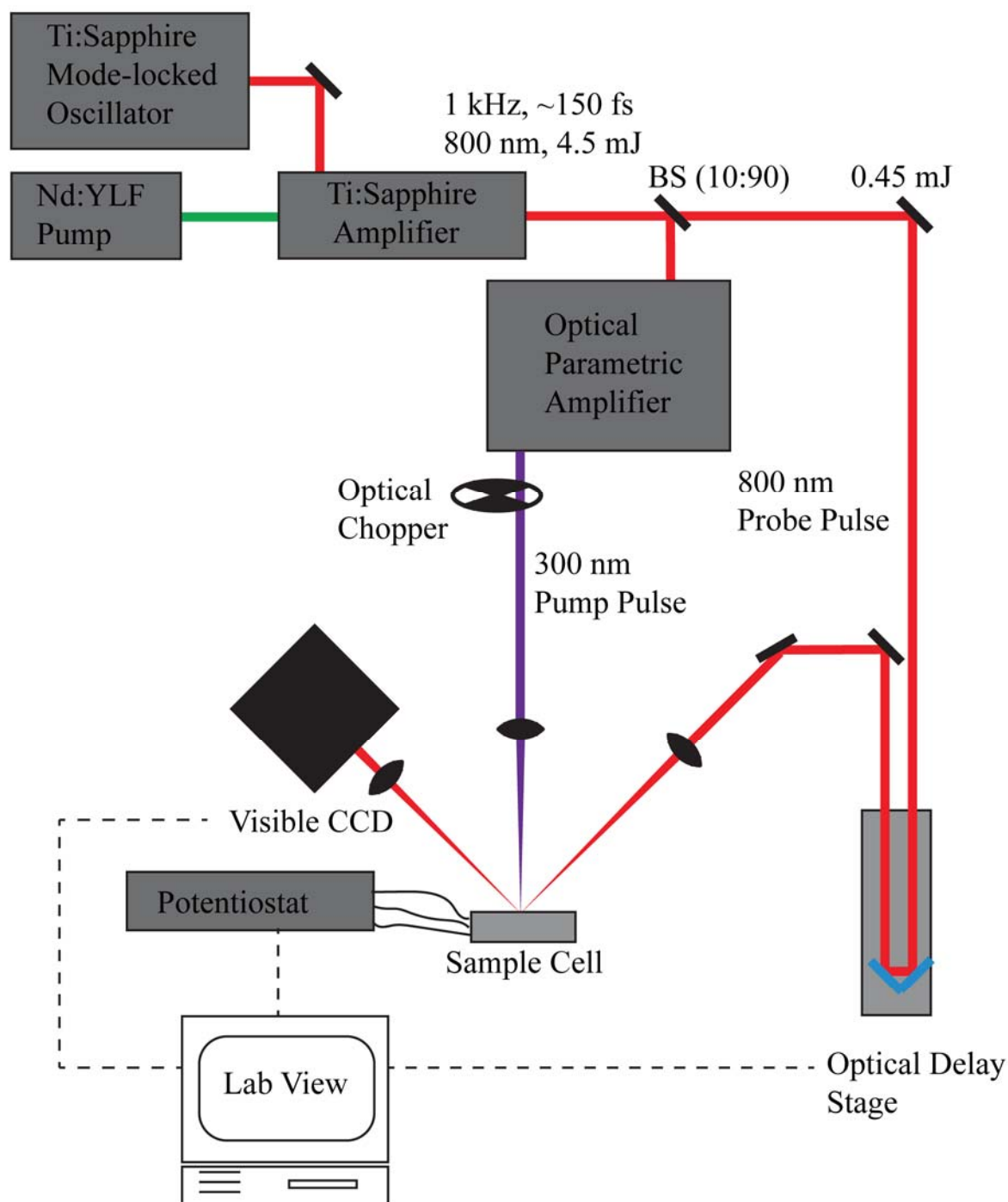


**Figure 3.1** Laser System and Pump Probe Optical Setup. BS is beamsplitter.

The time resolved laser system is illustrated in Fig. 3.1. The system consists of a regeneratively amplified Ti:Sapphire laser system (Coherent Legend, Coherent, Inc., Santa Clara, CA) with a seed input from a mode-locked Ti:Sapphire oscillator. A Nd:YLF laser provides 527 nm as the pump source for the regenerative amplifier (Evolution, Coherent, Inc., Santa Clara, CA). The output pulse has a center wavelength of 800 nm and 150 fs pulse width at a 1 kHz repetition rate with <0.5% rms energy stability. Typical output power is 4.5 W. Part of the amplifier output is directed into an optical parametric amplifier (OPA) (OPerA-SOLO; Light Conversion, Vilnius, Lithuania) for generation of laser pump pulses at 300 nm. The s-polarized 800 nm probe beam is directed onto the sample at a 45 degree incident angle. The pump beam, perpendicularly polarized to the probe beam, is incident normal to the sample surface. After the sample, the reflected probe beam is focused into an optical fiber, which is coupled to a CCD array spectrometer (CAM-VIS-3; Ultrafast Systems, LLC, Sarasota, FL). In all experiments, the pump beam is modulated by a mechanical chopper (3501; Newport, Inc., Irvine, CA) at a frequency of 500 Hz. The detector output is interfaced with a personal computer, which provided automated control over an optical pump-probe delay stage (MTM250CC1; Newport, Inc., Irvine, CA). Typical pump-induced reflectance changes ( $\Delta R/R$ ) are on the order of 0.8 mOD. The typical incident pump fluence is about  $0.045 \text{ mJ cm}^{-2}$ , corresponding to carrier densities on the order of  $10^{19} \text{ cm}^{-3}$ . The excitation beam spot size is  $\sim 500 \mu\text{m}$  (fwhm).

n-SrTiO<sub>3</sub> (0.7% and 0.08% Nb-doped SrTiO<sub>3</sub> by weight henceforth referred to as 0.7% and 0.1% respectively) single crystals with crystallographic orientation (100) are obtained from MTI Corp. (Richmond, CA). The crystals are 0.5 mm thick with polished front sides ( $R_a < 5$  Angstrom) and unpolished back sides. All spectroscopic measurements are performed on the polished front sides. The optical constants of Nb-doped SrTiO<sub>3</sub> are derived from spectroscopic ellipsometry measurements recorded on a Horiba Jobin-Yvon UVISSEL Ellipsometer (Horiba, Edison, NJ). The spectra were taken in reflection mode in air at a 70 angle of incidence.

All spectroelectrochemical measurements are performed in a Teflon electrochemical cell with CaF<sub>2</sub> optical windows (3 mm thick) as shown in Figure 3.2. The electrolyte is a  $\sim 0.1 \text{ M}$  aqueous solution of sodium hydroxide for all experiments, unless otherwise noted. To avoid formation of laser-induced air bubbles during pump-probe experiments, electrolyte solutions are briefly degassed under vacuum before commencing experimental measurements. The amount of laser light is insufficient to generate a macroscopically observable O<sub>2</sub> bubble. Bubble formation is solely due to above-band gap excitation of SrTiO<sub>3</sub>, which heats the solution nearby the sample and liberated dissolved gas.

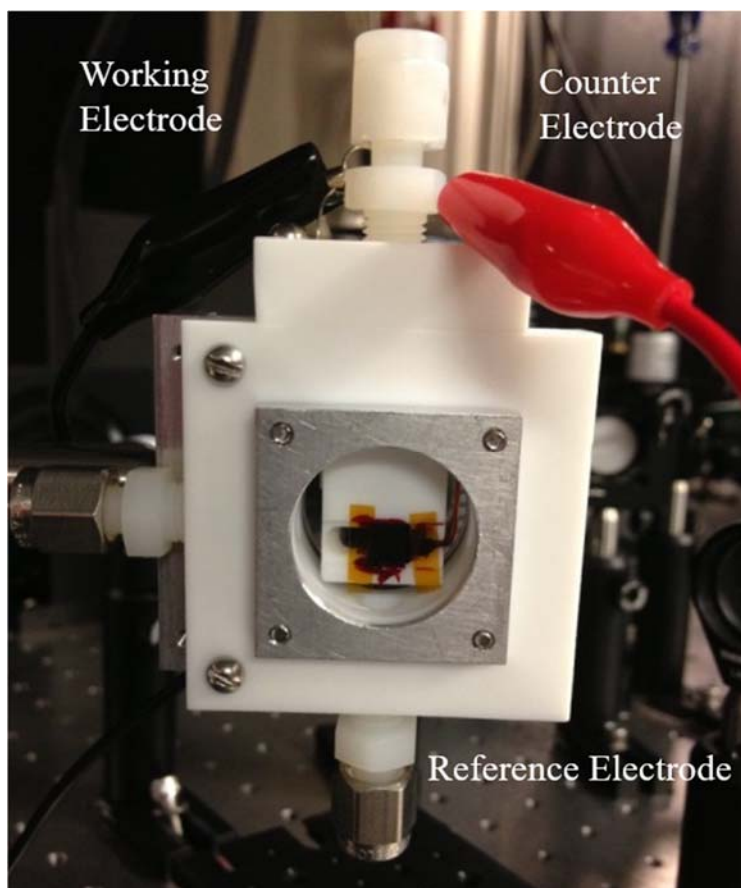


**Figure 3.2** Teflon electrochemical cell used in the experiments. n-SrTiO<sub>3</sub> (black square in the center) is used as working electrode. Pt wire is used as counter electrode and Ag/AgCl is used as reference electrode.

The electrolyte is in contact with the atmosphere during measurements. The potential of the n-SrTiO<sub>3</sub> working electrode with respect to an Ag/AgCl reference electrode (MF-2052; Basi, West Lafayette, IN) is controlled by a CHI1140B Potentiostat (CH Instruments, Austin, TX). A Pt wire serves as the counter electrode. Ohmic contact between the unpolished n-SrTiO<sub>3</sub> back side and copper wire is established using silver paste (Electron Microscopy Sciences, Hatfield, PA). For the transient reflectance experiments, an insulating lacquer covers all surfaces except the polished front side of the crystal. The exposed front surface areas of the 0.1% and 0.7% Nb-doped samples are  $\sim 25 \text{ mm}^2$  and  $\sim 50 \text{ mm}^2$ , respectively. For differential capacitance measurements, the exposed front side area is matched to the Gaussian laser spot size of  $\sim 1 \text{ mm}^2$  (fwhm).

### 3.3 Results

#### 3.3.1 Optical properties of SrTiO<sub>3</sub>

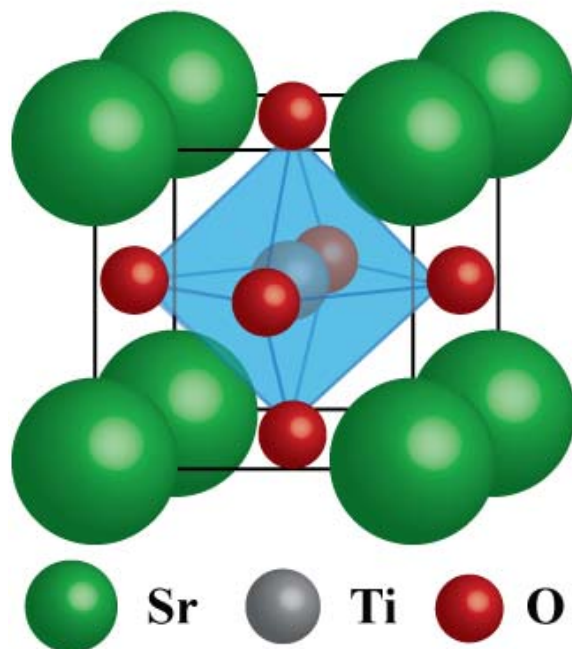


**Figure 3.3** Perovskite SrTiO<sub>3</sub> unit cell

At room temperature, SrTiO<sub>3</sub> is in cubic perovskite structure as shown in Figure 3.3 with a lattice parameter of 0.3905 nm. The Ti<sup>4+</sup> ions are six-fold coordinated by O<sup>2-</sup> ions. And each of the Sr<sup>2+</sup> ions is surrounded by four TiO<sub>6</sub> octahedra which makes each Sr<sup>2+</sup> ion coordinated by 12 O<sup>2-</sup> ions.

Electronic structure wise, SrTiO<sub>3</sub> is an intrinsic insulator with 3.25 eV as indirect bandgap and 3.75 eV as direct bandgap.<sup>27</sup> The bottom of the conduction band mainly consists of Ti 3d states with d<sup>0</sup> configuration. The top of the conduction band consists of O 2p states. Substitute Ti atom with Nb atom can achieve n-doping in SrTiO<sub>3</sub>. Nb atom will donate d electrons into conduction band and making SrTiO<sub>3</sub> a semiconductor.

Due to the wide bandgap nature of SrTiO<sub>3</sub>, most of the optical absorption happens in ultraviolet range. The optical constant of n-SrTiO<sub>3</sub> is shown in Figure 3.4. As shown in the figure, the imaginary ( $\kappa$ ) part of the complex index of refraction (related to absorption of material) peaks at ~250 nm, corresponding to transition from O 2p band into Ti 3d band. The imaginary ( $\kappa$ ) part is approaching 0 in the visible range.

(400 nm to 800 nm). The real part ( $n$ ) peaks at  $\sim 320$  nm and it converges to  $\sim 2.4$  in the visible range.

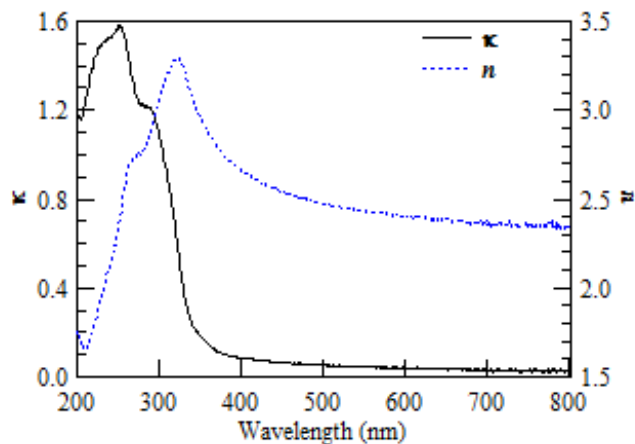


**Figure 3.4** Imaginary ( $\kappa$ ) and real ( $n$ ) parts of the complex index of refraction of n-SrTiO<sub>3</sub>

### 3.3.2 Electrochemical properties of n-SrTiO<sub>3</sub>

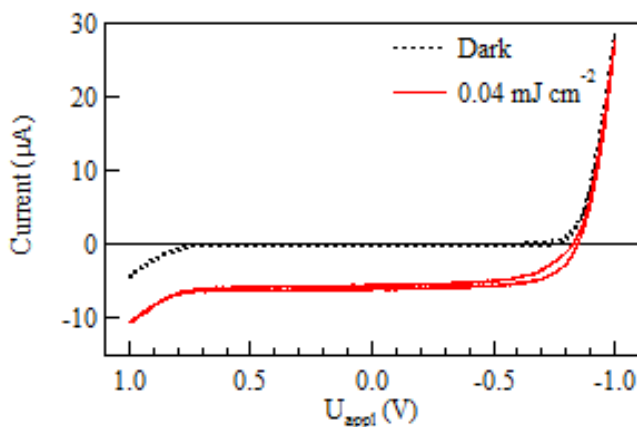


**Figure 3.5** Cyclic voltammetry of n-SrTiO<sub>3</sub> with and without laser irradiation.

Cyclic voltammetry measurements with n-SrTiO<sub>3</sub> as the photo-anode in an electrochemical cell with 0.1 M NaOH solution in the dark and with 500 Hz, 150 fs laser excitation at 300 nm is shown in Figure 3.5. In the dark, the current versus voltage curve exhibits an ideal diode-like behavior. For voltages more negative than  $-0.8$  V the n-type semiconductor is in a forward bias regime. Under anodic voltages, the semiconductor is largely in a reverse-bias regime. Under light excitation, a steady

negative photocurrent is observed for voltage more positive than -0.7 V. This photocurrent corresponds to product O<sub>2</sub> formation. The quantum efficiency of the photocurrent (> 75%), defined as the ratio of the photocurrent to the absorbed light flux, is plotted in Figure 3.6.

The high quantum efficiency is achieved by ensuring that the excitation absorption depth,  $d = \frac{\lambda}{4\pi\kappa}$ , where  $\lambda$  is the excitation wavelength and  $\kappa$  is the imaginary part of the refractive index,  $d$  is smaller or equal to the width of the depletion layer. By using data in Figure 3.4, the absorption depth  $d$  at 300 nm excitation is calculated to be ~20 nm. Then, using the Schottky approximation for the n-type semiconductor/liquid interface, the depletion width is given according to:<sup>28</sup>

$$w = \sqrt{\frac{2\epsilon\epsilon_0}{e_0N_d} \left( U_{sc} - \frac{k_B T}{e_0} \right)} \quad (3.3)$$

where  $N_d$ ,  $\epsilon_0$ ,  $\epsilon$ ,  $e_0$ ,  $k_B$ , and  $T$  represent the doping density, the vacuum permittivity, the dielectric constant of the semiconductor, the electronic charge, the Boltzmann constant, and the absolute temperature, respectively. Using a value of 0.85 V for the voltage drop in the semiconductor ( $U_{sc}$ ), the depletion width is calculated to be ~25 nm and matches the absorption depth,  $d$ , of 300 nm light.

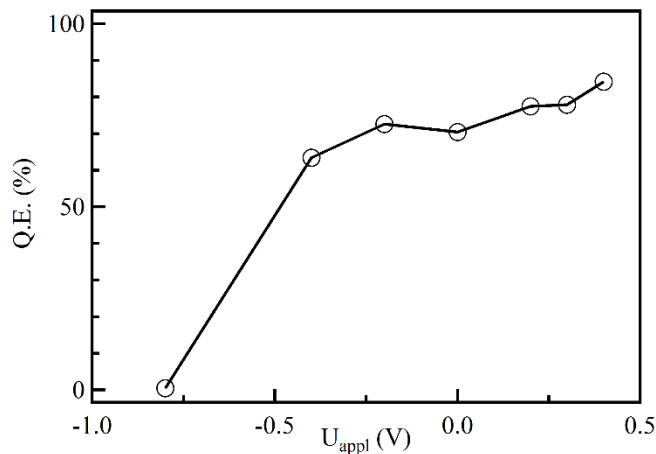


**Figure 3.6** Quantum efficiency of n-SrTiO<sub>3</sub> in 0.1 M NaOH with laser excitation.

### 3.3.3 Photoelectrochemical properties of n-SrTiO<sub>3</sub> – Shifting energy band position with applied voltage

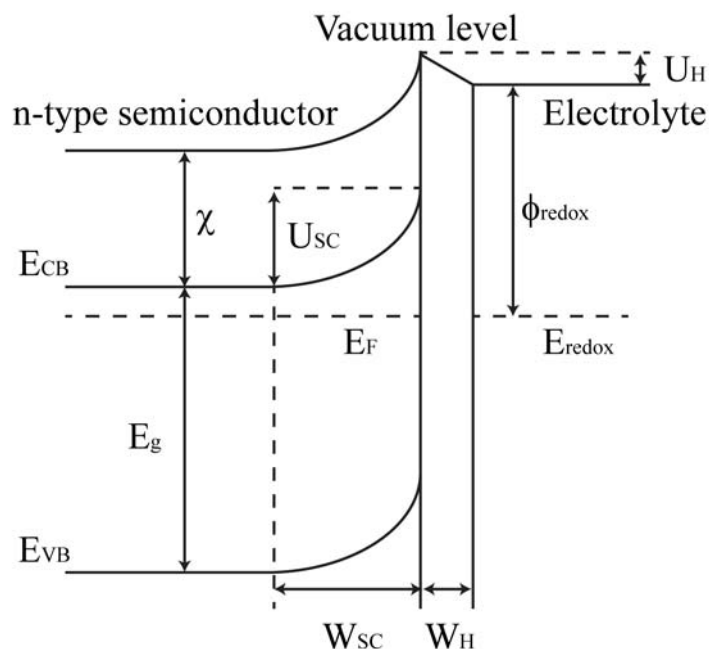


**Figure 3.7:** Band diagram at an n-type semiconductor/electrolyte interface equilibrated with the Nernst redox potential in electrolyte. The vacuum level is the energy of a free electron with zero kinetic energy. The electron affinity ( $\chi$ ) is the energy required to remove an electron from the conduction band.  $U_{SC}$  is the band bending voltage and  $U_H$  is the Helmholtz layer voltage.  $W_{SC}$  and  $W_H$  are the width of space charge layer and Helmholtz layer.  $E_{CB}$  and  $E_{VB}$  are the conduction band and valence band energies, respectively.  $E_g$  is the band gap.  $E_F$  is the fermi level and it is in equilibrium with solution redox level.

Figure 3.7 gives a detailed look at n-type semiconductor/electrolyte interface. At this interface, any voltage drop across the interface is distributed across both the semiconductor depletion layer ( $U_{SC}$ ) and the Helmholtz layer ( $U_H$ ). The Helmholtz layer comes from negative ions in the liquid screening the positive charge in the semiconductor,<sup>23,29,30</sup> forming a very thin parallel plate capacitor at the interface.  $U_H$  is therefore defined to be the voltage drop between the valence band edge potential at the interface and the solution potential. In an electrochemical cell, the voltage drop comes from both the applied voltage ( $U_{appl}$ ) and the flatband voltage determined by

equilibration of the chemical potentials of the semiconductor and the liquid ( $U_{fb}$ ), leading to the following equation:

$$U_{appl} - U_{fb} = U_{sc} + U_H \quad (3.4)$$

How the voltage is distributed across the semiconductor depletion region and the Helmholtz layer will depend on the capacitances associated with each ( $C_{sc}$ ,  $C_H$ ). Whenever  $U_H$  changes, the position of the valence band edge moves and changes the surface hole potential. Here, we find  $U_H$  for the electrochemical conditions that apply to the in-situ transient spectroscopy, namely a variable  $U_{appl}$  and high laser intensity.

At equilibrium, where  $U_{appl} = 0$  V, and in the dark,  $U_H$  can be determined experimentally. As shown in Figure 3.8, Mott-Schottky plots of the capacitance determine  $U_{fb}$  to be  $-1.52$  V and photovoltage measurements determine  $U_{sc}$  to be  $0.85$  V.

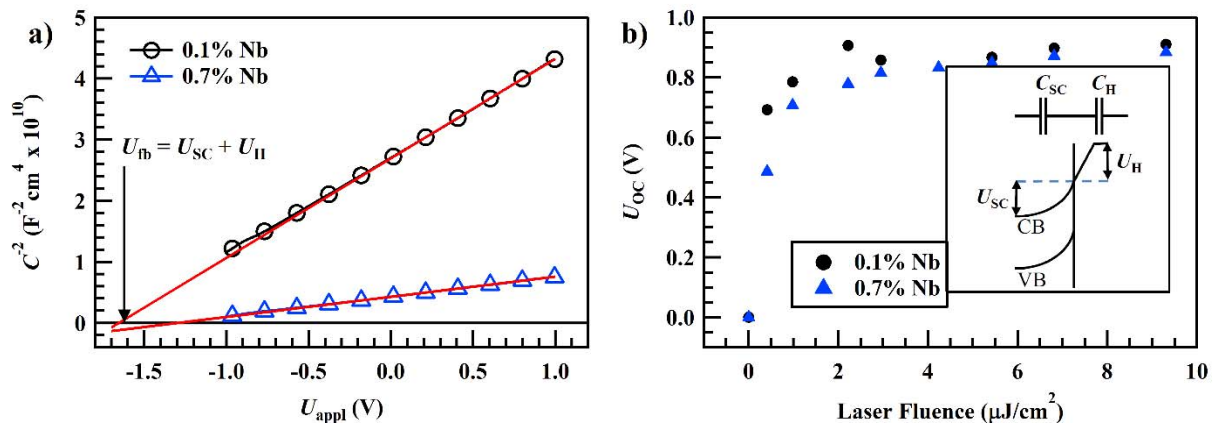


**Figure 3.8:** **a**, Mott-Schottky plots of n-SrTiO<sub>3</sub> in the dark. **b**, Photovoltage measurements of n-SrTiO<sub>3</sub> with laser irradiation. The graph indicates that only 2  $\mu\text{J}/\text{cm}^2$  fluence is needed to flatten the semiconductor energy band.

Together with equation 3.4, these measurements determine  $U_H$  to be  $0.67$  V. Similar assessments have recently been made for another n-type semiconductor, Fe<sub>2</sub>O<sub>3</sub>.<sup>31</sup> Intense light excitation alters the distribution of the voltage drop across  $C_{sc}$  and  $C_H$ . This is shown by the fact that the capacitance changes dramatically upon light excitation (Figure 3.9). Rather than simply decreasing as the applied anodic voltage becomes less negative, as it does in the dark, the capacitance starts increasing beyond an anodic voltage intermediate between the flatband voltage ( $-1.52$  V) and the photocurrent onset ( $-0.85$  V, see Figure 3.5).

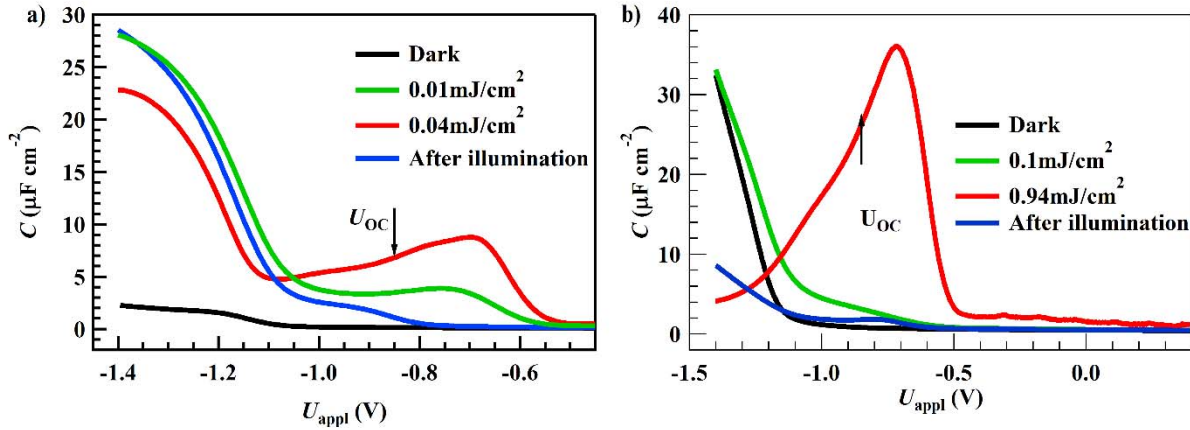


**Figure 3.9:** Differential capacitances of 0.1%Nb and 0.7% Nb-doped SrTiO<sub>3</sub> in an aqueous solution of 0.1 M Na<sub>2</sub>SO<sub>4</sub>, adjusted to a pH of 8.4 with NaOH, with and without laser irradiation as indicated. The photocurrent onsets at  $\sim -0.85$  V. As shown, capacitance changes dramatically upon light excitation which is an indication of carrier inversion that turns the surface of the n-type semiconductor into p-type. While carrier inversion was observed in both samples, a  $\sim 10$  times higher laser fluence was needed to achieve inversion in the more highly doped sample, consistent with the condition for carrier inversion, which is a photo-generated carrier density larger or equal to the semiconductor doping density.

As depicted in Figure 3.10 a, there are two types of surface charge densities (holes/cm<sup>2</sup>) that contribute to the voltage dependent capacitance in the semiconductor:  $q_{SC}$ , the hole density in the depletion layer dependent on  $U_{SC}$ , and  $q_{PHOTO}$ , induced by the laser pulse. Under laser excitation, the voltage drop that is present in the semiconductor under dark conditions is zeroed out by  $q_{PHOTO}$ , i.e. the semiconductor bands are flattened under illumination. As shown by the fast saturation of the photovoltage (Figure 3.8 b), very small laser fluences completely flatten the bands. This measurement indicates that only a small fraction of the photo-induced charge annihilates the voltage drop in the semiconductor, while most of the holes end up creating a thin, p-type layer at the interface that increases  $U_H$ . This carrier inversion process has been seen previously to move the valence band edge either as a result of a large number of surface defects<sup>32</sup> or under illumination,<sup>26</sup> as observed here.

Given the significant effect of these excess holes at the interface,  $U_H$  is a result of both  $q_{PHOTO}$  and  $q_{SC}$  screened by negatively charged ions in solution:

$$U_H = (q_{SC} + q_{PHOTO})/C_H \quad (3.5)$$

This construction has been applied successfully previously<sup>15,29</sup> for excess surface states and assumes a voltage-independent capacitance  $C_H$ . Here,  $q_{\text{PHOTO}}$  is obtained from the absorbed laser fluence and  $q_{\text{SC}}$  is given within the Schottky approximation by:

$$q_{\text{SC}} = \sqrt{2\epsilon\epsilon_0|e_0|N_d(U_{\text{SC}} - \frac{k_B T}{|e_0|})} \quad (3.6)$$

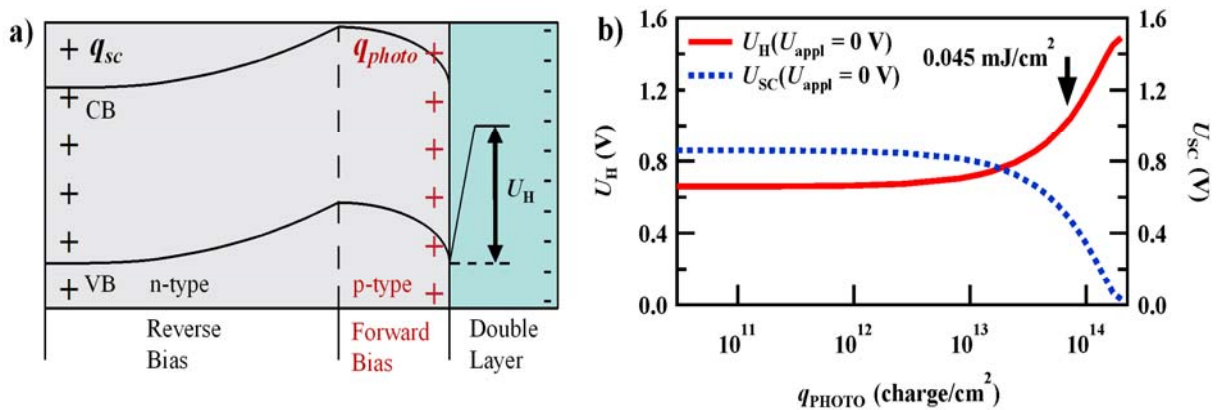


**Figure 3.10:** **a**, Band diagram showing light-induced carrier inversion at the n-SrTiO<sub>3</sub> surface where photo-generated holes change n-SrTiO<sub>3</sub> to p-SrTiO<sub>3</sub>. **b**, Calculated Helmholtz voltage ( $U_H$ ) and semiconductor (depletion layer) voltage ( $U_{\text{SC}}$ ) as a function of photo-generated charges at the interface at  $U_{\text{appl}} = 0$  V for n-SrTiO<sub>3</sub>.

$U_H$  can be self-consistently calculated from equations 3.4, 3.5, and 3.6 for a variable  $U_{\text{appl}}$  and  $q_{\text{PHOTO}}$  to match the conditions of the in-situ transient spectroscopy.  $C_H$  was determined from the equilibrium measurements in the dark, when  $U_{\text{appl}}$  and  $q_{\text{PHOTO}}$  are both zero. A  $U_{\text{SC}} = 0.85$  V and  $U_H = 0.67$  V give a  $C_H$  of  $21 \mu\text{F}/\text{cm}^2$ .

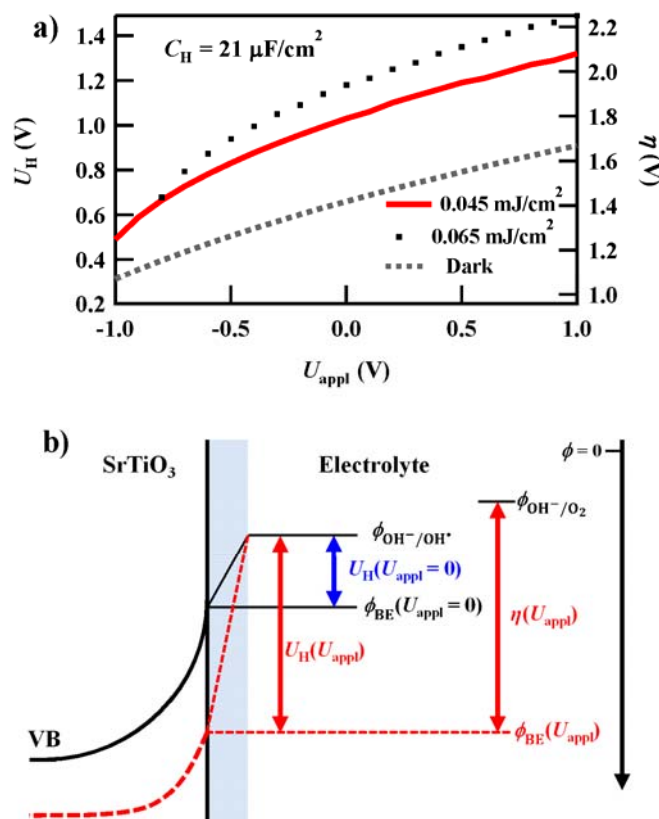


**Figure 3.11:** **a**, Calculated Helmholtz voltage ( $U_H$ ) as a function of applied potential with and without laser irradiation. The right-hand axis shows the corresponding overpotential ( $\eta$ ) for water oxidation. **b**, Graphical definition of interfacial potentials.  $\phi$ 's represent absolute potentials with respect to a reference electrode and  $U$ 's represent potential differences, or voltage drops. The area shaded in blue indicates the Helmholtz layer.

Figure 3.11 shows how the magnitude of  $U_H$  changes as a function of  $U_{\text{appl}}$  for this laser fluence, at a somewhat higher laser fluence, and in the dark. While  $U_H$  increases roughly linearly with  $U_{\text{appl}}$  in the dark as well as under illumination,  $U_H$  is substantially higher and increases more strongly with  $U_{\text{appl}}$  under illumination. The two laser fluences show that variations in  $q_{\text{PHOTO}}$  in this fluence regime have only a moderate effect on how  $U_H$  depends on  $U_{\text{appl}}$ .

Figure 3.11 b depicts the motion of the valence band edge with  $U_H(U_{\text{appl}})$ .  $U_H(U_{\text{appl}})$  will be used to map how changes in the surface hole potential modulate the kinetics in the transient spectroscopy experiments. In addition to showing how the valence band edge moves with  $U_{\text{appl}}$ ,  $U_H(U_{\text{appl}})$  itself can be interpreted as the reaction free

energy of reaction 3.2. With the absolute potential of the valence band edge at equilibrium as a reference,<sup>33</sup>  $U_H(U_{\text{appl}})$  determines the free energy difference between interfacial holes and  $O_2$  evolution, or the overpotential. As shown in Figure 3.11 a, the overpotential ranges from 1.3 to 2.1 V for the laser fluences and applied potentials used in the in-situ transient spectroscopy. This range is accessed by many n-type semiconductors used for photocatalytic water oxidation, characterized by low lying valence bands<sup>33</sup> with respect to the water oxidation potential, whether excited by UV or visible light.<sup>31</sup>

### 3.3.4 Charge transfer reaction on n-SrTiO<sub>3</sub> – Open circuit kinetics of interfacial hole transfer

The transient optical spectroscopy reported was made sensitive to interfacial hole transfer by operating under conditions where: (1) essentially all excited electron-hole pairs are separated within the depletion layer and (2) the probe is only sensitive to carrier dynamics within the depletion layer width. The high quantum efficiency (> 75%) for photocurrent for excitation wavelengths shorter than 300 nm is indicative of the first condition. To meet the latter condition, the experiments were performed in reflectance with a 45-degree incident angle. In such a reflectance geometry, the chosen near infrared probe wavelength (800 nm), sensitive to free carrier excitation, only penetrates ~25 nm from the surface according to<sup>34</sup>  $d = \frac{\lambda}{4\pi n}$  and the measured index of refraction at 800 nm (Figure 3.4). This penetration depth is equivalent to the depletion width for reverse bias conditions.

Figure 3.12 shows that the experimental conditions are in fact sensitive to interfacial charge transfer in 0.1% Nb-doped SrTiO<sub>3</sub> by comparing the transient response in aqueous electrolyte (NaOH), and in aqueous NaSCN electrolyte at open circuit. In both cases, we observe negative transient reflectance changes ( $\Delta R$ ) associated with an increase in the absorption of the material following photo-excitation of the semiconductor. Such an increase in absorption at optical frequencies corresponding to energies significantly lower than the band gap is typically assigned to the generation of free carriers, as has been done in SrTiO<sub>3</sub> previously.<sup>35</sup> Holes are the predominant free carrier generated within the depletion width by the excitation since the electrons are injected into the bulk of the semiconductor by the surface electric field faster than a few picoseconds.

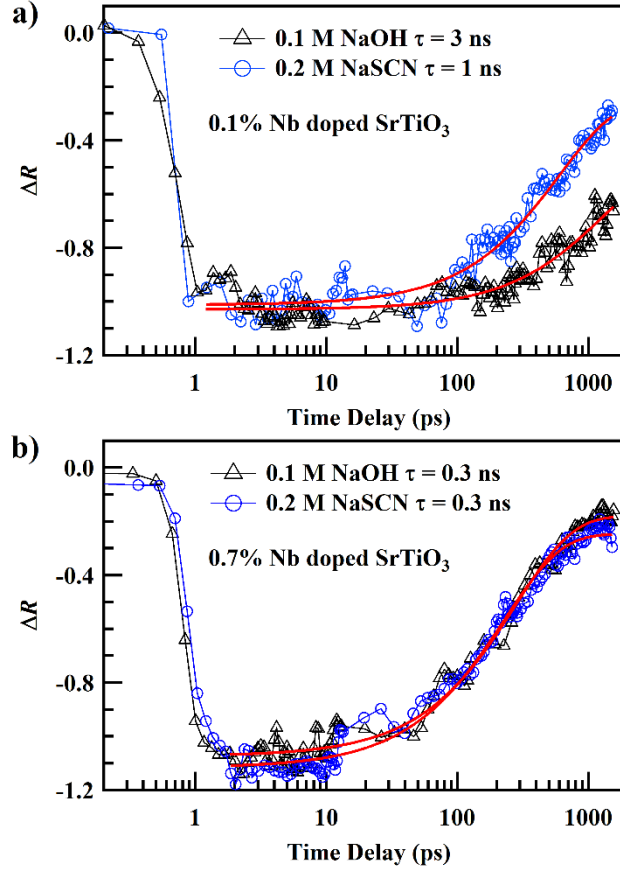


**Figure 3.12:** Normalized changes in reflectance for **a**, 0.1% Nb **b**, 0.7% Nb doped SrTiO<sub>3</sub>, attributed to the decay of photo-generated holes, probed at 800 nm under open circuit conditions. The red lines represent single exponential fits to the data. Zero time delay between pump and probe was shifted to  $\sim 1$  ps for display of the data on a logarithmic time scale.

In the semiconductor depletion region, the magnitude of the maximum of the electric field is given by:

$$E_m = \left( \frac{2e_0 N_d U_{SC}}{\epsilon_0 \epsilon} \right)^{1/2} \quad (3.7)$$

where  $N_d$ ,  $\epsilon_0$ ,  $\epsilon$ ,  $e_0$ , represent the doping density, the vacuum permittivity, the dielectric constant of the semiconductor, and the electronic charge, respectively. For a value of  $U_{SC} = 0.85$  V, we find  $E_m \sim 450$  kV/cm. The maximum carrier drift velocity is given by:

$$v_d = \mu E_m \quad (3.8)$$

The carrier mobility  $\mu$  is  $5.5 \text{ cm}^2/\text{V}\cdot\text{s}$ <sup>36</sup>, giving a maximum drift velocity of  $2.5 \times 10^6 \text{ cm/s}$ . As the electric field is linear in the depletion region, the average hole drift velocity is approximately half of its maximum value. For a depletion width of 25 nm, the hole drift time out of depletion region is close to be 2 ps.

The decrease in absorbance with time is then indicative of free holes leaving the semiconductor through the aqueous interface. As shown by single exponential fits to the kinetics, the transient response in the aqueous NaSCN electrolyte is three times faster than in the basic aqueous solution. The faster response in the NaSCN electrolyte is attributed to the lower Nernstian potential for hole transfer to  $\text{SCN}^-$ ,<sup>37</sup> a well-known hole scavenger. The significantly faster response in the NaSCN electrolyte indicates that the interfacial charge transfer of free holes are preferentially being probed in our geometry where the depletion width, the excitation penetration depth, and the probe penetration depth are all matched to 25 nm. When the depletion width is smaller and not matched to the incoming light, as in the case for the 0.7% Nb-doped sample with a depletion width of 9 nm calculated by equation 3.3, the transient response (Figure 3.12 b) does not change based on the solution potential.

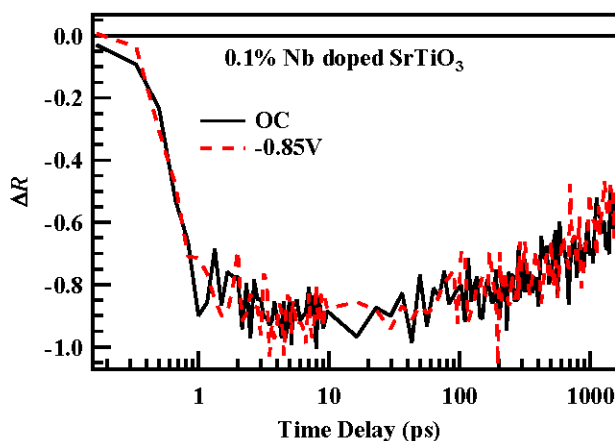


**Figure 3.13:** Comparison of transient reflectance traces for 0.1% Nb-doped  $\text{SrTiO}_3$  under open circuit conditions and with an applied bias of  $-0.85 \text{ V}$ . The invariance of the kinetics arises from identical surface hole potentials for the two cases described by Figure 3.12.

The open circuit kinetics in Figure 3.12 are measured with no leads connecting the counter electrode to the anode. However, this does not imply that a voltage is not applied. From the photovoltage measurements, the pump excitation drops an equivalent of  $-0.85$  V across the semiconductor, zeroing out the equilibrium  $U_{SC}$  in the dark and flattening the bands. This suggests another way to measure the open circuit kinetics, namely by applying  $-0.85$  V when the circuit is closed. As long as this leads to  $U_{SC} = 0$  V, the surface hole potential will be equivalent and guided by  $U_H$ .  $U_H(U_{appl} = -0.85$  V) is taken from the calculated  $U_H$  under illumination (Figure 3.11 a) and consistently gives  $U_{SC} = 0$  V according to equation 3.4. This shows that the true open circuit configuration and the circuit that applies  $-0.85$  V between reference and working electrode have equivalent surface hole potentials. These two circuit configurations yield the same transient response (Figure 3.13), which means that the measured kinetics are truly dictated by the surface hole potential.

### 3.3.5 Charge transfer reaction on n-SrTiO<sub>3</sub> – Kinetics of interfacial hole transfer as a function of overpotential

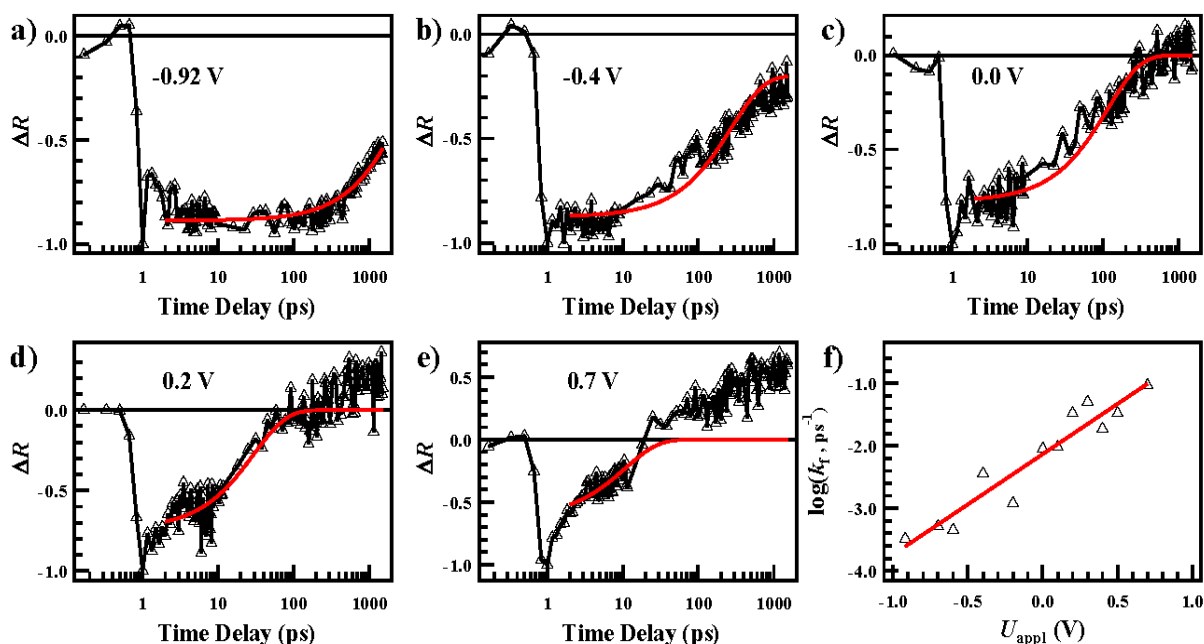


**Figure 3.14:** a-e, Normalized transient reflectance changes, attributed to the decay of photo-generated holes, probed at 800 nm at the specified  $U_{appl}$ . The red lines are single exponential fits to the data. Zero time delay between pump and probe was shifted to  $\sim 1$  ps for display of the data on a logarithmic time scale. f, Plot of  $\log(k_f)$  vs  $U_{appl}$ . The red line is a linear fit to the data.

We now turn to investigating these interfacial holes transfer kinetics as a function of changes in the surface hole potential due to valence band edge motion. As discussed in the introduction, we consider the first hole transfer, namely the initial step in the cycle of water oxidation as shown in equation 3.2

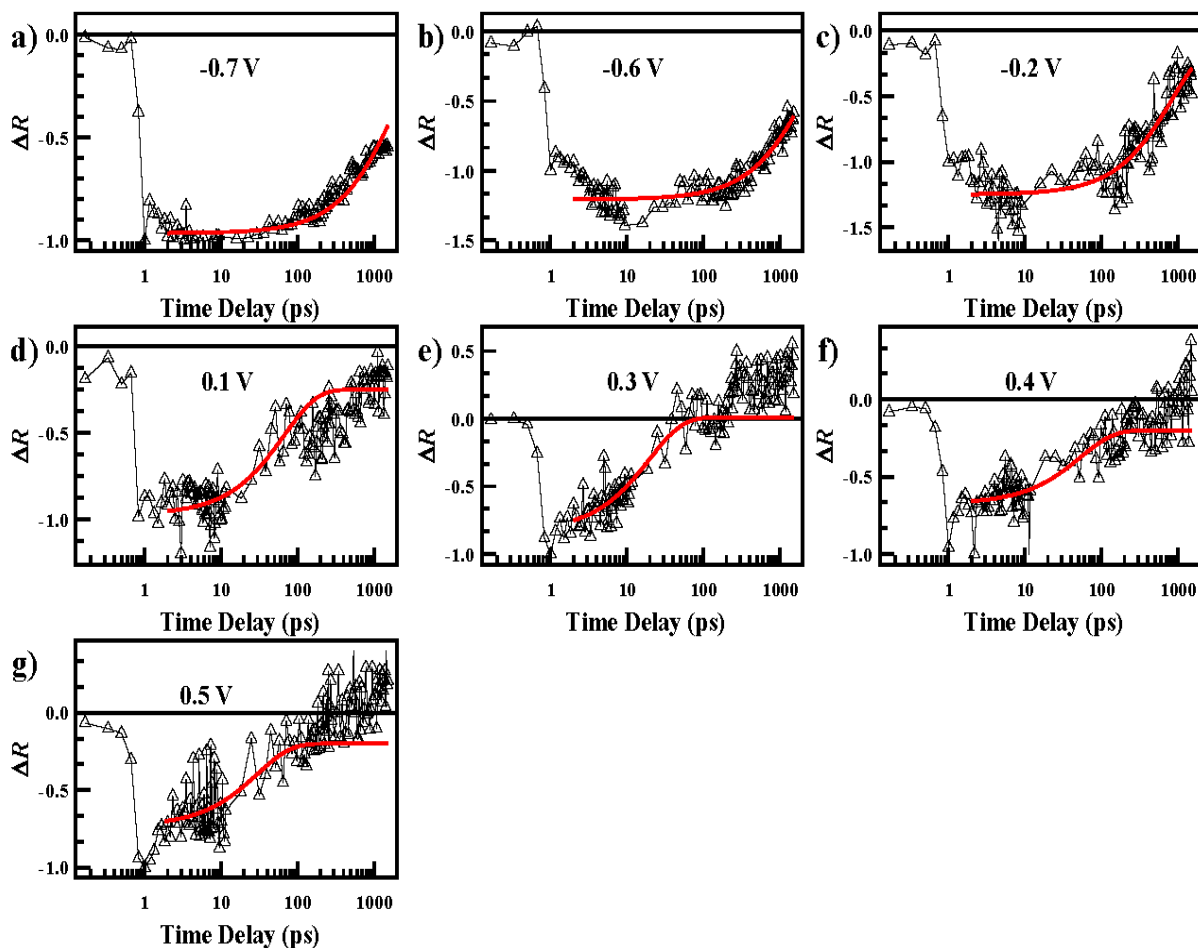


**Figure 3.15:** a-g, Normalized transient reflectance changes, attributed to the decay of photogenerated holes, probed at 800 nm at the specified  $U_{\text{appl}}$ . The data in this figure and the one shown in Figure 3.14 a-e, form the complete data set which was used to construct Figure 3.14 f.

Figure 3.14 shows the transient response ( $\Delta R$ ) for several representative applied potentials. Additional traces are provided in Figures 3.15 and 3.16. The selected voltages are taken at points where the photocurrent onsets exponentially in the forward bias regime and where the photocurrent becomes potential-independent in the reverse bias regime (Figure 3.5). For each voltage, the data could be nicely fit

with a single exponential for negative  $\Delta R$ , attributed to the decay of free holes. Such an exponential time dependence suggests a first order dependence of the above reaction on the concentration of holes. The time constant changes from 3 ns to 8 ps for applied voltages spanning  $-0.9$  V to  $0.7$  V.

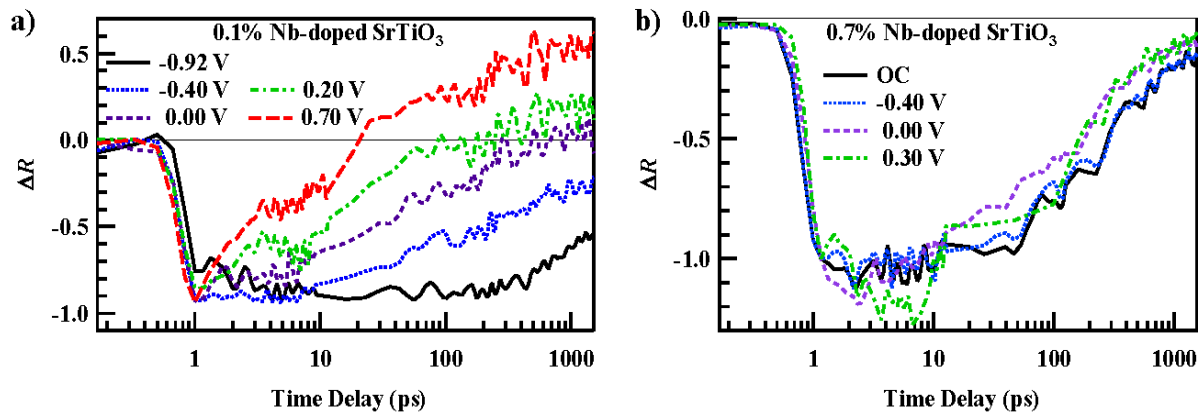


**Figure 3.16:** **a**, Same transient reflectance traces as in Figure 3.14, but plotted on the same graph for direct comparison. **b**, Independence of the transient reflectance traces for 0.7% Nb-doped SrTiO<sub>3</sub> on applied potential. This independence is attributed to the lack of surface sensitivity of the probe in this sample.

Figure 3.14 f displays how the logarithm of the rate constant depends on the applied voltage. As shown by the clear linear fit to  $\log(k_f)$ , the rate constant exponentially depends on the applied potential and demonstrates that we are measuring the rate of interfacial hole transfer as a function of surface hole potential, tuned by  $U_{\text{appl}}$ . The plot can be written in the form of an Arrhenius equation describing the activation barrier to this interfacial hole transfer:<sup>38</sup>

$$k_f = k_{OC} e^{\frac{\alpha F(U_{\text{appl}} - U_{OC})}{RT}} \quad (3.9)$$

where  $R$  is the gas constant,  $F$  is the Faraday constant, and  $\alpha$  is the phenomenological parameter that describes the shape of the activation barrier.  $k_{OC}$  is assigned to the kinetics at open circuit and  $U_{OC}$  is the equivalent applied voltage at open circuit conditions, or  $-0.85$  V as described in the previous section. As a check to analyzing the data in this way, we use the slope and the intercept of the plot ( $U_{\text{appl}} = 0$  V) in Figure 3.14 f, along with the kinetics measured at open circuit, to independently pull out  $U_{OC}$  using the transient kinetics alone. We find that the value

agrees with  $U_{OC} = -0.85$  V. This shows that the measured kinetics are truly tied to a potential tuned by the electrochemical cell in a manner that obeys the Arrhenius law.

While  $\log(k_f)$  is linear with  $U_{appl}$ , the true potential at the surface changes with  $U_H$ . To obtain a physically meaningful measurement of  $\alpha$ , we re-scaled the voltage axis in Figure 3.14 f with  $U_H(U_{appl})$  in Figure 3.11 a that determines the surface hole potential. The error in this rescaling of  $U_{appl}$  to  $U_H(U_{appl})$  comes primarily from the error in the measurement of absorbed fluence. The re-scaling is therefore done at two absorbed laser fluences,  $0.045$  mJ/cm<sup>2</sup> and  $0.065$  mJ/cm<sup>2</sup>, where the actual absorbed laser fluence is estimated to fall between these two values. Here, the coefficient of the Arrhenius equation is set to be the equilibrium hole transfer rate at  $U_H = 0$  V ( $k_0$ ):

$$k_f = k_0 e^{\frac{\alpha F U_H}{RT}} \quad (3.10)$$

While  $k_0$  is not relevant to the determination of the slope and therefore  $\alpha$ , it is an important parameter describing the activation barrier and will be discussed further below.

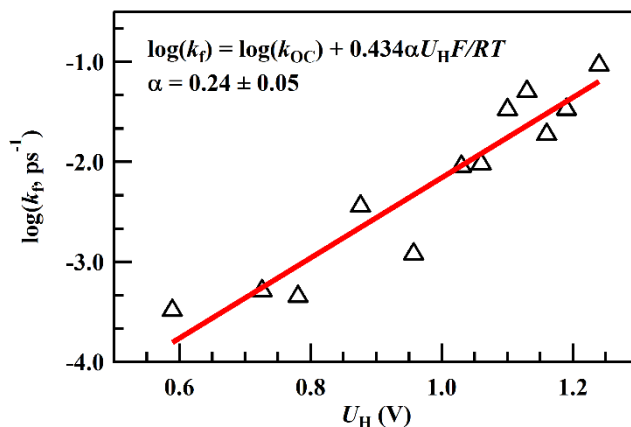


**Figure 3.17:** Plot of  $\log(k_f)$  vs Helmholtz voltage ( $U_H$ ).  $U_H$  was calculated using an excitation fluence of  $0.045$  mJ/cm<sup>2</sup>. The red line is a linear fit to the data. The extracted transfer coefficient ( $\alpha$ ) is  $0.24$ .

The results are shown in Figure 3.17 at a laser fluence of  $0.045$  mJ/cm<sup>2</sup> and give an  $\alpha$  of  $0.24$ . The results for the laser fluence of  $0.065$  mJ/cm<sup>2</sup> are shown in Figure 3.18 of and give an  $\alpha$  of  $0.19$ . Given the uncertainty in the absorbed laser fluence, we report  $\alpha = 0.20 \pm 0.05$ . This means that only about 20% of the increase in surface

hole potential is reflected in a decrease of the activation barrier for the reaction. Such an analysis leads to the asymmetric free energy diagram for interfacial charge transfer shown in Figure 3.19.

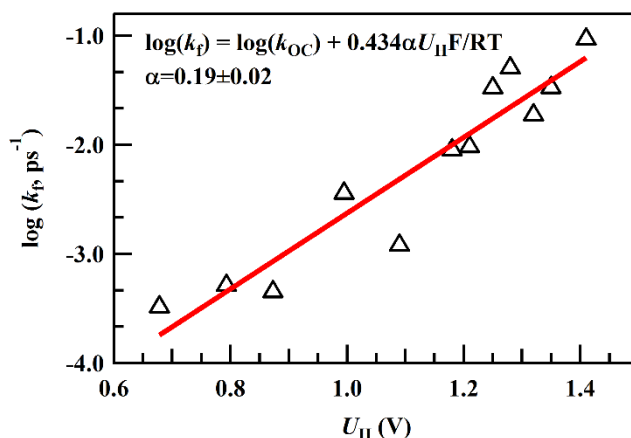


**Figure 3.18:** Plot of  $\log(k_f)$  vs Helmholtz potential drop ( $U_H$ ) with an excitation fluence of  $0.065 \text{ mJ/cm}^2$ . The derived value of  $\alpha$  is similar to the one obtained when using a fluence of  $0.045 \text{ mJ/cm}^2$ , indicating the robustness of the derived value to experimental uncertainties related to the absolute value of the fluence. The extracted value for  $k_0$  is  $(7.90 \pm 1.00) \times 10^{-7} \text{ ps}^{-1}$ . The red line is a linear fit to the data.

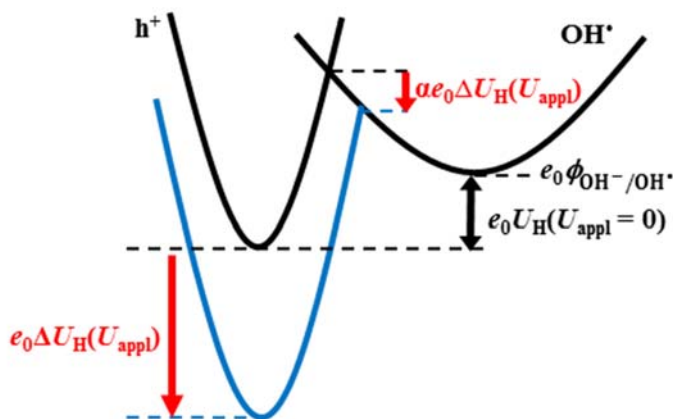


**Figure 3.19:** Diagram showing the free energy profile of the reaction.

While  $\alpha$  is commonly assumed to be 0.5, Marcus theory predicts a value different from 0.5, depending on the relative magnitude of overpotential and solvent reorganizational energy per molecule of reactant at the solid/electrolyte interface.<sup>38</sup>

While a more detailed interpretation of on a molecular level is left for future theoretical work, the value of found here shows the strongly uphill free energy posed by transferring holes from a delocalized, O 2p valence band in the semiconductor to a localized  $\text{OH}^-$  ion at the aqueous interface. We noted that the measured kinetics are obtained in a regime of high overpotential for the water oxidation reaction, covering  $\sim 1.3$  to  $2.1$  V (Figure 3.11 a). In this regime, the initial hole transfer is not rate limiting since changing the surface hole potential does not increase the photo-induced, steady state current (Figure 3.5).

### 3.4 Discussion

In using the calculated  $U_{\text{H}}$  to determine  $\alpha$  from the transient kinetics, only changes in  $U_{\text{H}}$  coming from the motion of the valence band edge are important. Therefore,  $\alpha$  is independent of an assignment of the reaction taking place (equation 3.2) and the magnitude of  $U_{\text{H}}$ .

However, such a reaction is suggested by the fast picosecond time scales for hole transfer and the very basic conditions. Since the Helmholtz layer derives from  $\text{OH}^-$  screening the positive charge in the semiconductor,  $U_{\text{H}}$  is then interpreted as the free energy difference driving the  $\text{OH}^-/\text{OH}^{\bullet}$  reaction. Here, the  $\text{OH}^-$  ions are thought of as being located at the outer Helmholtz plane, rather than the inner plane describing directly absorbed species.<sup>23</sup> Using a reference for the valence band edge,<sup>33</sup> the data imply an absolute Nernstian potential for the  $\text{OH}^-/\text{OH}^{\bullet}$  reaction of  $+1.21$  V vs Normal Hydrogen Electrode (NHE) at  $\text{pH} = 13$ . This value can be compared with that obtained by gas phase photoemission for the  $\text{OH}^-/\text{OH}^{\bullet}$  reaction  $1.41$  V vs NHE at  $\text{pH} = 13$ ,<sup>39</sup> as well as the range of values given by Bard.<sup>40</sup> The similarity in these two values supports our assignment of equation 3.2 to the measured kinetics. Further, the free energy difference driving the  $\text{OH}^-/\text{OH}^{\bullet}$  reaction at equilibrium conditions ( $U_{\text{appl}} = 0$  V) in the dark was calculated for the  $\text{TiO}_2$  (110) surface to be  $0.57$  V.<sup>41</sup> This can be compared with  $U_{\text{H}} = 0.67$  V found experimentally here at equivalent conditions (Figure 3.11). It is important to note, however, that the calculation assumes the OH species to be directly bound to the surface. Indeed, it is difficult to determine to what extent the inner Helmholtz rather than the outer Helmholtz layer is the potential difference responsible for the free energy difference, and we leave that as an open question.

In interpreting  $U_{\text{H}}$  as the free energy difference for the  $\text{OH}^-/\text{OH}^{\bullet}$  reaction, another parameter can be pulled out from the kinetic data, namely the kinetics of charge transfer at the Nernstian potential of the reaction or  $U_{\text{H}} = 0$  V. This entails finding

the x-intercept of Figure 3.17 and gives a value of  $(6.76 \pm 1.50) \times 10^{-7} \text{ps}^{-1}$  for  $k_0$ . While determines the shape of the activation barrier,  $k_0$  relates to its magnitude. This value is critical to defining the current of a single step in the water oxidation reaction and would be essential to any model of the full  $\text{O}_2$  evolving current. To our knowledge, there are no other direct measurements of this value in the literature, likely due to the fact that transient experiments on electrode reactions are scarce. Note, however, that extrapolating the intercept of the linear fit to our data assumes that equation 3.10 applies at low overpotentials for the water oxidation reaction, not directly accessible in these experiments.

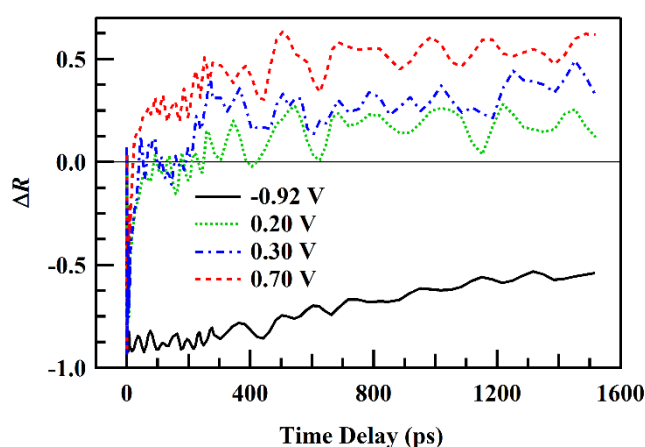


**Figure 3.20:** Representative transient reflectance traces of the same experiment shown in Figure 3.14, but plotted on a linear time scale to emphasize the emergence of a transient signal of opposite sign under large reverse bias values. The signal changes sign at pump-probe time delay values  $< 200$  ps. The persistence of this component beyond the observation window ( $\sim 1.5$  ns) indicates the multi-component nature of the reaction kinetics.

The high overpotential range of water oxidation leading to fast, single exponential kinetics at early time scales has allowed for the observation of clear multi-component kinetics within a short time window. The very fast component (below 2 ps) in the traces at applied potentials higher than 0.2 V (Figure 3.14) are tentatively attributed to hot hole transfer. At longer time scales, as shown in Figure 3.14 and in Figure 3.20,  $\Delta R$  changes sign indicating a new physical component to the kinetic response. This kinetic component is characterized by much longer time scales and does not show appreciable decay out to 1.5 nanoseconds. The results indicate that we are clearly resolving at least two kinetic components of the multi-faceted water oxidation reaction. The observation of a single rate constant exponentially dependent

on the surface hole potential that is followed by a second, much longer time scale suggests that a dominant new intermediate of the water oxidation reaction is formed upon picosecond hole transfer to  $\text{OH}^-$  within the Helmholtz layer. Future work will apply ultrafast infrared spectroscopy to this system to discover the appearance of the new intermediate that results from the disappearance of holes measured optically and at picosecond time scales here.

### 3.5 Conclusion

We observed the kinetics of the first step of the water oxidation reaction in basic conditions, namely picosecond hole transfer to form a hydroxyl radical followed by the formation of a more stable intermediate. For the  $\text{OH}^-/\text{OH}^\bullet$  reaction, we have quantified for the first time the symmetry of the activation barrier through and its magnitude through  $k_0$  using an Arrhenius equation. We consistently derived a Nernstian potential for the reaction. Such a quantification informs electronic structure calculations that investigate the activation barriers and Nernstian potentials of each hole transfer of the water oxidation cycle.<sup>42-46</sup>

## Chapter 4

# Probing initial intermediates of water oxidation on n-SrTiO<sub>3</sub> with vibrational spectroscopy

*Portions of the content and figures of this chapter are reprinted or adapted with permission from Herlihy, D. M.; Waegele, M. M.; Chen, X.; Pemmeraju, C. D.; Prendergast, D. and Cuk, T. Nat. Chem. 8, 549 (2016).*

### 4.1 Introduction

The essential step of water oxidation reaction is the formation of the O-O bond that then leads to the evolution of O<sub>2</sub>. Directly resolving the sequence of catalytic intermediates that leads to the O-O bond and how they couple dynamically to their environment is critical.<sup>47</sup>

A charged transition-metal-oxygen species that accepts electrons is thought to precede O-O bond formation. In the Mn<sub>4</sub>O<sub>4</sub> complex of photosystem II,<sup>48-51</sup> the widely initial intermediates are thought to be radicals (either Mn(IV,V)-O or Mn-O•). At the heterogeneous transition metal oxide/aqueous interface, electrochemical and spectroelectrochemical studies<sup>52,53</sup> find indirect evidence of such radicals. For titanate catalysts, the catalytic intermediate is thought to be the oxyl radical (e.g. Ti-O•), with some support for its identification from transient photocurrent/luminescence measurements and EPR under illumination.<sup>17,54-56</sup> In oxides of later transition metals, electrochemical current-voltage studies that also employ X-ray absorption and EPR,<sup>57,58</sup> suggest an oxidized metal center such as Co(IV)=O/Mn(IV)=O or an oxyl Ni-O• radical.<sup>59-62</sup>

We employ in-situ ultrafast infrared spectroscopy of a single crystal n-SrTiO<sub>3</sub>/aqueous interface under attenuated total reflection (ATR) to detect the oxyl radical, Ti-O•. Ultrafast infrared spectroscopy can identify photo-induced molecular changes at the solid-gas interface,<sup>63</sup> within the liquid<sup>64</sup> and, recently, in the condensed phase, OH stretches,<sup>47,65,66</sup> but has not yet been applied to the identification of a catalytic intermediate formed under reaction conditions. The experiments described below, in combination with theoretical modeling and

interpretation, provide the first molecular-scale detection of the transformation of charge into a nascent, catalytic intermediate at the solid-liquid interface. In doing so, they not only provide evidence for the oxyl radical, but reveal a new way to track a catalytic cycle in this setting.

## 4.2 Experimental Configuration

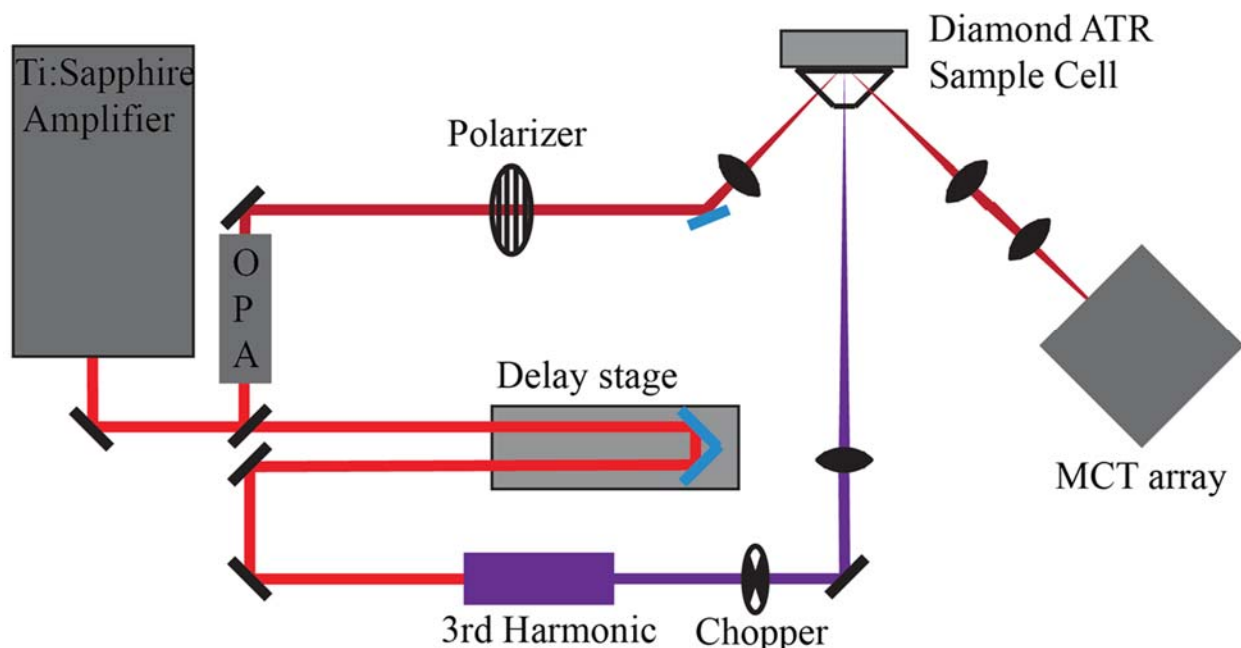


**Figure 4.1:** Representation of ultrafast infrared laser setup

The laser setup for transient experiment is shown in Figure 4.1. The pump and probe beams were derived from a regeneratively amplified Ti:sapphire laser system (Coherent Legend; Coherent, Inc., Santa Clara, CA) producing pulses with a center wavelength of 800 nm and  $\approx 150$  fs temporal width at a 1 kHz repetition rate. Part of the amplifier output was directed into an optical parametric amplifier (OPerA-SOLO; Light Conversion, Vilnius, Lithuania) for generation of laser probe pulses in the far infrared (10 – 14  $\mu\text{m}$ ). Using an anti-reflection coated ZnSe window, the OPA output was split into probe and reference beams. The probe light was directed and focused ( $f = 150$  mm) onto the aperture of a 45° trapezoidal ATR element at an incident angle of 20°. After the sample, the probe beam was collimated ( $f = 254$  mm) and focused ( $f = 150$  mm) onto the entrance slit an Acton SP-2300 spectrograph (Princeton Instruments, Princeton, NJ), where it was spectrally dispersed and

detected on the top row of a 64-element, dual-row array detector (MCT-12-64; Infrared Associates, Stuart, FL). Similarly, the reference beam was dispersed on the lower row of the detector. The detected signals were amplified using a box-car integrator (FPAS-6416; Infrared Systems Development, Winter Park, FL). The amplifier output was interfaced with a personal computer, which provided automated control over an optical pump-probe delay stage (MTM250CC1; Newport, Inc., Irvine, CA). All absorbance changes reported herein were calculated using Beer's Law, i.e.  $\Delta A = -\log(\Delta R/R_0)$ , where  $\Delta R$  is the time-dependent change in reflectance upon sample excitation and  $R_0$  is the reflection before excitation. Both  $\Delta R$  and  $R_0$  are normalized by the reference beam signal for each probe pulse detected. In all experiments, the pump beam was modulated by a mechanical chopper (3501; Newport, Inc., Irvine, CA) at a frequency of 500 Hz. The typical incident pump fluence was about  $0.040 \text{ mJ cm}^{-2}$ , corresponding to carrier densities on the order of  $10^{19} \text{ cm}^{-3}$ , or 7% of lattice sites at the surface. Using a lattice constant of  $0.3905 \text{ nm}$ , the surface site density was calculated to be  $6.56 \times 10^{14} \text{ sites/cm}^2$ . The excitation beam spot size was  $\approx 900 \text{ }\mu\text{m}$  (FWHM).

All spectroelectrochemical measurements were performed in a custom-built Teflon/stainless steel electrochemical cell with either a triple-bounce or single-bounce (Pike Technologies, Madison, WI) attenuated total internal reflection diamond element. The single crystal sample sits at a distance from the ATR element that is controlled by three single-axis micrometer stages. The intensity of the evanescent probe wave is calculated from the refraction indices of diamond and water and exponentially decays within  $2 \text{ }\mu\text{m}$  from the diamond/electrolyte interface. The electrolyte was a  $\approx 1 \text{ M}$  aqueous solution of sodium hydroxide for all experiments, unless otherwise noted. The electrolyte was in contact with the atmosphere during measurements. The potential of the n-SrTiO<sub>3</sub> working electrode with respect to an Ag/AgCl reference electrode (3M KCl) (MF-2052; Basi, West Lafayette, IN) was controlled by a CHI1140B Potentiostat (CH Instruments, Austin, TX). A Pt wire served as the counter electrode. Ohmic contact between the unpolished n-SrTiO<sub>3</sub> back side and copper wire was established using silver paste (Electron Microscopy Sciences, Hatfield, PA). Insulating epoxy (Loctite 615; Henkel North America, Rocky Hill, CT) covered all surfaces except the polished front side of the crystal. The exposed front surface area was typically between  $2$  to  $4 \text{ mm}^2$ .

The n-SrTiO<sub>3</sub>/electrolyte interface is photo-activated in the single-bounce diamond ATR spectroelectrochemical cell described above by a  $266 \text{ nm}$ ,  $150 \text{ fs}$  light pulse at  $500 \text{ Hz}$ . A  $150 \text{ cm}^{-1}$  bandwidth infrared pulse in the range of  $700 - 1000 \text{ cm}^{-1}$  probes the photo-induced signals at the interface. To achieve photo-catalytic

activity, the single crystal sample is situated at a  $< 3 \mu\text{m}$  distance from the diamond ATR surface, such that the evanescent wave probes through the electrolyte before reaching the photo-activated interface (Figure 4.2). The penetration depth of evanescent wave is shown in Equation 4.1. For a diamond ( $n_1 = 2.4$ ) electrolyte ( $n_2 = 1.12$ ) interface, for a  $60^\circ$  angle of incidence, at  $800 \text{ cm}^{-1}$ ,  $d_p \approx 3 \mu\text{m}$ .

$$d_p = \frac{\lambda}{2\pi\sqrt{n_1^2 \sin^2(\theta) - n_2^2}} \quad (4.1)$$

The z-distance is controlled by a piezoelectric motor with 30 nm resolution, calibrated by the magnitude of the  $\Delta A$  signal. In a geometry where the active surface is at a distance from the generation of the evanescent wave (here, the diamond/electrolyte interface), the signal decays along with the evanescent wave intensity.<sup>67</sup> The sample is reproducibly positioned at the mid-point of the decay of the  $\Delta A$  signal, proportional to the evanescent probe wave intensity.

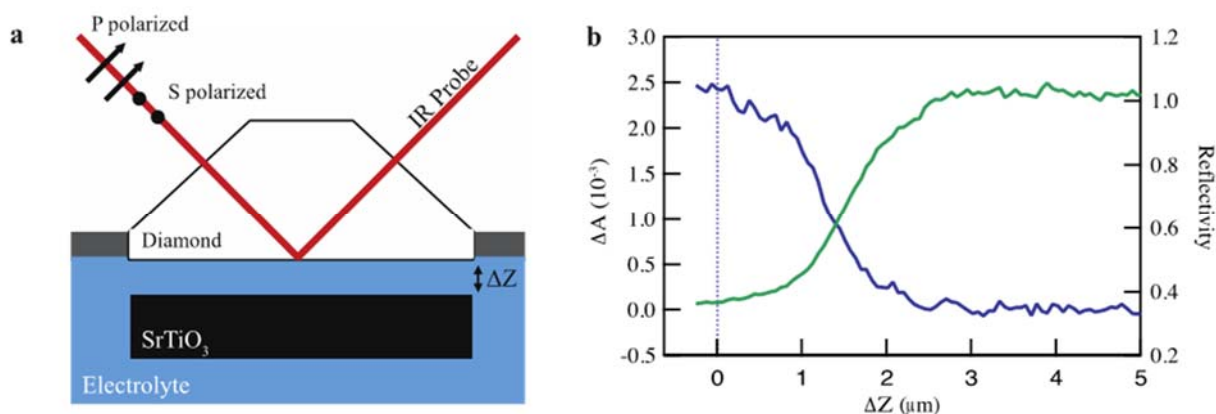


**Figure 4.2:** Experimental Geometry. **a**, The  $\text{SrTiO}_3$  single crystal is positioned within the evanescent wave generated at the diamond – electrolyte interface.  $\Delta Z$  ( $0 - 10 \mu\text{m}$ ) is controlled using a piezo-electric stepper motor. **b**, When a n-doped  $\text{SrTiO}_3$  sample is stepped towards the diamond, the magnitude of the transient signal (blue) grows as the sample enters the probe region. Conversely the light throughput (green) decays from its maximum value as the  $\text{SrTiO}_3$  single-crystal attenuates the light. The dotted line indicates when the sample is considered pressed to the diamond surface.

### 4.3 Results

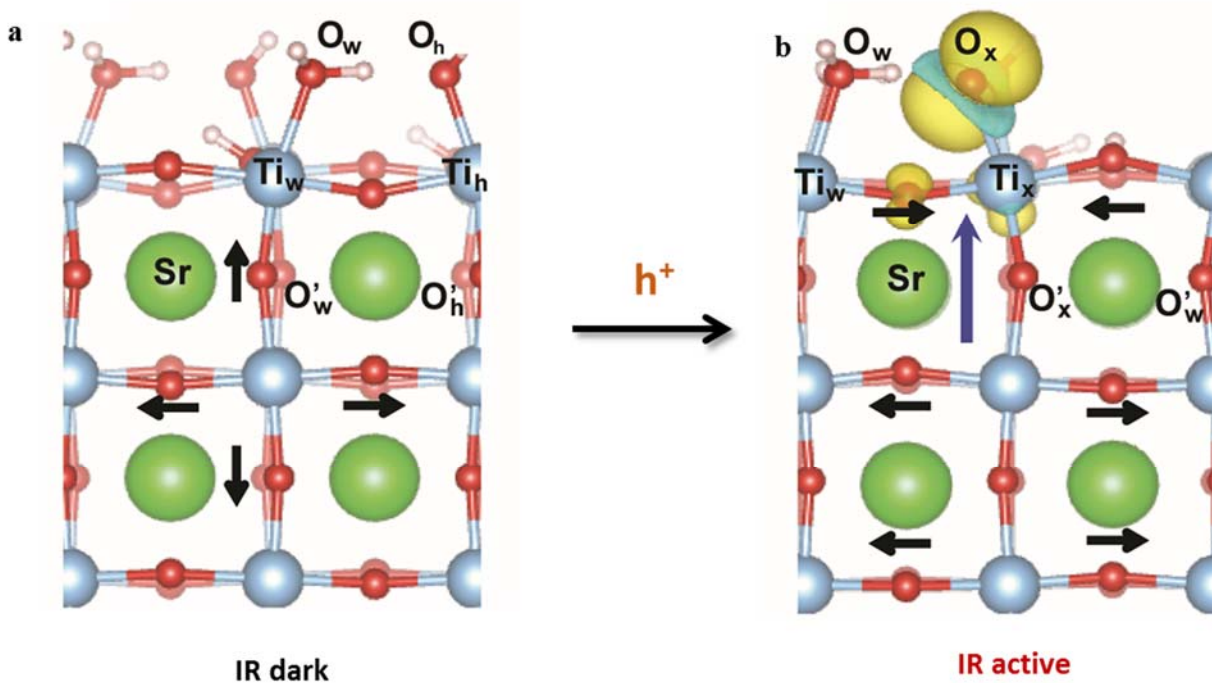


**Figure 4.3:** Infrared activity of the oxyl radical. A representation of the water-adsorbed SrTiO<sub>3</sub> surface before and after illumination. **a**, Water-adsorbed SrTiO<sub>3</sub> surface. The mode shown is a bulk breathing motion present in the dark and infrared-inactive. **b**, Water-adsorbed SrTiO<sub>3</sub> after illumination. Changes in electron spin density (decrease, yellow; increase, cyan) indicative of hole capture to O<sub>x</sub> result in a surface Ti<sub>x</sub>-O<sub>x</sub>• termination. The presence of Ti<sub>x</sub>-O<sub>x</sub>• generates a new (surface) infrared-active mode because of a large-amplitude motion of O<sub>x</sub>' that disrupts the original breathing mode.

The perovskite SrTiO<sub>3</sub> (100) is shown with a water-adsorbed surface of the Ti-O layer in Figure 4.3. Both the Ti-O and the Sr-O layer can be exposed, with a suggested ratio of 7(TiO):3(SrO) by surface sensitive x-ray diffraction.<sup>68</sup> The Ti-O surface is shown with all transition metal sites terminated by either water or hydroxyl groups, as expected for an ambient air or aqueous electrolyte interface.<sup>69</sup> Photoexcitation at the n-SrTiO<sub>3</sub> interface generates a hole that is trapped at a surface terminating oxygen site in a form of oxyl radical, Ti-O•, as shown in Figure 4.3 b. First-principles density functional theory calculations indicate that producing the radical causes a bulk breathing mode (Figure 4.3 a) to combine with other dark and

infrared-active modes of the initial configuration. This new surface mode (Figure 4.3 b) is infrared-active due to a large amplitude, Ti-O stretch motion of the O (labeled  $O_x'$ ) in the SrO layer right below the Ti-O• site; the assigned IR activity matches the bright surface mode observed by the ultrafast experiments. This bright surface mode, and the Fano lineshapes that are sensitive to the electron plasma density and the electrolyte, is expected to report on the Ti-O oxyl species until a new bond is formed (e.g. the O-O peroxy species).

### 4.3.1 Subsurface Ti-O vibration reports on the oxyl radical Ti-O•

The spectrum of the photo-generated bright mode, probed by attenuated total reflectance, peaks at  $795\text{ cm}^{-1}$ , is shown in Figure 4.4 for the 0.1% Nb-doped n-SrTiO<sub>3</sub> sample. The narrow bandwidth of the photo-generated signal ( $35\text{ cm}^{-1}$ , 4 meV) and its appearance in the frequency range known for Ti-O stretches are strong evidence for a vibrational rather than an electronic transition. Moreover, the same narrow mode occurs over a wide range of doping (Nb 0.1% to 0.7%) and surface excitation (0.5% to 30%) that would necessarily modify the width of an electronic transition.

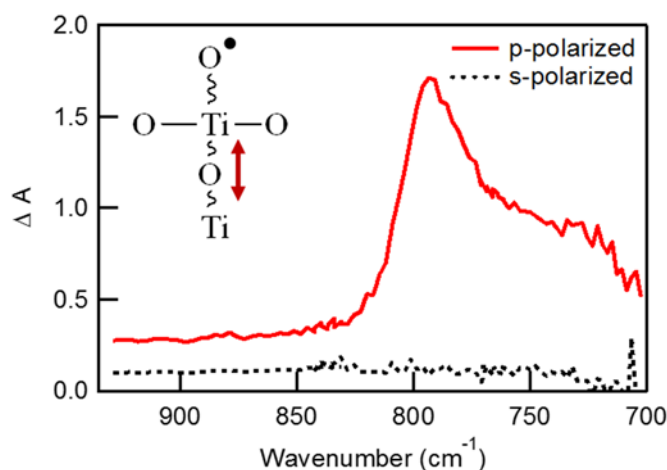


**Figure 4.4:** Photo-induced absorption of the oxyl radical is defined experimentally by its polarization. It is only observed using p- (red line) but not s- (black dashed line) polarized light. The inset shows the sub-surface vibration after localizing a hole on the surface to form oxyl radical.

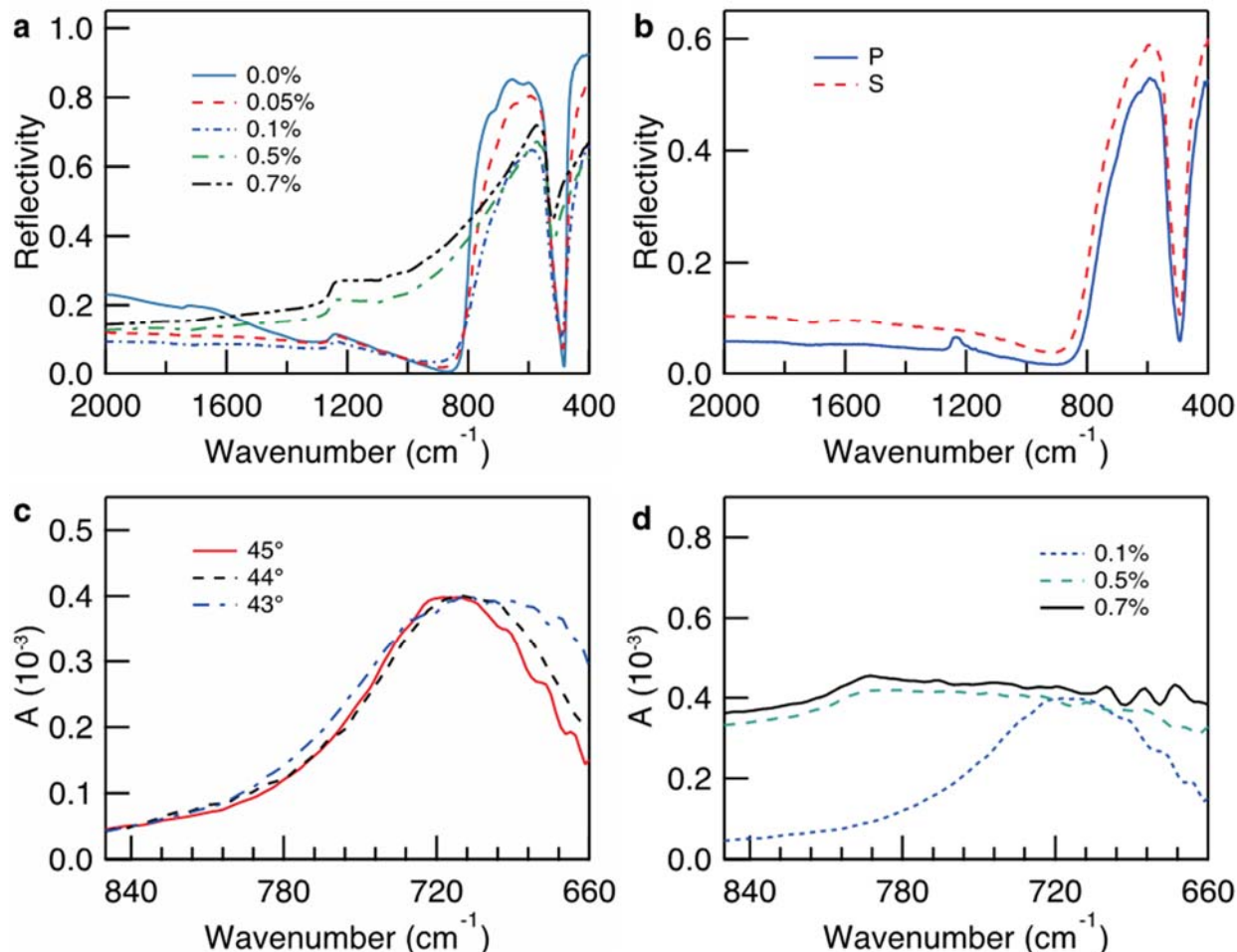


**Figure 4.5:** Specular reflectance and attenuated total reflection of SrTiO<sub>3</sub>. **a**, Reflectance spectra of undoped and variously % Nb doped SrTiO<sub>3</sub>. **b**, Static reflectance of 0.1% Nb doped SrTiO<sub>3</sub> sample for both S and P polarization. **c**, Static ATR of 0.1% Nb doped SrTiO<sub>3</sub> with different incident angles (P-polarization). **d**, Static ATR spectra of SrTiO<sub>3</sub> with different dopings (P-polarization).

The photo-generated mode solely occurs in P-polarization of the infrared probe beam. Its exclusive appearance in P-polarization completes its identification as a molecular, surface localized vibration with a dipole perpendicular to the sample plane. While a bulk LO phonon also occurs near 800 cm<sup>-1</sup> in reflectivity measurements,<sup>70</sup> it shows up in both P and S polarization in single crystal samples (Figure 4.5) and moreover, the interfacial reflectance measured by ATR is not sensitive to the bulk LO phonon at all (Figure 4.5). Other than a surface polariton seen previously,<sup>71</sup> which occurs as a broad mode centered at 700 cm<sup>-1</sup> and only at the air interface, no mode is observed by the evanescent infrared probe in the ATR

cell in this frequency range without photo-excitation. Therefore, the photo-generated mode is characteristic of a new transient species rather than a change in the dipole or occupation of a ground state mode. It is important to note that the sign of the transient species, when measured by ATR of the solid-liquid interface, cannot be interpreted via Beer's law and a new absorptive cross-section can appear as either a positive or negative differential signal. This is discussed in the following paragraph.

The transient data is collected using the evanescent wave generated by total internal reflection at the diamond/electrolyte interface as a probe. Equation 4.2 governs the absorption change (for weakly absorbing samples).

$$\begin{aligned} \Delta A &= -\log \left( \frac{I_0 - I_0 \left( \frac{n^{ON} \kappa^{ON} |t_{12}|^2}{n_1 \cos(\theta) \sqrt{n_1^2 \sin^2(\theta) - n_2^2}} \right) e^{\frac{-2\Delta Z}{d_p}}}{I_0 - I_0 \left( \frac{n^{OFF} \kappa^{OFF} |t_{12}|^2}{n_1 \cos(\theta) \sqrt{n_1^2 \sin^2(\theta) - n_2^2}} \right) e^{\frac{-2\Delta Z}{d_p}}} \right) \\ &= -\log \left( \frac{1 - T^{ON}}{1 - T^{OFF}} \right) \quad (4.2) \end{aligned}$$

Where  $n^{ON}$ ,  $\kappa^{ON}$ ,  $n^{OFF}$ ,  $\kappa^{OFF}$  represent the indices of refraction with light on and light off. Although the samples used in these experiments are not weak absorbers, the simplified relation serves to highlight an ATR-specific property; as the sample is positioned closer to the diamond there is greater overlap between the sample and the evanescent electric field, so more light is attenuated, and the reflectivity drops. Likewise, in the differential (pump-probe) signal, the displacement of the sample from the interface will lower the magnitude of the transient signal. This is accounted for by repeatable positioning of the sample as described above.

Equation 4.2 shows that  $\Delta A$ , probed by ATR, can change in a complex manner with  $n^{ON}$ ,  $\kappa^{ON}$ ,  $n^{OFF}$ , and  $\kappa^{OFF}$ . In the limits of weak absorption and where a continuum is not involved through  $n$ , the interpretation can be simplified to a purely absorptive change in  $\kappa$ . Here, we are in the strongly absorbing limit and have two continua involved (the solid state plasmonic and liquid librational continua). This means that, while the Fano lineshape analysis below makes it clear that we are observing the frequency dependence of an intrinsic matrix element of an absorptive change at the solid-liquid interface, the sign and magnitude of the differential signal depends on the details of  $n$  and  $\kappa$ . Through the Kramers-Kronig relation that derives  $n$  from  $\kappa$ , changing the absorption cross section via  $\kappa^{ON}$  also modifies  $n^{ON}$  in the same spectral region. Furthermore, photoexcitation will change  $n$ ,  $\kappa$  over a larger spectral range than is being measured. Therefore, to truly determine the absolute change in the

absorptive cross-section ( $\kappa^{\text{ON}} - \kappa^{\text{OFF}}$ ), the Kramers-Kronig relation for  $n$  and  $\kappa$  over a large frequency range should be consistently incorporated into the ATR equations. We do not attempt this here, as it requires taking data out to far infrared frequencies. Instead, we rationalize the sign of the signal necessitated by the Fano lineshapes below by the changes in reflectivity that occur with doping in the 700-1000  $\text{cm}^{-1}$  spectral range being measured (Figure 4.5).

The photo-generated mode is attributed to a transient  $\text{Ti-O}\cdot$  species by: (1) its appearance only with photo-induced charge separation at the n-SrTiO<sub>3</sub> interface, (2) a long lifetime that decreases as a function of methanol concentration, and (3) its correlation with O<sub>2</sub> evolution. The photo-generated mode occurs exclusively in n-doped samples (Figure 4.6 a), while it is completely absent in un-doped and p-doped samples that have low quantum efficiency for charge separation and O<sub>2</sub> evolution (< 1%). The lifetime of the signal at 795  $\text{cm}^{-1}$  (Figure 4.6 b) demonstrates a very long-lived vibration (> 1 ns). This long and fluence-independent lifetime excludes an assignment to a highly excited Ti-O surface mode of the ground state. Finally, the lifetime decreases substantially as a function of methanol concentration in water (Figure 4.6 b), indicating that the photo-hole generated transient species occurs uniquely at the water-adsorbed surface and is quenched by a better hole acceptor.

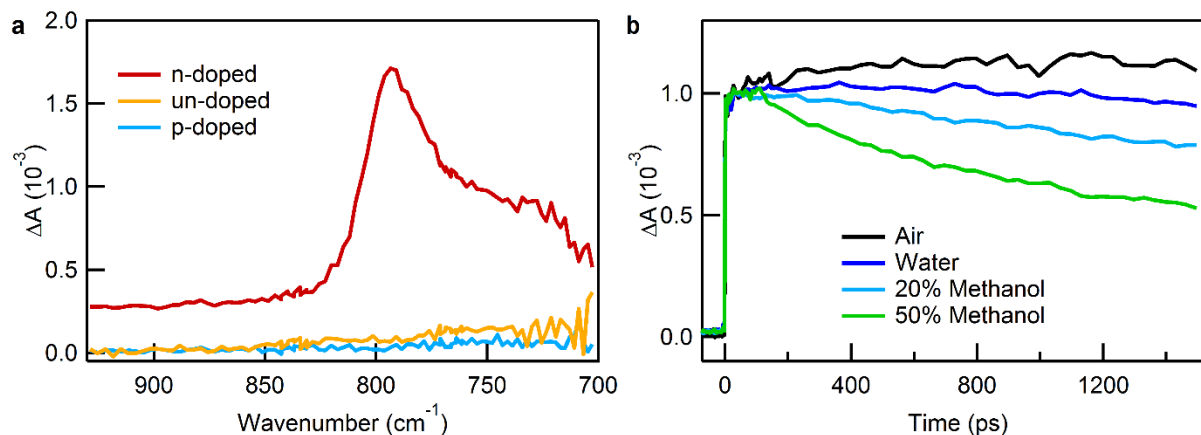


**Figure 4.6:** Investigating the  $\text{Ti-O}\cdot$  oxyl signature of n-SrTiO<sub>3</sub>. **a**, Absorption only appears in n-doped SrTiO<sub>3</sub> (red line) and not in p-doped (blue) or undoped (orange) SrTiO<sub>3</sub>. **b**, Normalized kinetics of the transient response at 795  $\text{cm}^{-1}$  for the 0.1% Nb n-doped sample in contact with air (black line), water (blue line), and 20% (cyan line) and 50% (green line) methanol in water.

To understand this transient species as being a photo-hole active site for water oxidation, the magnitude of the absorbance change at closed circuit, when a

photocurrent evolves, is compared with  $O_2$  evolution (inferred from the photocurrent measured by a potentiostat) (Figure 4.7). Varying the laser excitation fluence increases both the steady-state photocurrent and the observed signal magnitude, as shown in Figure 4.7. Here, to compare the absorbance change to the current, both signals are normalized at a fluence of  $0.04 \text{ mJ/cm}^2$  (3% surface site excitation). The error bars in the absorbance change were calculated from three independent trials, where the data is taken with either increasing or decreasing fluence; at higher fluence damage to the sample decreases the signal slightly and therefore, biases the absorbance change to lower values. When the sample is fully pulled back from the diamond ATR crystal and the photocurrent is not diffusion limited (at the position at which infrared data is taken, the photocurrent is diffusion limited), the Q.E. of the photocurrent reaches 80%. Together with 100% Faradaic efficiency of  $O_2$  evolution at n-SrTiO<sub>3</sub>/aqueous interfaces,<sup>72</sup> this high Q.E. means that almost all of the hole-activated sites at picosecond time scales are involved in the evolution of  $O_2$  (as long as enough reactants are available). In light of the fact that the absorbance change tracks a new transient species of a photo-hole at a water absorbed surface, is itself surface localized, and further, scales with highly efficient  $O_2$  evolution, we propose the vibration is that of a Ti-O• species active in the water oxidation reaction.

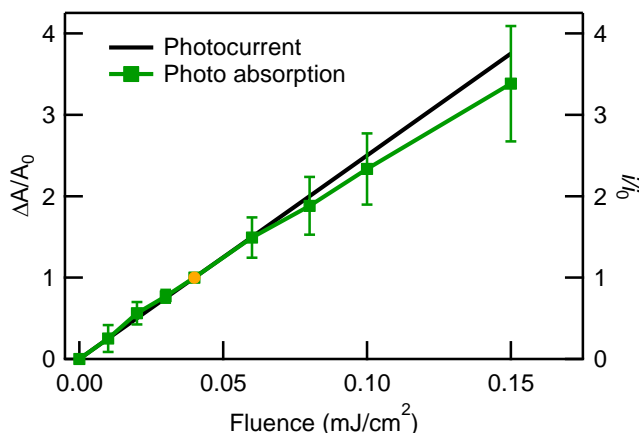


**Figure 4.7:** Absorbance change (green, squares) at  $795 \text{ cm}^{-1}$  and the resulting steady-state photocurrent  $i$  (black line), measured in a three-electrode cell held at  $0.0 \text{ V}$  versus Ag/AgCl at pH 14. Error bars in  $\Delta A$  represent the standard error over three trials.  $\Delta A$  and  $i$  have been normalized to their respective values (solid orange circle) at a fluence of  $0.04 \text{ mJ cm}^{-2}$  (5% surface excitation).

### 4.3.2 Coupling to Electronic and Librational Continua

The Ti-O surface localized vibration, as shown by Fano lineshapes, is coupled both to the electronic dynamics in the solid and solvent dynamics in the liquid, demonstrating the extent to which the mode is truly interfacial. In that it couples to the electron dynamics, the mode is similar to one of a small molecule (CO, methanol) adsorbed on a solid surface that exhibits Fano lineshapes because of the solid-state continuum.<sup>73,74</sup> On the other hand, the coupling of a molecular, surface localized vibration to solvent dynamics in the electrolyte is new. As will be shown below, the solvent dynamics the Ti-O stretch couples to are water librations and in that sense, the coupling exemplifies what has been expected of a catalytic intermediate, but had not yet been detected molecularly—namely the interaction of its vibrations with reactant dynamics.

A Fano lineshape occurs whenever a discrete mode, such as a vibration, couples to a broad continuum of excitations whose spectral weight crosses the mode frequency, creating a resonance between the mode and the continuum. The lineshape is characterized by the coupling constant,  $\Gamma$ , of the mode to the continuum and an asymmetry factor,  $q$ , that in turn depends on the screening of the mode by the continuum and the continuum density of states at the resonant frequency. The Fano lineshapes<sup>75</sup> and asymmetry factor  $q$  are defined rigorously by:

$$|\langle \Psi | T | i \rangle|^2 = A \left[ \frac{(q - \varepsilon)^2}{1 + \varepsilon^2} \right] + Y_0 \quad (4.3)$$

$$q^2 = \frac{2|\langle \Phi | T | i \rangle|^2}{\pi |\langle \psi | T | i \rangle|^2 \Gamma} \quad (4.4)$$

where  $\varepsilon = \frac{(\omega - \omega_0)}{2\Gamma}$  and  $\omega_0$  is the resonant frequency.  $|\langle \Psi | T | i \rangle|$  represents the transition matrix element of the coupled vibration and continuum that is measured by the spectroscopy and separated by theory into transition matrix elements of the screened vibration,  $|\langle \Phi | T | i \rangle|$ , and of the continuum excitations,  $|\langle \psi | T | i \rangle|$ . The asymmetry factor  $q$  is the ratio of the screened vibrations over the continuum excitations at  $\omega_0$ .  $A$  represents solely the continuum excitations that are coupled to the mode ( $|\langle \psi | T | i \rangle|^2$ ) and  $Y_0$  represents the uncoupled continuum excitations.

The asymmetry of the spectral line-shape changes drastically with n-doping, pH, and H/D exchange. Remarkably, the variations in lineshape are all described by changes in the magnitude of the asymmetry factor,  $|q|$ , that occur when the experimental conditions modify the extent to which continuum excitations are involved. The three characteristics of the Fano lineshape fit by  $|q|$  are a dip in spectral

weight prior to the resonant frequency, followed by a steep rise near the resonant frequency, and then a more gradual decay following the resonance. The magnitude of the asymmetry factor decreases with increasing spectral weight of the continuum that crosses the resonant frequency, either through screening (decreasing  $\Phi$  in the numerator,  $|\langle \Phi | T | i \rangle|$ ) or through a larger density of states (increasing  $\psi$  in the denominator,  $|\langle \psi | T | i \rangle|$ ). Accordingly, with higher doping at the air interface (Figure 4.8), the asymmetry factor changes from -3.7 (0.1% Nb) to -1.5 (0.7% Nb). The doping induced electronic continua that cross the resonant frequency near 795  $\text{cm}^{-1}$  are the electron plasma mode peaked at 400-500  $\text{cm}^{-1}$  and the Drude free electron peak.<sup>76</sup> Interestingly, the resonant frequency of the mode increases from 798-800  $\text{cm}^{-1}$  to 807-810  $\text{cm}^{-1}$  in the more highly doped samples (Table 4.1), which reflects an increase in the plasma frequency in this doping range<sup>76</sup> and suggests that plasma excitations are primarily involved.

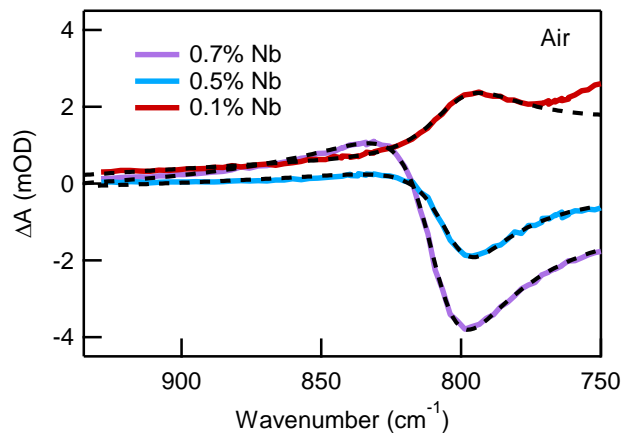


**Figure 4.8:** Transient spectra at 700 ps of 0.1% (red), 0.5% (cyan) and 0.7% Nb (purple) n-doped  $\text{SrTiO}_3$  in air. Modifying the n doping tunes the Fano lineshape associated with coupling to the plasma continuum in the solid.

Condition	Doping	$\omega_0$	q	A	$\Gamma$	$Y_0$	S
Air	0.7% Nb	807.7	-1.62	-1.58	29.6	1.25	120.41
	0.5% Nb	802.3	-2.29	-0.35	31.0	0.24	72.97
	0.05% Nb	797.6	-1.93	0.16	53.2	0.38	37.30
Electrolyte 1M NaOH	0.7% Nb	809.7	-0.16	-5.34	34.5	5.60	281.60
	0.5% Nb	808.9	-0.07	-3.97	31.5	4.50	195.68
	0.05% Nb	797.9	-1.98	0.09	44.5	0.32	18.80

**Table 4.1:** Fano parameters obtained for different dopings.

With the addition of electrolyte (Figure 4.9), a second continuum is introduced by condensed phase molecular water librations in this frequency range<sup>77</sup> and as a result, the magnitude of the asymmetry factor decreases further. The most striking lineshape change occurs for the Nb 0.5% and 0.7% doped samples. Here, continuum excitations due to both the electron plasma density and water librations have a large enough spectral weight at the resonant frequency that the vibration becomes a symmetric Lorentzian dip in the broad background of continuum excitations (this is the limit of  $q \sim 0$  for the Fano lineshape). As described by Fano's theory,<sup>75</sup> when two continua are involved in coupling to a single discrete mode, they introduce a significant, positive un-coupled background  $Y_0$  (purple dotted line in Figure 4.9); therefore, a true dip in spectral weight due to the vibration is only apparent after subtracting this un-coupled background.

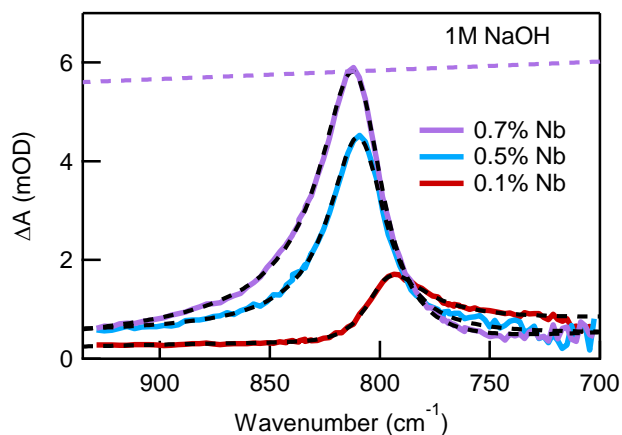


**Figure 4.9:** Transient spectra at 700 ps of 0.1% (red), 0.5% (cyan) and 0.7% Nb (purple) n-doped SrTiO<sub>3</sub> in 1M NaOH. Modifying the electrolyte conditions (air versus electrolyte) tunes the Fano lineshape associated with coupling to water librations.

The asymmetry factor also significantly responds to shifts within the librational continuum obtained by pH and H/D exchange. Changes to the asymmetry are most readily accessed via the Lorentzian lineshape of the 0.7% doped sample in normal water. The change in the asymmetry factor from  $q = -0.02$  in water to  $q = -0.44$  in deuterated water (Figure 4.10 a) is naturally explained by the librational frequency shift between H<sub>2</sub>O and D<sub>2</sub>O<sup>78</sup> resulting in less spectral weight at the resonant frequency. While the lineshape changes drastically with H/D exchange, the resonant frequency does not (Table 4.2); this means that the interfacial Ti-O mode does not involve a proton. There is, however, a distinct effect of pH on the resonant frequency,

red-shifting by  $\sim 3 \text{ cm}^{-1}$  from pH 14 to pH's lower than 13 (Figure 4.10 b). Since only at pH 14 do surface hydroxyls dissociate to form a primarily  $\text{Ti-O}^-$  terminated surface, this implies that the mode reporting on the  $\text{Ti-O}\cdot$  oxyl couples to librations that involve nearby adsorbed groups.

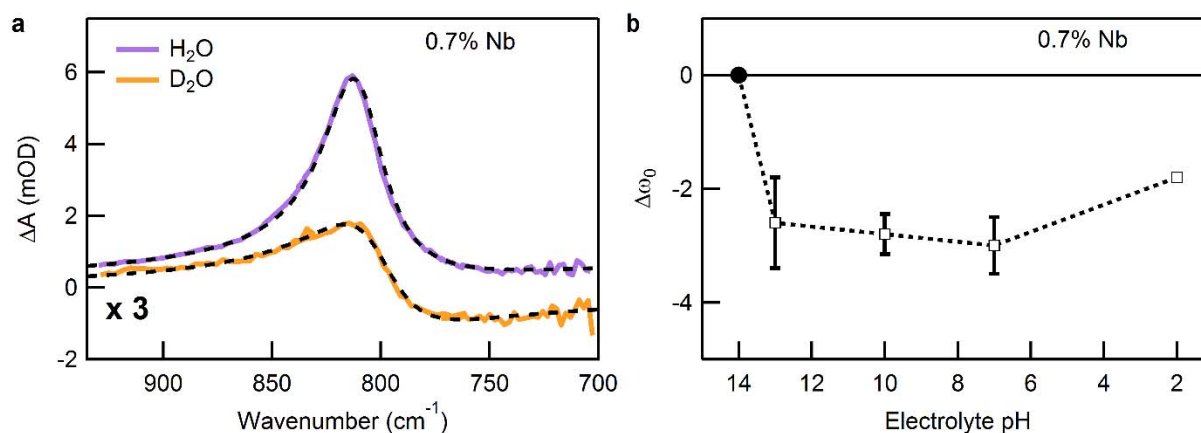


**Figure 4.10:** **a**, Transient spectra at 700 ps of 0.7% Nb (purple) doped  $\text{SrTiO}_3$  in 1M NaOD in  $\text{D}_2\text{O}$  (orange, scaled  $\times 3$ ). **b**, The underlying vibrational mode shows a consistent  $\sim 3 \text{ cm}^{-1}$  redshift when the solution pH is less than 14. Error bars show the standard error from four trials.

Condition	pH	$\omega_0$	q	A	$\Gamma$	$Y_0$	S
$\text{H}_2\text{O}$	14	809.7	-0.16	-5.34	34.5	5.60	281.60
	10	801.6	-0.10	-1.14	44.6	1.20	79.06
	2	803.7	-0.018	-1.09	36.8	1.23	61.24
$\text{D}_2\text{O}$	14	801.4	-0.63	-0.63	47.9	0.6	28.59
	10	801.2	-0.60	-1.33	44.0	1.18	58.83
	2	800.3	-0.45	-1.83	33.7	1.79	75.95

**Table 4.2:** Fano parameters obtained from H/D exchange in both acidic and basic conditions for the 0.7% Nb  $\text{SrTiO}_3$  sample.

The fact that the entire data set, despite the large changes in lineshape, can be fit with the expected modifications to the asymmetry factor demonstrates that the same Hamiltonian describing a localized, surface Ti-O vibration coupled to both the electron plasma density and water librations is involved throughout; the sign of the asymmetry factor is important in this consistency and arises in the context of continuum excitations that peak at lower energies than the mode. It is also important

that the width of the transition, given by a similar coupling strength  $\Gamma$  (30-45  $\text{cm}^{-1}$ ) across the data set, leads to a lifetime of  $\sim 1$  ps for the coupled mode, which confirms that the measured nanosecond kinetics (Figure 4.6 b) are that of a transient species rather than of a mode that decays into vibrational or electronic excitations. We note that some of the transition width fit by the coupling strength is likely un-related directly to the Fano lineshape and can instead be attributed to anharmonic phonon coupling, polaronic behavior of the trapped hole, and surface heterogeneity.

While the Fano lineshapes shown here primarily describe variations in the continuum spectral weight that couples to the mode (via  $q$ ), they also have the potential to describe variations in the coupling strength ( $\Gamma$ ) of the mode to solvent and electron dynamics, which are expected to occur especially as  $\text{Ti-O}\bullet$  evolves through a transition state and the O-O bond is formed.

The full range of doping and electrolyte conditions fit with the Fano lineshape, and details of the fits are discussed as follows. For the various experiments performed, the results were fit using Equation 4.5 as described by Fano<sup>75</sup> when considering the interaction of multiple continua with a discrete state.

$$|\langle \Psi | T | i \rangle|^2 = A \frac{(q + \frac{(\omega - \omega_0)}{\frac{1}{2}\Gamma})^2}{1 + \frac{(\omega - \omega_0)^2}{\frac{1}{2}\Gamma}} + Y_0 \quad (4.5)$$

In equation 4.5,  $A$  represents the transition probability  $|\langle \Psi_{E1} | T | i \rangle|^2$  to continua that interact with the discrete state transition, and  $Y_0$  represents a transition probability  $|\langle \Psi_{E2} | T | i \rangle|^2$  arising from continua that do not couple to the discrete state.  $Y_0$  is a nearly energy independent offset (slope  $< 0.004 \frac{\Delta mOD}{\text{cm}^{-1}}$  identified by fitting a line to the region 850 – 950  $\text{cm}^{-1}$ , where the discrete state contribution is minimal.  $\Gamma$  represents the coupling between the discrete state and the continuum. The factor  $q$  is defined as the ratio of the transition matrix element of the initial state to the discrete state (modified by interaction with the continua), over the transition matrix element between the initial state and the continuum states (over a bandwidth given by  $\Gamma$ ). Phenomenologically, the value of  $q$  is dictated by the asymmetry of the resulting lineshape (negating  $q$  is equivalent to reversing the abscissa axis). Finally,  $\omega_0$  is the observed resonance energy corresponding to excitation to the discrete state modified by interaction with the continuum. The parameter values used in fitting our results in air and electrolyte, as well as figures showing fits, are found in Table 4.1

and Figure 4.11 respectively.  $\Gamma$  (the continua/discrete state coupling) is roughly constant as a function of doping, and does not change appreciably in the presence of electrolyte. In contrast  $q$  changes with both doping and the presence of electrolyte. The resonant frequency  $\omega_0$  is consistently found to be 797-802  $\text{cm}^{-1}$  in air and electrolyte, although it increases to 807-810  $\text{cm}^{-1}$  for the 0.5% and 0.7% Nb doped samples. The coupled-continua transition probability ( $A$ ) increases with doping and further with the presence of electrolyte. The Fano fits require that for the more highly doped samples (0.5%, 0.7%),  $A$  is negative, while for the less doped samples (0.05%, 0.1%), it is positive. Justification for this is that the plasma mode can significantly change the dielectric constants of reflectivity for the 0.5% and 0.7% doped samples in this wavenumber range (Figure 4.5) and that differential reflectance, even if coming from an additional absorption, can appear either as a positive or negative absorbance change.<sup>79,80</sup>

The matrix elements that define  $q$  are:

$$q = \frac{(\varphi|T|i)}{(V_E + W_E)(\Psi_E|T|i)} + \frac{\int \frac{dE'(V_{E'} + W_{E'})(\Psi_{E'}|T|i)}{E - E'}}{(V_E + W_E)(\Psi_E|T|i)} \quad (4.6)$$

Here  $V_E$ ,  $W_E$  represent the coupling of the vibration ( $\varphi$ ) to the electronic, librational continua respectively.  $E$  is the resonance energy,  $E'$  the energy that spans through both continua, and  $\Psi_{E'}$  represents both continua. Fano has shown that the presence of two continua does not change the form of the Fano equation, but only add an additional smooth background, described further below.

While the sign of the first term is due to the phases of the wave-functions involved, the sign of the second term is always positive for continua that peak at lower energy than  $E$  (when  $(E - E') > 0$ ). Since the electron plasma density and the librations are the only continua that we know of that can extend to  $E$  and they become large for lower energies, the sign of  $q$  cannot be determined by the second, screening term. Therefore, the consistent negative values suggest that the first term is dominant and the phases of the wavefunctions make it negative. The first term could be dominant in many considerations of the Fano lineshape, since it involves the wavefunctions in the region near the resonance energy  $E$ . The relative phases of the wavefunctions cannot be predicted without more extensive calculations.

From this starting point, we can rationalize the changes in the magnitude of  $q$  with the changes in the density of states of the two continua. As the electronic continuum increases with doping, we expect the magnitude of the first term (negative) to decrease and the contribution of the screening term (positive) to increase. This then

results in a lower  $|q|$  with doping, as exhibited in the table above. In a similar manner, the addition of a librational continuum can explain why  $|q|$ , for a given doping, decreases in electrolyte. The contribution from the librational density of states will decrease upon H/D exchange. This explains why  $|q|$ , for the 0.7% doped sample in deuterated electrolyte, is lower than in air, but larger than in pH 14 electrolytes. In the lower doped, 0.1% sample, the changes in  $q$  between air and electrolyte are not as pronounced and  $q$  doesn't change in deuterated electrolyte. The less pronounced effect of the librational continuum on  $q$  may have to do with the fact that the denominator in the first term is already small due to a much lower electronic continuum. Indeed, if a consistent relative phase of the wavefunctions determines the first term above despite the presence of two continua, one of the continua, likely the electron doping, determines this phase.

The relative importance of the continuum to the signal can also be seen in the differential signal amplitude ( $A$  in the table), representative of transitions within the continuum. As expected within this interpretation, the amplitude is highest in the case of the more highly doped samples in electrolyte.

Finally, the presence of two continua also means that there will be a large, smooth background on top of the original Fano lineshape given by:

$$\sqrt{(V_E^2 + W_E^2)} |(\Psi_E | T | i)|^2 \quad (4.7)$$

We find that the 0.7% doped and 0.5% doped samples in electrolyte have a large uncoupled continuum, close to the magnitude of the Fano signal. These are exactly the two cases when  $q$  changes significantly with the librational continuum, suggesting that two full continua are involved through  $V_E$  and  $W_E$ . The presence of this large uncoupled continuum is why the data look like Lorentzian peaks rather than Lorentzian dips within a coupled continuum, described by the  $q \rightarrow 0$  limit of the Fano lineshape. A Lorentzian peak is associated with the  $q \rightarrow \infty$  limit. However, the  $q \rightarrow \infty$  limit means that a continuum is not significantly contributing ( $A \rightarrow 0$ ), while experimentally the Lorentzians occur when the electronic and librational continua are maximally involved.

There is another solution set for the Fano fitting, if one explores the case when the differential signal amplitude ( $A$ ) is positive for all dopings. In this case, one has to interpret the Lorentzians of 0.5% and 0.7% in the  $q \rightarrow \infty$  limit. As described, this minimum is not physically matched with the experimental conditions. Furthermore, the fits require  $q$  to change sign and to span -2 to 15 non-monotonically with changes in the continuum density of states. The screening term would have to dominate some

of the time and not in others. Finally, these fits also require a large uncoupled continuum (of the order the Fano signal) to be added to the 0.5% and 0.7% doped samples in air (rather than in electrolyte), where two clear continua do not exist.

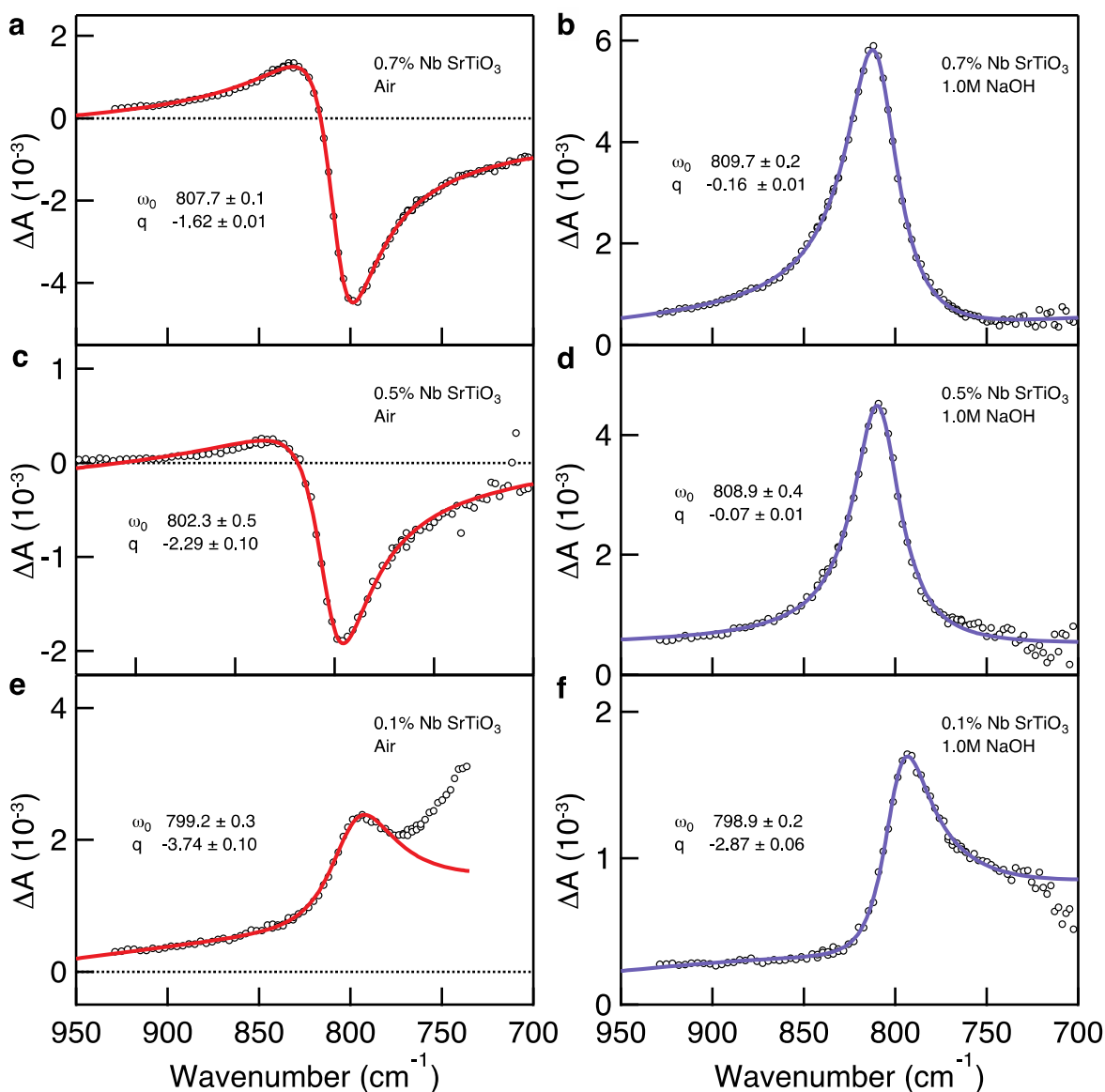


**Figure 4.11:** Full spectra of variously doped samples in air and electrolyte. Transient spectrum of doped SrTiO<sub>3</sub> in air and electrolyte with doping concentration **a, b**, 0.7% Nb, **c, d**, 0.5% Nb, **e, f**, 0.1% Nb. Spectra were fit with Equation 4.5 describing a Fano resonance. Full fitting parameters found in Table 4.1.

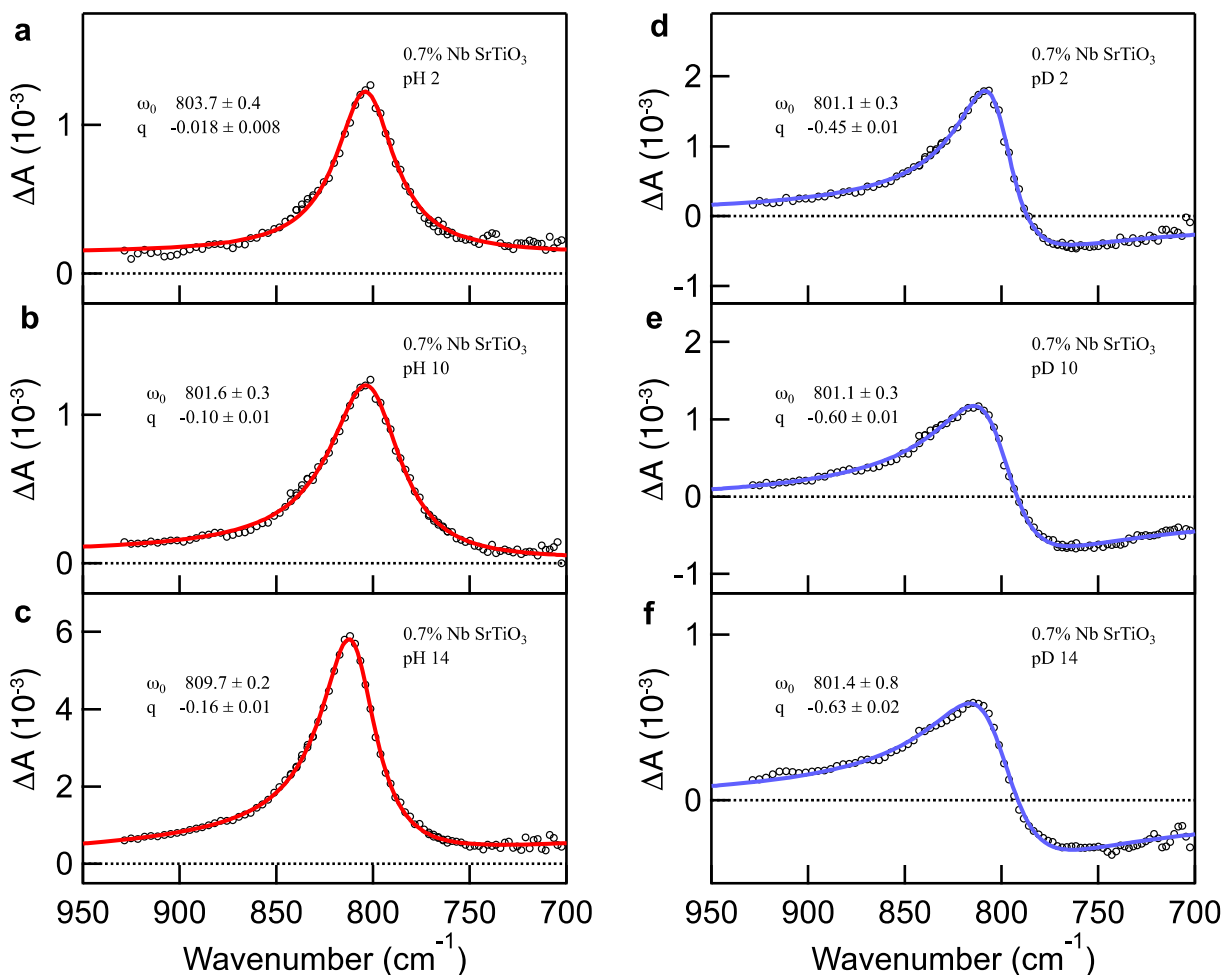


**Figure 4.12:** Full spectra in different pH and pD electrolyte. Transient spectrum of 0.7% doped SrTiO<sub>3</sub> in **a – c**, H<sub>2</sub>O with different pH and **d – f**, D<sub>2</sub>O with different pD.

All the above considerations are made in the case where there is no direct coupling between the two continua, which is the first order effect considered by Fano.

### 4.3.3 Theory of Interfacial Ti-O• and its Surface Modes

The data demonstrate that a transition dipole for a surface-localized, Ti-O vibration becomes bright whenever a hole sits at the surface. Therefore, we consider a water-adsorbed and undoped SrTiO<sub>3</sub>/air interface with holes as the starting point for a more detailed, molecular description of the vibration and the associated transient species using first-principles theory. At equilibrium, we find a partially

dissociated configuration ( $C_{GS}$ ), wherein 50% of adsorbed water molecules lose an H atom to one of the lattice surface oxygen atoms and hydroxyl-water dimers form (Figure 4.3). In the photo-excited configuration ( $C_{oxyl}$ ), the hole is localized on an O adatom ( $O_x$ ) and there are two hydroxyl groups on the surface  $TiO_2$  layer (Figure 4.3 b). O sites on the surface-terminating  $TiO_2$  layer of the STO slab are henceforth referred to as lateral oxygen to distinguish them from the oxygen of adsorbed water or hydroxyl groups. Our calculations indicate that the configuration in which the hole is localized at  $O_x$  is the lowest in energy by 0.46 eV. Furthermore, localizing the hole at a lateral oxygen surface site does not lead to P-polarized vibrations, as observed in experiment.

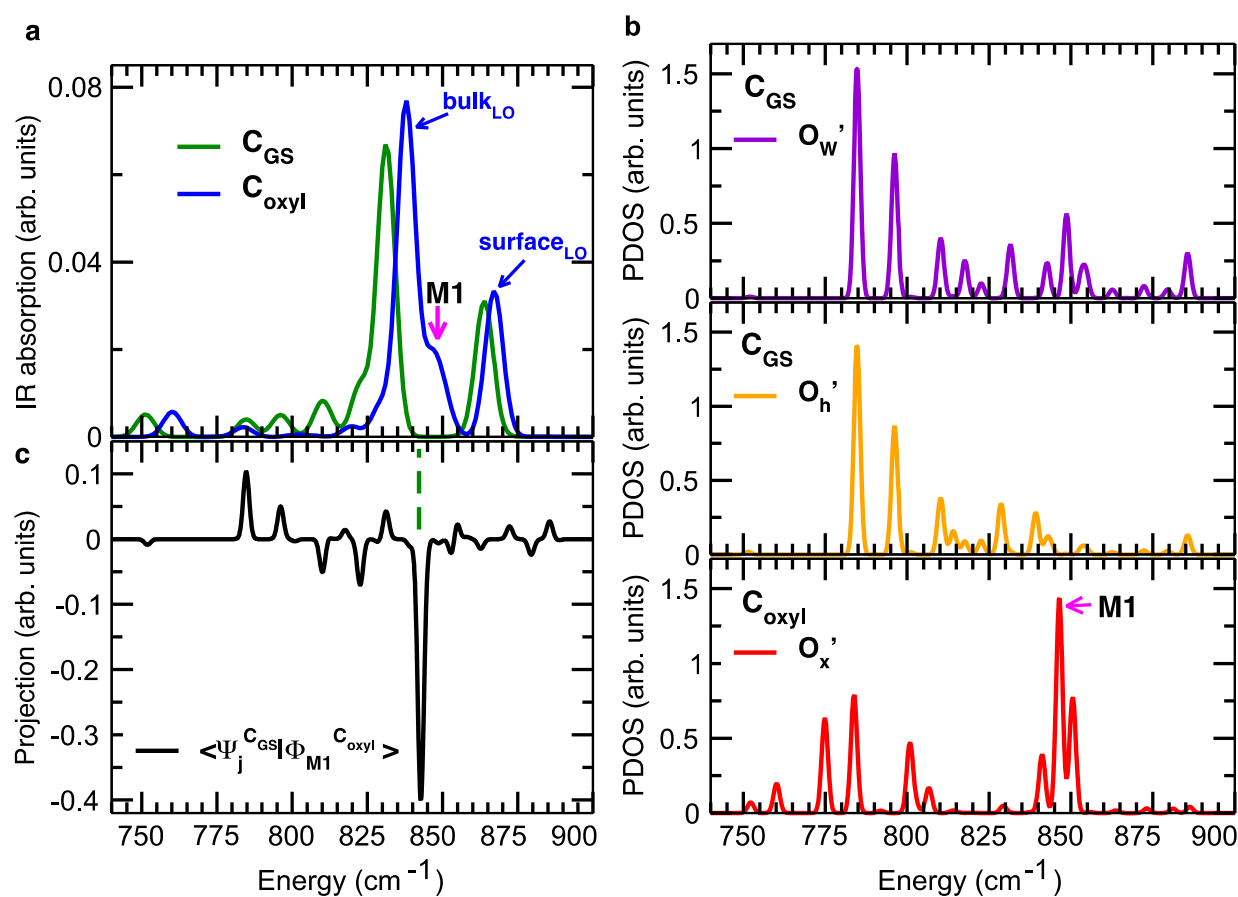


**Figure 4.13:** **a**, Infrared activity of the slab for  $C_{GS}$  and  $C_{oxyl}$  where M1 indicates the new surface mode upon creating the oxyl. **b**, Partial density of states of  $O_w'$  sites in  $C_{GS}$  (top),  $O_h'$  in  $C_{GS}$  (middle) and  $O_x'$  in  $C_{oxyl}$  (bottom). **c**, Projection of the eigenvector of mode M1 in  $C_{oxyl}$  on the phonon eigenvectors of  $C_{GS}$ , where the primary contribution comes from a dark breathing mode at 843  $cm^{-1}$

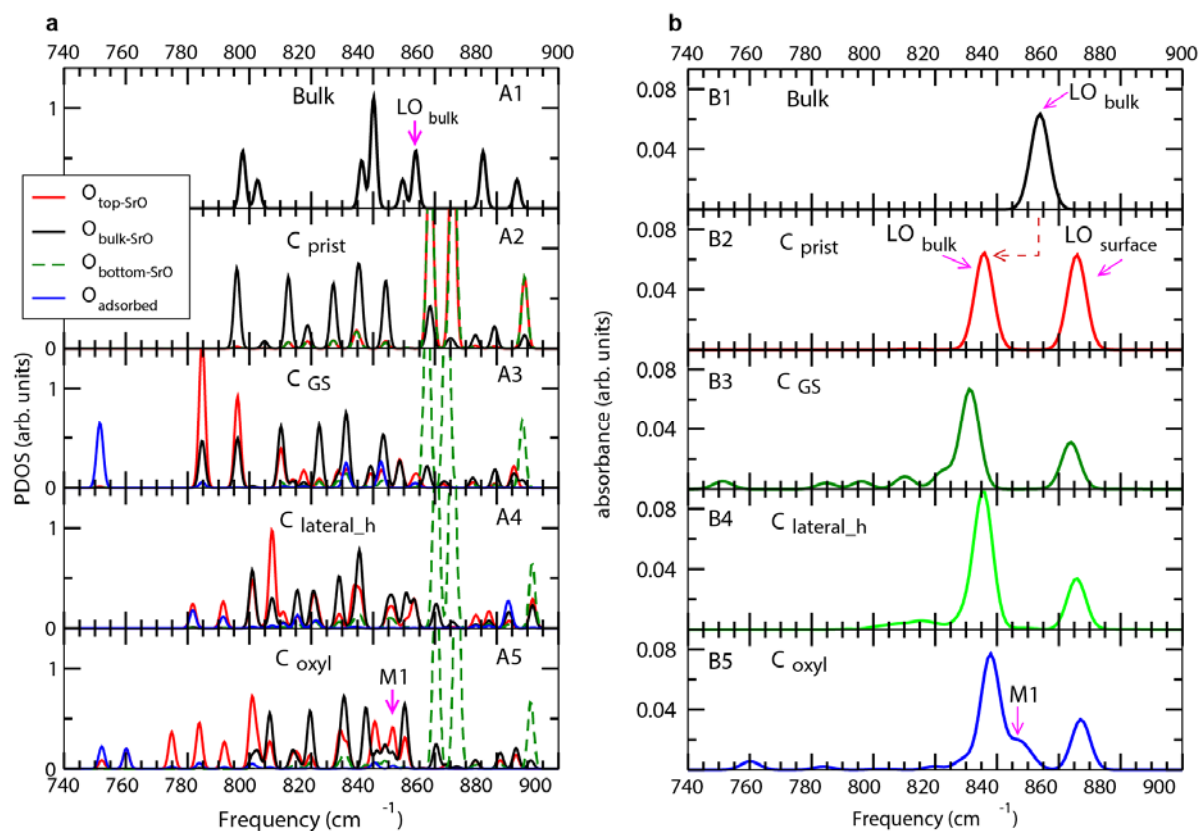


**Figure 4.14:** **a**, Projected densities of states (PDOS) averaged over selected O sites from the bulk and slab geometries.  $\text{O}_{\text{top-SrO}}$ ,  $\text{O}_{\text{Bulk-SrO}}$ ,  $\text{O}_{\text{Bottom-SrO}}$ ,  $\text{O}_{\text{adsorbed}}$  represent collective labels for O sites in the top-most SrO layer, middle four SrO layers, bottom SrO layer and surface adsorbed species, respectively. In particular, sites contained within  $\text{O}_{\text{top-SrO}}$  are individually labeled as  $\text{O}_w'$ ,  $\text{O}_h'$ ,  $\text{O}_x'$  etc. in Figure 4.13 **b**, Calculated IR absorbance corresponding to the configurations represented in **a**.

Phonon frequencies and eigenvectors for configurations  $\text{C}_{\text{GS}}$ ,  $\text{C}_{\text{oxy}}$ , and a pristine surface are calculated using a density functional finite difference approach, and associated infrared absorption oscillator strengths are obtained using an established methodology.<sup>81</sup> The dominant motion for the Ti-O modes observed in P-polarization (perpendicular to the surface) is related to either the O in SrO layers or the adsorbed atoms at the surface ( $\text{O}_w$ ,  $\text{O}_h$ ,  $\text{O}_x$ ) defined in Figure 4.3. The vibrations of O sites within the SrO layers can be divided into bulk O modes ( $\text{O}_{\text{bulk-SrO}}$ ), sub-surface O modes of the un-terminated layer ( $\text{O}_{\text{bottom-SrO}}$ ), and the sub-surface O modes of the terminated layer ( $\text{O}_w'$ ,  $\text{O}_h'$  and  $\text{O}_x'$ ). In both  $\text{C}_{\text{GS}}$  and  $\text{C}_{\text{oxy}}$ , the bulk LO Ti-O mode occurs near 835  $\text{cm}^{-1}$  (bulk LO in Figure 4.13 a). A surface infrared active LO Ti-O mode of  $\text{O}_{\text{bottom-SrO}}$  occurs at 866  $\text{cm}^{-1}$  (surface LO in Figure 4.13 a).

The significant difference in infrared activity between  $C_{GS}$  and  $C_{\text{oxyl}}$  appears at  $846 \text{ cm}^{-1}$  (Figure 4.13 a) where  $O_x$  is decoupled from the  $O_w$ ,  $O_h$  motion and dominates the projected phonon density of states (PDOS) (Figure 4.13 b and Figure 4.14). As can be seen from projecting the new eigenstate (M1 in Figure 4.13 a) in  $C_{\text{oxyl}}$  on the  $C_{GS}$  eigenstates, the dominant contributor to M1 is an originally dark (infrared-inactive) mode in  $C_{GS}$  at the same energy and the remaining spectral weight is distributed among many (infrared active and dark) modes in  $C_{GS}$  (Figure 4.13 c). The dark breathing motion in  $C_{GS}$  (Figure 4.3 a) is disrupted by a new large amplitude motion on  $O_x$  (Figure 4.3 b). We can assign M1 to the Ti-O infrared activity seen experimentally because: (1) it occurs at a frequency  $\approx 10 \text{ cm}^{-1}$  above the bulk LO Ti-O mode; (2) it is associated with an oxyl radical, or a photo-hole active site; (3) it is associated with a completely new absorption cross-section not seen in the ground state; (4) it does not involve a proton; and (5) the infrared activity comes from a sub-surface layer whose motion is P-polarized and can readily couple to bulk and surface water librations. We note that experiment does not observe an isotope shift upon  $O^{16}/O^{18}$  surface exchange and theory confirms this for M1 (Figure 4.15).

Furthermore, as shown in Figure 4.13 a, M1 is the distinctive infrared mode associated with the oxyl radical. One might also expect to observe a beating mode of the surface oxyl Ti- $O_x$  bond itself, but only weak and spectrally broad IR activity is predicted for motions of Ti- $O_x$  at the fully water-adsorbed surface; hydrogen bonding strongly hybridizes the motion of  $O_x$  with nearby surface-adsorbed water groups. Thus, a pure Ti- $O_x$  beating mode is not expected to be a stable vibrational eigenstate of the oxyl radical.

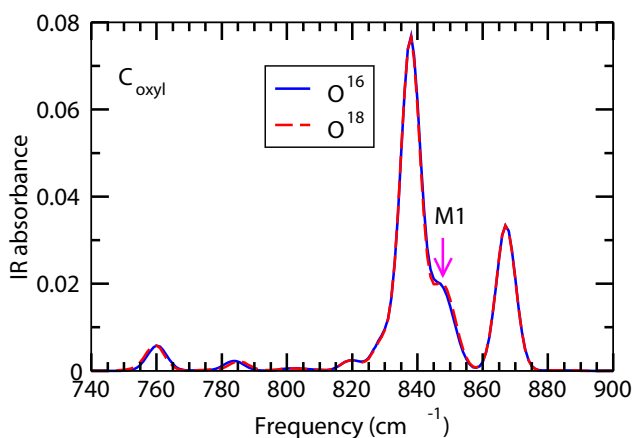


**Figure 4.15:** Calculated IR absorbance for the  $C_{\text{oxyl}}$  configuration with and without  $O^{18}$  isotope exchange within the surface adsorbed species.

## 4.4 Discussion

Together, experiment and theory molecularly detect the transformation of charge into a Ti-O• oxyl radical through a well-defined sub-surface vibration of the O directly below it. The oxyl radical is formed within picoseconds, i.e. at the point of charge transfer, and remains present for at least nanosecond time scales. This means we can use changes in this sub-surface vibration in time to track the formation of later time scale intermediates of the water oxidation cycle at a transition metal oxide surface. While some of the molecular intermediates of the cycle can be followed by the new bonds that are created on the surface, as done in other laboratories, the decoupling of the sub-surface vibration from the lattice could be the distinctive vibrational mode of the transformation of charge into a catalytic intermediate prior to bond formation, not only for the oxyl radical, but more generally. The vibration of the adsorbed atom involved in creating the new bond is likely well-hybridized with reactants, as is the case for the Ti-O<sub>x</sub> beating mode. While the sub-surface vibration has the integrity of a spectrally defined mode, we have discovered that it still couples the oxyl radical to its immediate surroundings. Both the coupling strength ( $\Gamma$ ) and the involvement of the continuum excitations ( $q$ ), through Fano lineshapes, describe how the sub-surface vibration couples to solvent and electron dynamics. This coupling opens opportunities for tracking and influencing the dynamics of the reaction pathway directly through the local electrolyte environment and the electronic plasma density in the solid. In particular, coupling of the vibrations of the oxyl radical to different local electrolyte environments could strongly alter the dynamics of how it transforms into the O-O bond. Broadly speaking, the methods shown here to study nascent catalytic intermediates and how they interact with the solid-liquid interface open up a new field of investigating catalytic dynamics from the point of charge transfer and then successively through the molecular intermediates of the cycle.

## 4.5 Conclusion

We have identified the initial intermediates of water oxidation on n-SrTiO<sub>3</sub> in its molecular form, Ti-O• or oxyl radical with ultrafast infrared spectroscopy. The generation of oxyl radical will induce a subsurface Ti-O vibration that uniquely occurs in P polarization. This vibrational mode could couple to both side of the solid-liquid interface, making it a special reporter for initial intermediates of water oxidation reaction.

## Chapter 5

# Probing initial intermediates of water oxidation on n-SrTiO<sub>3</sub> with electronic spectroscopy

*Portions of the content and figures of this chapter are reprinted or adapted with permission from Chen, X.; Choing, S.; Aschaffenburg, D. J.; Pemmaraju, C. D.; Prendergast, D. and Cuk, T. J. Am. Chem. Soc. 139, 1830 (2017).*

### 5.1 Introduction

At solid-liquid interface, catalysis proceeds by localizing charge carriers from the bulk to the surface, creating a surface population of radicals that can form bonds. Charge can localize at the surface in several different molecular forms, including at in-plane or axial, terminating surface sites, on different terminating elements of the compound, and with dissimilar atomic arrangements of the surface.<sup>51,53,82,83</sup>

At the surface of semi-conductors, localized charge that results from a surface termination or surface trap creates mid-gap electronic states that one can probe spectroscopically. Transient optical spectroscopy of semiconductor interfaces effectively uses this spectroscopic marker to report on surface recombination dynamics.<sup>35,84</sup> As a form of localized charge, surface bound water oxidation radicals should also form mid-gap states. The optical transitions of these radicals in principle can be isolated from the charge carrier signal by probing the mid-gap states they generate with a suitable, sub-band gap wavelength and in a surface sensitive optical geometry.

Here, transient optical spectroscopy of efficient, photo-catalytic water oxidation at the single crystal n-SrTiO<sub>3</sub>/aqueous interface, probed by 400 nm and white light in reflectance, isolates the formation dynamics of distinct water oxidation radicals. The distinct formation dynamics define two classes of radicals: one occurring with a  $1.3 \pm 0.2$  ps time constant, and another occurring upon a delay of 4.5 ps, with a  $36 \pm 10$  ps time constant. The  $1.3 \pm 0.2$  ps time constant is identical to the early time dynamics of a sub-surface vibration induced by an axial radical, the titanium oxyl (Ti-O•),<sup>85</sup> assigned previously near  $800\text{ cm}^{-1}$ . While this assigns a formation rate to

the oxyl radical, it is not the only radical created at the aqueous interface with this time constant. Uniquely observed here in relation to a transition metal oxide/aqueous interface, a predominantly in-plane dipole moment characterizes the stimulated emission transition between the conduction band and mid-gap states. Theoretical calculations show that a fully in-plane dipole describes bridge radical transitions (Ti-O•-Ti), while the oxyl's transition is un-polarized. Further, the voltage dependence observed for the mid-gap electronic state differs markedly from the oxyl's voltage dependence observed through its vibration. Finally, spectrally and dynamically resolving the white light probe demonstrates the importance of the sequential 1.3 ps, 4.5 ps, and 36 ps formation dynamics over a broad probe region that emulates photoluminescence. Altogether, the polarization of the optical transition's dipole moment, the disparate voltage dependence observed optically and vibrationally, and this broad optical emission, assigns the 1.3 ps time constant to populating a surface with the limiting forms of single O-site radicals, e.g. the oxyl and bridge radicals. We cannot yet assign a molecular form to the 36 ps radical, but an oscillatory component to the time trace distinguishes its formation from the 1.3 ps rise. Reaction conditions (applied voltage, surface excitation) modify the surface radical population, but conserve the formation dynamics. As would be expected of localized charge in the form of single O-site based radicals that count charge, the 1.3 ps radicals, measured specifically by the oxyl's vibration, decay with the overall surface charge measured by the transient photocurrent.

The formation dynamics are unique to the reactive, aqueous interface, conserved under disparate reaction conditions, and describe diverse radical species. Therefore, interfacial water dynamics should separately define them. Intriguingly, hydroxyl stretch relaxation at solid-liquid interfaces occurs with a 1.3 ps time constant.<sup>86</sup> Further, the two concomitant time constants of  $\sim 2$  ps and  $\sim 4$  ps are observed for hydroxyl stretch relaxation in dilute H-bond networks of isotopically mixed water solutions.<sup>86-89</sup> Namely, a hydroxyl stretch relaxes into lower energy modes of neighboring water molecules after which the water equilibrates through H-bond breaking. Thereby, the following non-adiabatic kinetic mechanism for generating oxyl and bridge radicals is proposed: The hole carrier, initially at a high potential energy with respect to the radicals, releases some of its energy to create a hydroxyl stretch (0.3 eV) of surface adsorbed or interfacial water. The hydroxyl stretch relaxation (1.3 ps) reorganizes neighboring water molecules, which facilitates reaching a transition state common to oxyl and bridge radicals. Upon radical formation, a period of H-bond equilibration ( $\sim 4$  ps) follows.

## 5.2 Experimental Configuration

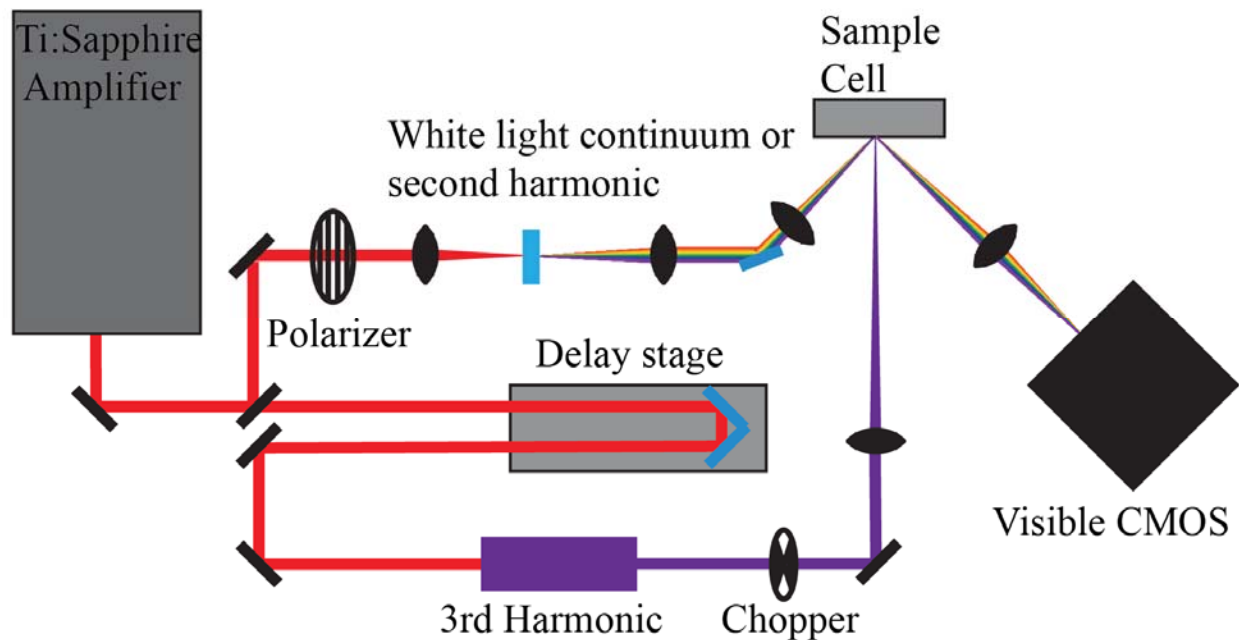


**Figure 5.1:** Representation of ultrafast optical laser setup.

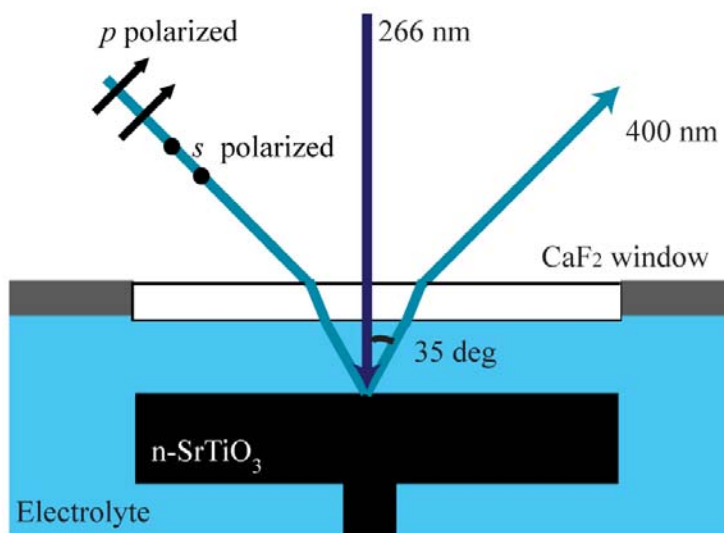


**Figure 5.2:** Representation of ultrafast optical experimental geometry. The s- or p-polarized 400 nm probe beam incident on the sample at an angle of  $35^\circ$  to the normal.

The laser setup is briefly shown in Figure 5.1. All spectroelectrochemical measurements were performed in a Teflon electrochemical cell with  $\text{CaF}_2$  optical windows (3 mm thick). The electrolyte was a 0.1 M aqueous solution of sodium hydroxide for all experiments, unless otherwise noted. The electrolyte was in contact with the atmosphere during measurements. The potential of the n- $\text{SrTiO}_3$  photoelectrode with respect to an Ag/AgCl (3M KCl) reference electrode (MF-2052; Basi, West Lafayette, IN) was controlled by a CHI650E Potentiostat (CH Instruments, Austin, TX). A Pt wire served as the counter electrode. Ohmic contact between the unpolished n- $\text{SrTiO}_3$  backside and copper wire was established using Gallium-Indium eutectic (Sigma-Aldrich, St. Louis, MO). For the transient reflectance experiments, an insulating lacquer covered all surfaces except the polished front side of the crystal. Transient optical and infrared measurement procedure were described elsewhere.<sup>84,85</sup>

Density functional theory (DFT) calculations were carried out using the Vienna Ab initio Simulation Package (VASP) which employs a planewave basis set and Projected Augmented Wave<sup>90,91</sup> pseudopotentials.

### 5.3 Results

The perovskite n- $\text{SrTiO}_3$  (100)/aqueous interface forms an interfacial electric field that separates photo-generated electron-hole pairs, as depicted in Figure 5.3. The water oxidation reaction is initiated by exciting above the band gap (3.25 eV) with a 266 nm (4.66 eV), 500 Hz, 150 fs laser pulse. Photo-holes generated in the O 2p valence band efficiently migrate to the surface. A number of different O-site radicals could be formed, such as  $\text{Ti-O}\cdot$  and  $\text{Ti-O}\cdot\text{-Ti}$ ,<sup>92</sup> and each should correspond to a mid-gap state within the n- $\text{SrTiO}_3$  semiconductor, as depicted in Figure 5.3.

In the following section, we use a sub-band gap, 400 nm probe in reflectance and during water oxidation at 0 V to isolate the radicals' optical transitions. In reflectance, the optical penetration depth is 12 nm according to  $d=\lambda/4\pi n$ . For measurements that utilize the polarization properties of the 400 nm probe, the incident angle to the sample is determined to be  $35^\circ$  (Figure 5.2). While s-pol( $0^\circ$ ) always refers to a fully in-plane probe polarization, p-pol( $90^\circ$ ) contains an out-of-plane component defined by the incident angle. The properties of the absorption change reported are exclusively associated with the reactive, aqueous interface: they vanish in methanol or deionized water and reduce in pH 7 compared to pH 13 (Figure 5.4). The time constants are identical for a 0.1% and 0.7% Nb-doped  $\text{SrTiO}_3$  crystal (Figure 5.5).

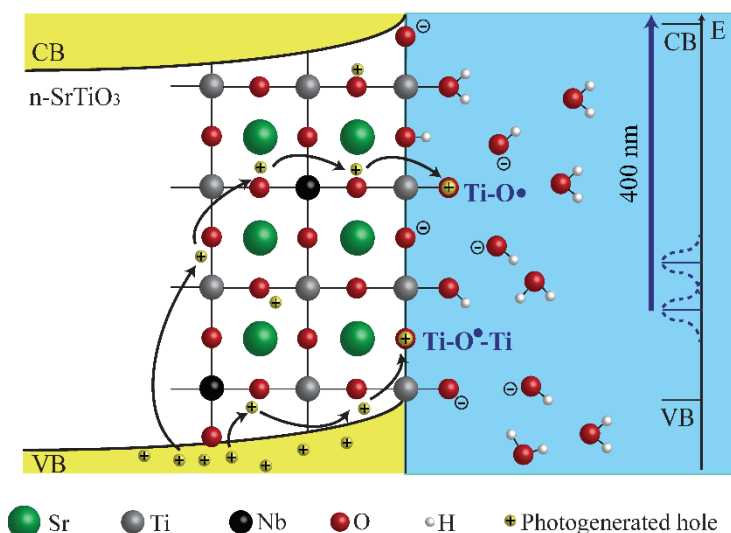


**Figure 5.3:** Representation of n-SrTiO<sub>3</sub> photo-electrode after bandgap (266 nm) photoexcitation. Photo-holes in the valence band of n-SrTiO<sub>3</sub> migrate to the surface to create O-site radicals: the titanium oxyl (Ti-O<sup>•</sup>) and the bridge (Ti-O<sup>•</sup>-Ti) radicals. These radicals create mid-gap states, whose optical transition to the conduction band minimum is excited by 400 nm light.

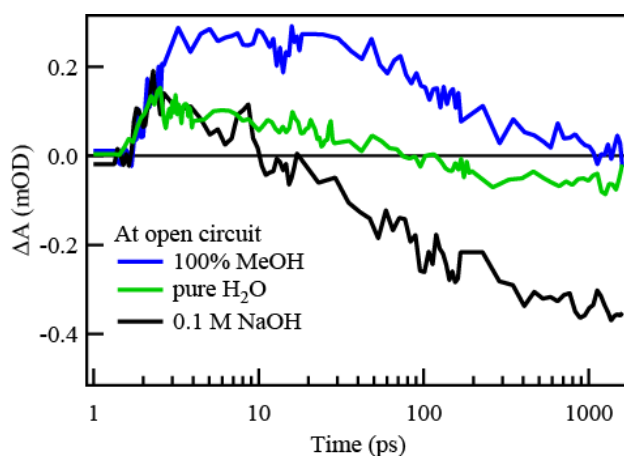


**Figure 5.4:** Kinetics of the transient response at open circuit with a 400 nm probe, where the sample is in contact with pure water (green), 100% methanol (blue), and 0.1M NaOH (black) solution. Clearly, the negative absorption vanishes in pure methanol and the amplitude is decreased in pure water.

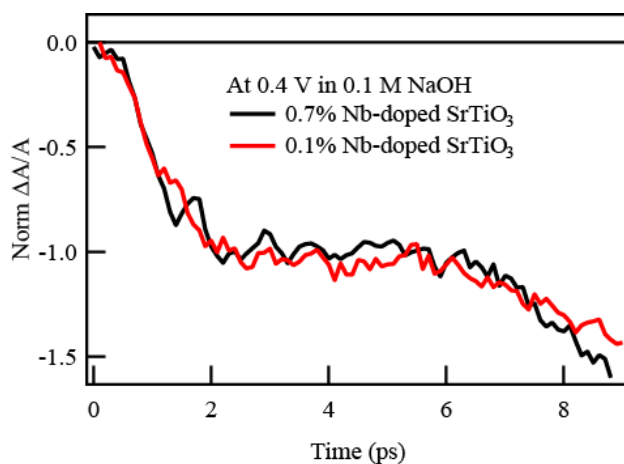


**Figure 5.5:** Kinetics of transient response for 0.1% and 0.7% Nb-doped SrTiO<sub>3</sub> (n-SrTiO<sub>3</sub>) at +0.4 V applied bias from 0 ps to 9 ps in 0.1 M NaOH solution. When normalized, no difference can be observed in kinetics for 0.1% and 0.7% Nb-doped SrTiO<sub>3</sub>.

We note that during current evolution, the sample surface changes. Therefore, we confirm the same kinetics on a pristine surface at open circuit. At higher electron energies, the sample post-catalysis still exhibits a LEED pattern of the 1x1 surface; a negligibly small amount of metal dissolution results from current evolution (Figure 5.6 and Figure 5.7).

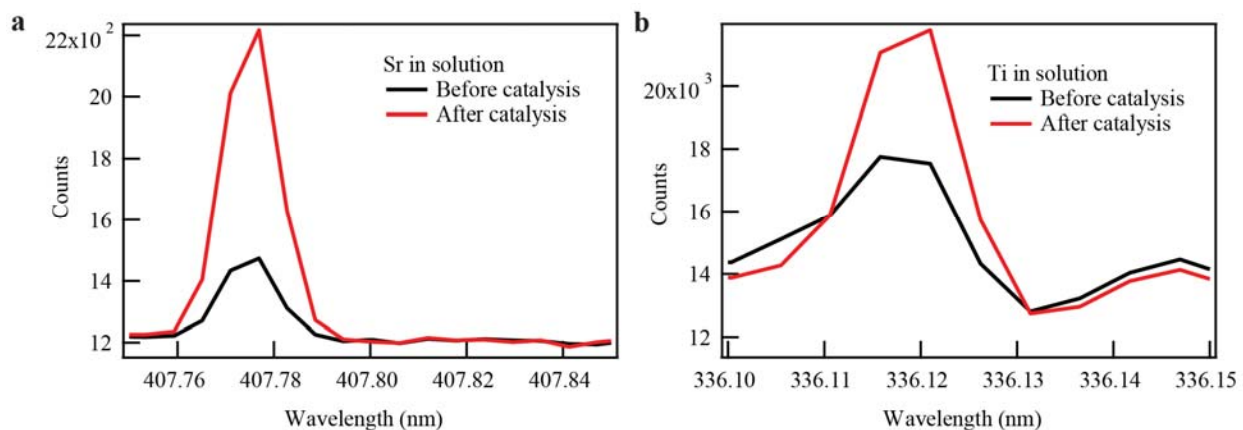


**Figure 5.6:** **a**, ICP spectra for Sr metal in solution before and after catalysis. **b**, ICP spectra for Ti metal in solution before and after catalysis. Very minimal photo-dissolution happened on n-SrTiO<sub>3</sub> surface.

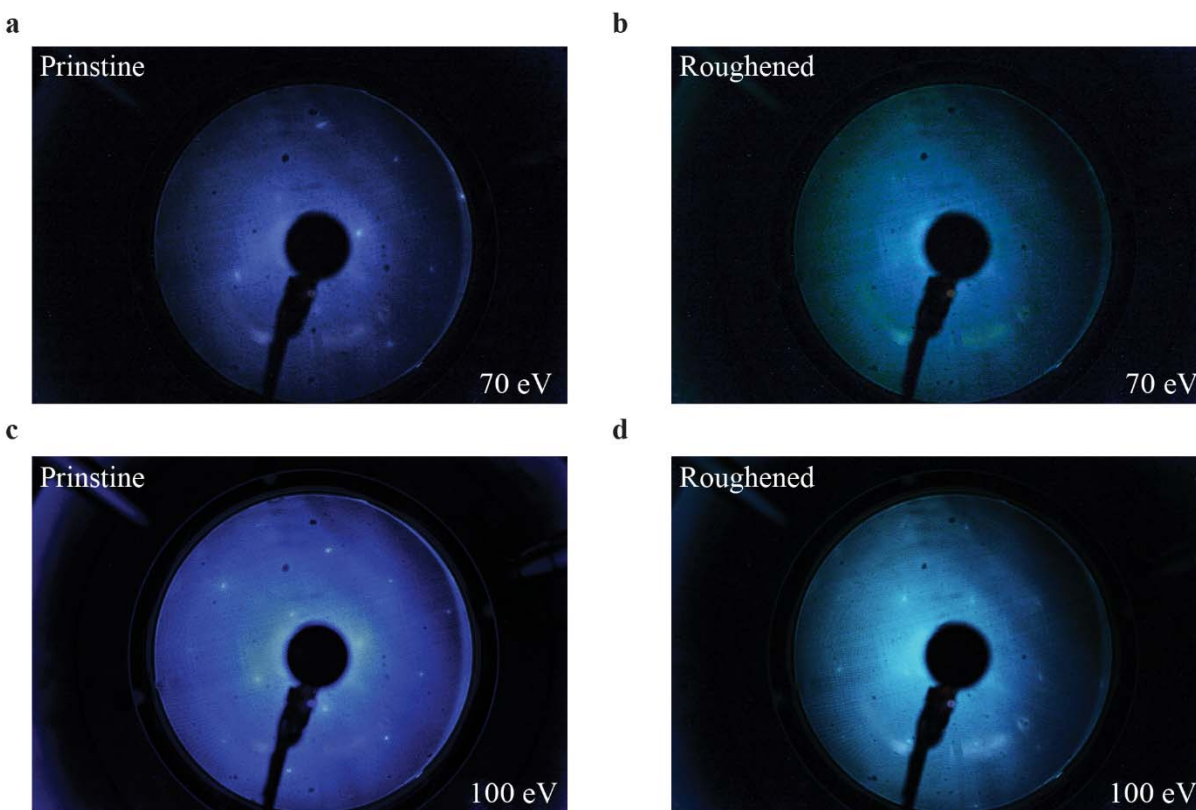


**Figure 5.7:** LEED pattern showing laser-induced roughening on n-SrTiO<sub>3</sub>. **a**, LEED pattern of pristine sample at 70 eV. **b**, LEED pattern of laser roughened sample at 70 eV. **c**, LEED pattern of pristine sample at 100 eV. **d**, LEED pattern of laser roughened sample at 100 eV.

ICP analysis is also performed to examine photodissolution during catalysis. Figure 5.6 a shows the Sr concentration in solution increasing after catalysis taken place. Figure 5.6 b shows the same is happening to Ti. Quantitatively, according to the calibration curve for Sr and Ti, the concentration for both species is 5 ppb which corresponds to a molar concentration of  $1.71 \times 10^{-8}$  M for both species. Totally 10 ml of solution is used, which gives a total of  $1.71 \times 10^{-10}$  mol Sr and Ti in solution. To electrochemically dissolve one mole Sr, 2 moles of electrons are needed as Sr has the form of Sr<sup>2+</sup> in SrTiO<sub>3</sub> crystal. Then, total number of charges to needed to dissolve Sr will be  $1.71 \times 10^{-10} \text{ mol} \times 2 \times N_A \times 1.6 \times 10^{-19} \text{ C} = 3.3 \times 10^{-5} \text{ C}$ . Typical day of experiments transfer total of 0.182 C of charge, therefore, the efficiency for photodissolution of Sr is  $\frac{3.3 \times 10^{-5} \text{ C}}{0.182 \text{ C}} \times 100\% = 0.018\%$ . Same procedure is applied to Ti and Ti has the form of Ti<sup>4+</sup>. So the efficiency for

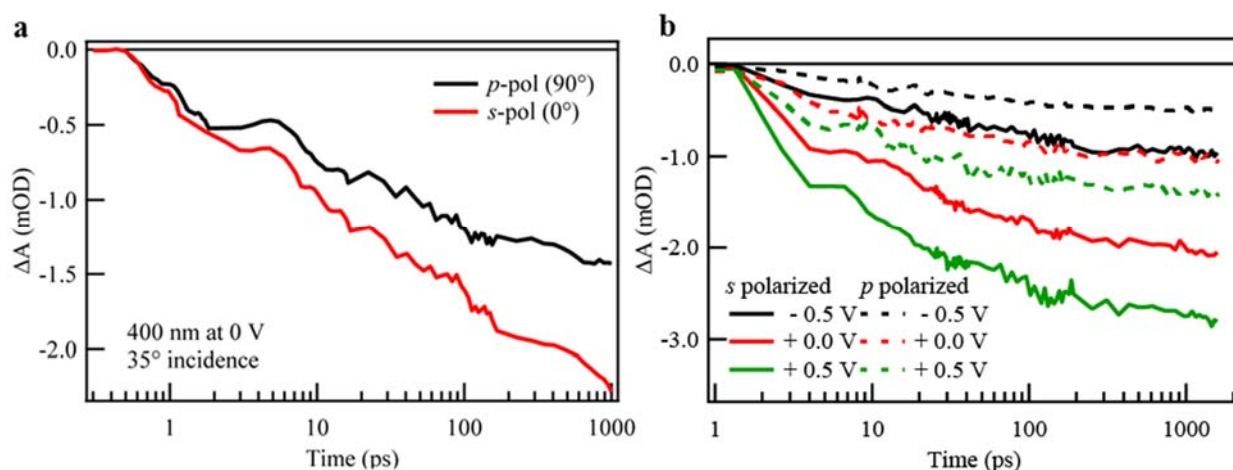
photodissolution of Ti is  $\frac{6.6 \times 10^{-5} C}{0.182 C} \times 100\% = 0.036\%$ . Total efficiency for electrochemical photodissolution is then  $0.018\% + 0.036\% = 0.054\%$ .

Figure 5.7 a shows the pristine surface has  $1 \times 1$  surface reconstruction at 70eV, which suggests a cubic surface structure. Figure 5.7 b shows the roughened surface has no ordered  $1 \times 1$  surface reconstruction at 70eV, indicating roughened surface is not having cubic geometry and some reconstruction is happening. When 100 eV is used, both pristine and roughened sample have  $1 \times 1$  surface reconstruction as shown in Figure 5.7 c and Figure 5.7 d. This indicates the major crystal structure is not affected by roughening, but rearrangement is happening on the surface only. The detailed mechanism for this rearrangement is still unknown.

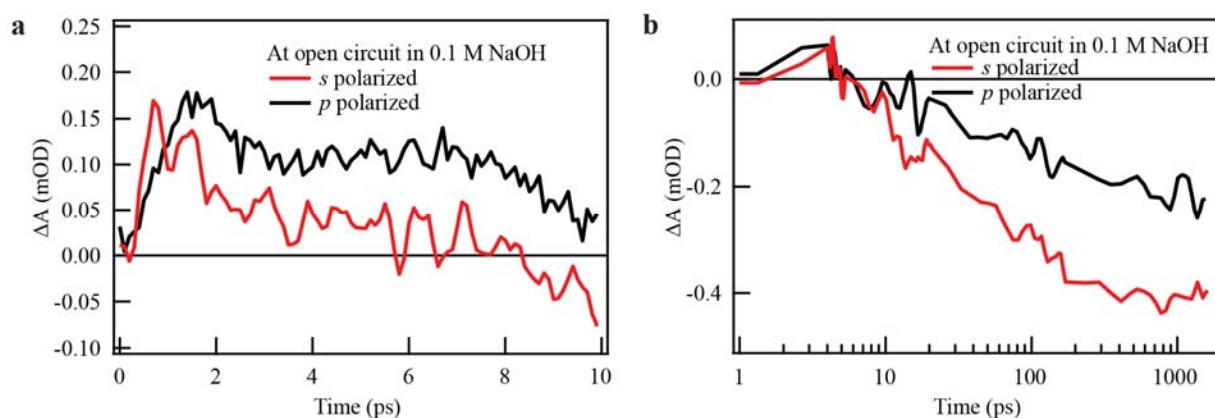
### 5.3.1 Formation time constant of Oxy & Bridge Radicals

Figure 5.8 shows the kinetic trace of the 400 nm probe at 0 V. We convert the transient change in reflectance to a change in absorption, according to  $\Delta A = -\log(R_{on}/R_{off})$ . There are two transitions to consider for hole-related mid-gap states: the transition of an electron deeper in the valence band to the mid-gap state, leading to an absorption, and the transition of an electron in the conduction band to the mid-gap state, leading to stimulated emission. The emissive, charge transfer transition between Ti 3d conduction electrons and the O 2p mid-gap states should have a much larger cross-section. Indeed, the negative absorption change suggests emission and in this spectral region, emission is expected by SrTiO<sub>3</sub> photoluminescence.<sup>35,93</sup> Employing Beer's law and with all the holes generated by the laser pulse reaching the surface at 0 V and 0.05 mJ/cm<sup>2</sup>, the cross-section is on the order of a charge-transfer transition,  $\sim 10,000 \frac{L}{mol-cm}$ . We note that since the absorption change relates to the very surface of the sample and the n-SrTiO<sub>3</sub> substrate is transparent to 400 nm light, the limit of a thin absorptive film on a transparent substrate likely applies. Therefore, the reflectance is interpretable in terms of the film's absorptive properties.<sup>79,94</sup>

We observe that the absorption change has a polarized transition optical dipole. Therefore, given the symmetric electronic structure of n-SrTiO<sub>3</sub> along  $x$ -,  $y$ -,  $z$ - axes, it relates to a surface species. The absorption change is greater in  $s$ -polarization of the 400 nm probe than in  $p$ -polarization (Figure 5.8 a for 0 V, Figure 5.8 b for other voltages). The same polarization dependence occurs at open circuit, with a pristine surface (Figure 5.9). At an incidence angle of 35°, the ratio of  $p$ -pol/ $s$ -pol is 0.78. Since a fully in-plane optical dipole would lead to a ratio of 0.67 at 35° incidence, this demonstrates a strong in-plane component to the measured absorption change.



**Figure 5.8:** Time-resolved reflectivity after 266 nm light excitation probed with 400 nm light. **a**, trace on the nanosecond time scale for both s (red) and p (black) polarization at 0 V, where the ratio of the s/p absorption change is 0.78 probed at 35° **b**, trace on the nanosecond time scale for both s (red) and p (black) polarization at -0.5 V, 0 V and + 0.5 V at 45° incidence.



**Figure 5.9:** **a**, Kinetics of transient response for the pristine 0.1% Nb-doped SrTiO<sub>3</sub> at open circuit at early times. Photoexcitation induces bulk absorption that is positive in sign. Right after that, the fast 1.3 ps component of the negative absorption occurs with larger amplitude for the s polarized probe. **b**, Transient response for the same sample at open circuit from 0 ps to 1.6 ns. At late times, the 36 ps component of the negative absorption occurs with larger amplitude for the s polarized probe.

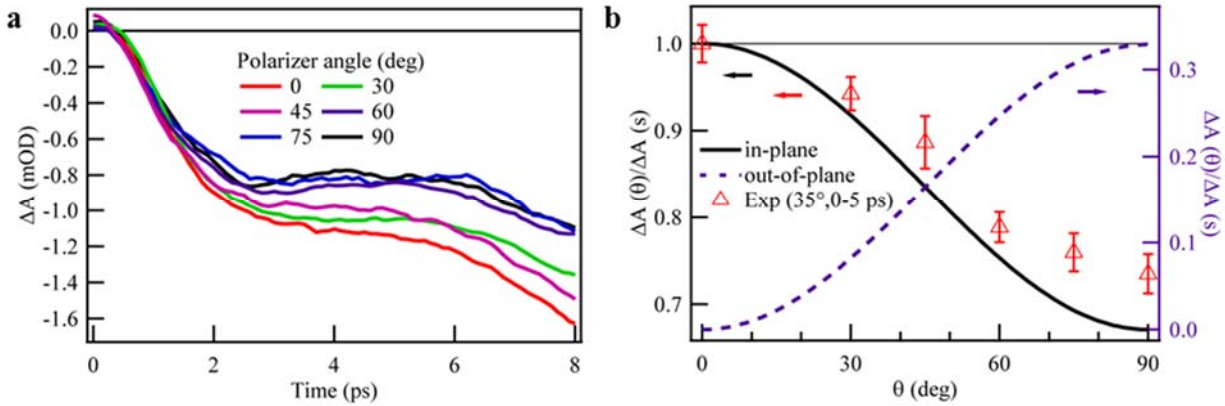


**Figure 5.10:** **a**, Kinetics of transient response for the pristine 0.1% Nb-doped SrTiO<sub>3</sub> at 0 V from 0 ps to 10 ps with different polarizer angle. 0 deg indicates s polarization and 90 deg indicates p polarization for the probe light. The amplitude of the 1.3 ps rise component is used to construct Figure 2B. **B**, A version of Figure 2B with the predicted dependence for an out-of-plane dipole in the experimental geometry, as described below.

Next, the fact that the absorption change increases in time allows us to assign distinct formation times to the surface species. As shown in Figure 5.11, the data can be fit with two rising exponentials separated by a delay. The first exponential rise, after convolution with the instrumental response function, has a time constant of  $1.25 \pm 0.06$  ps. The second exponential rise has a time constant of 36 ps. A delay in the range of 3-5.5 ps from time 0, when the first rising exponential begins, is required to fit the data with 4.5 ps the best fit. An oscillation, attributable to a 0.11 THz coherent acoustic phonon of SrTiO<sub>3</sub>,<sup>95</sup> accompanies the second rising exponential (this oscillation is cosine filtered from the data shown in Figure 5.8 for clarity). The 4.5 ps delay and this oscillation separate the second time constant from the first, such that the fit represents the addition of two species that form independently. The fitting function used is described by equation 5.1.

$$f(t) = \frac{1}{2} A_1 \cdot \left\{ \text{Erfc} \left[ \frac{-\sqrt{2}(t-t_0)}{W} \right] - e^{\frac{1}{8} \frac{W^2}{\tau_1^2}} \cdot e^{\frac{-(t-t_0)}{\tau_1}} \cdot \text{Erfc} \left[ \frac{W}{2\sqrt{2}\tau_1} - \frac{\sqrt{2}(t-t_0)}{W} \right] \right\} + A_2 \cdot H(t_1) \cdot \left( 1 - e^{\frac{-(t-t_1)}{\tau_2}} \right) + A_3 \cdot H(t_1) \cdot \cos[\omega(t-t_1) + T_0] \cdot e^{\frac{-(t-t_1)}{\tau_3}} \quad (5.1)$$

$A_1$  is the maximum transient signal before 6 ps,  $t_0$  is the time at which pump and probe pulses overlap and  $\tau_1$  is the time constant for the first exponential rise

component.  $A_2$  is the maximum transient signal difference between 1 ns and 6 ps,  $H(t_1)$  is the Heaviside function,  $t_1$  is the time at which the second rise start (6 ps in our case) and  $\tau_2$  is the time constant for the second exponential rise.  $A_3$  is the oscillation signal caused by coherent phonon,  $\omega$  is the oscillation frequency,  $T_0$  is the phase of oscillation and  $\tau_3$  is the lifetime of the coherent phonon.

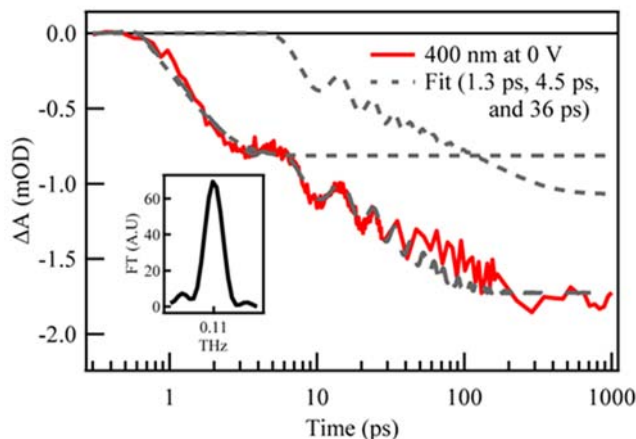


**Figure 5.11:** Nanosecond trace with higher time resolution in s-polarization (red). The fit, consisting of two independent, rising exponentials, is shown with the two exponential components (1.3 ps, 36 ps) separated (grey, dashed) and added (dark grey, dashed). The fit includes a delay of 4.5 ps between the start points of the two exponentials. The second exponential contains an oscillatory component with a frequency of  $\sim 0.11$  THz. The frequency is obtained by a Fourier Transform of the data (inset).

We now focus on the assignment of the first, 1.3 ps time constant, by using additional spectroscopic signatures of the local electronic structure of the intermediates. In other words, we relate the time constant to the population of the surface with particular, stable intermediates. Previously, by ultrafast mid-infrared spectroscopy on the same n-SrTiO<sub>3</sub> surface,<sup>85</sup> we identified the oxyl radical (Ti-O•) through a subsurface Ti-O vibration in the plane right below it (Figure 5.12 inset). As shown in Figure 5.12, the rise time of the oxyl's subsurface vibration taken at its peak (800 cm<sup>-1</sup>) is identical to the 1.3 ps rise of the mid-gap state. In order to establish this correspondence, both the optical and infrared time traces were taken with 100 fs time steps between 0 and 8 ps under identical reaction conditions of 0.05 mJ/cm<sup>2</sup>, 266 nm laser excitation and 0 V applied bias.

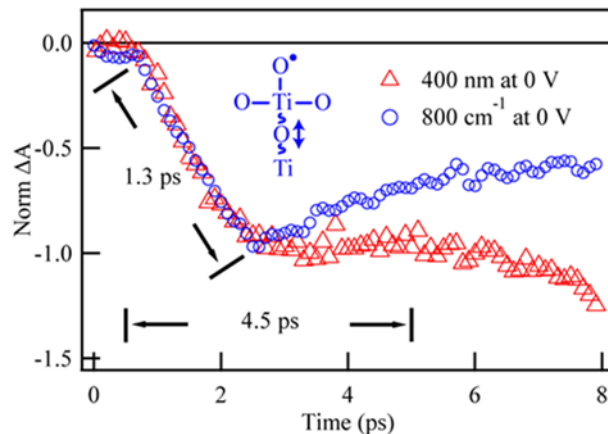


**Figure 5.12:** The optical (400 nm, red open triangles) and mid-infrared (800  $\text{cm}^{-1}$ , blue open circles) traces from 0 to 8 ps; both are taken at 0 V.

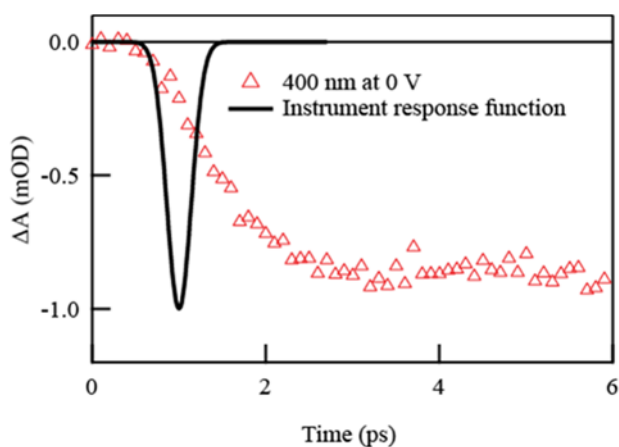


**Figure 5.13:** Kinetics of transient response for the 0.1% Nb-doped  $\text{SrTiO}_3$  at 0 V (open red triangles) with instrumental response function (black) overlaid. Instrumental response function has a Gaussian pulse width much smaller than the rise function.

The rise time between 0 and 2 ps is well within the resolution of our experiment with a Gaussian instrument response time of 200 fs (Figure 5.13). Two additional experiments confirmed this response time: the faster formation time for surface charge on a different sample (n-GaN) (Figure 5.14 a) and for high light excitations of n- $\text{SrTiO}_3$  at open circuit where a bulk carrier component is present (Figure 5.14 b). The rise of the bulk carrier component occurs simultaneously with the light excitation. It is significantly faster than the rise time of the mid-gap state and

therefore defines time zero in Figure 5.12; the 0.5 ps delayed onset represents the bulk carrier component that only becomes visible at open circuit (Figure 5.14 b).

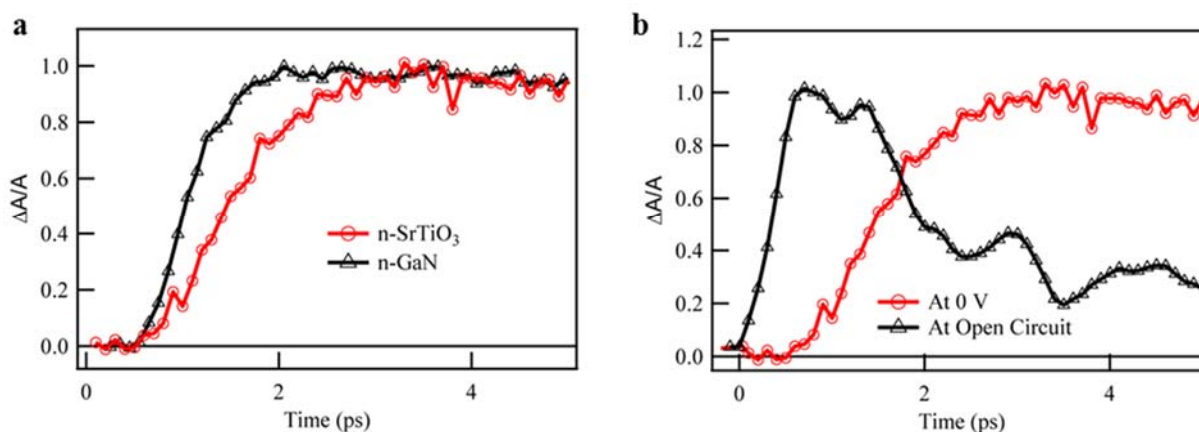


**Figure 5.14:** **a**, Kinetics for the 0.1% Nb-doped SrTiO<sub>3</sub> at 0 V (red) compared with n-GaN (black). Fine time steps of 100 fs are taken. By fitting, GaN has a faster rise (0.63 ps) compared to n-SrTiO<sub>3</sub> (1.3 ps). **b**, The normalized kinetics for the 0.1% Nb-doped SrTiO<sub>3</sub> at 0 V (red), open circuit (black) in 0.1 M NaOH solution. Time zero is identified with the rise of the free carriers at open circuit and the formation of radicals has a delay of 0.5 ps count from time zero. Also, the rise time for photogenerating free carriers is much faster than for the radicals.

These experiments represent a unique achievement in that they map a vibrational signature of a particular radical to an electronic one in time. In interpreting this result, the formation dynamics associated with the vibrational signature are considerably more complex. Multiple physical processes are involved: charge localization to the surface, the development of the radical's vibration, and the coupling of the vibration to neighboring modes. Given its high energy (100 meV), we expect the oxyl's vibration to develop immediately upon the localization of charge to the surface (within 100's fs). However, as demonstrated previously,<sup>85</sup> the sub-surface vibration does couple to neighboring modes: to solvent (water librations) and electron (plasmon) excitations. The coupling leads to a distinctive Fano resonance between the discrete vibration and two broad (electron, solvent) continua.<sup>75</sup> The time it takes for the resonance to establish, then, complicates assigning a time constant for populating the surface with oxyl radicals. Further, the width of the vibration ( $\sim 30$  cm<sup>-1</sup>) leads to a  $\sim 1$  ps vibrational lifetime, similar to the rise time of the mid-gap state. While this similarity could be of

importance to the kinetic mechanism below or simply coincidental, it does mean that during this time the vibration de-phases and populates neighboring modes.

In contrast to the subsurface vibration, the mid-gap state, by being a purely electronic signature, is insensitive to excitations in the local environment. Therefore, it is exactly through mapping the formation of the mid-gap state (400 nm) to the rise of the oxyl's vibration ( $800\text{ cm}^{-1}$ ) that we isolate the time constant for populating the surface with oxyl radicals. The evolution of the Fano resonance in time is not limited to this population time. Rather, the Fano resonance evolves over 6 ps, with the major changes concomitant with the sharp drop in the time trace (2-6 ps) (Figure 5.12 and Figure 5.15). Interestingly, these major changes in the Fano resonance occur over a  $\sim 4$  ps time interval that tracks the delay in the mid-gap state, for which the implications will be discussed below.

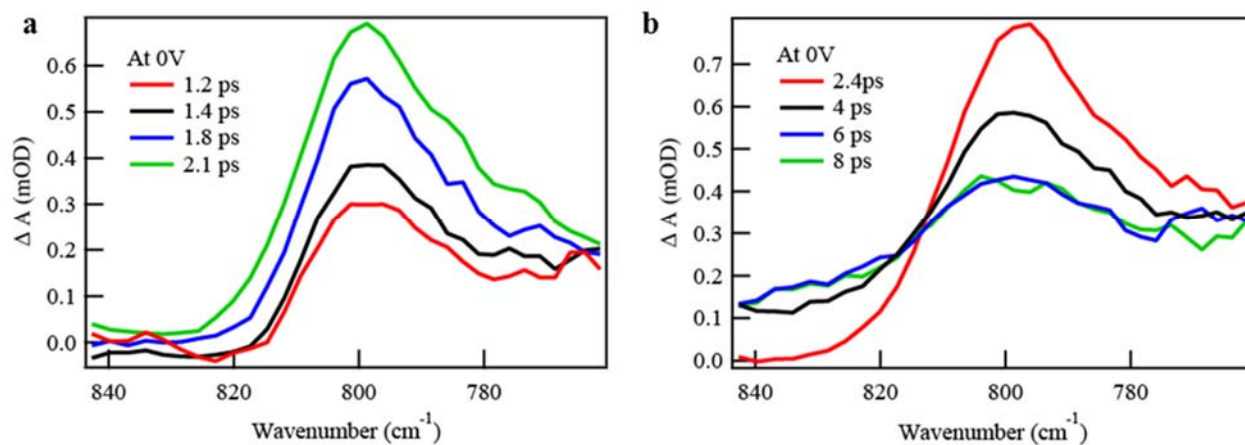


**Figure 5.15:** Spectra of photo induced absorption for the 0.1% Nb-doped SrTiO<sub>3</sub> at **a**, 1.2 ps (red), 1.4 ps (black), 1.8 ps (blue) and 2.1 ps (green) **b**, 2.4 ps (red), 4 ps (black), 6 ps (blue) and 8 ps (green). A near Lorentzian shape peaked at  $798\text{ cm}^{-1}$  is observed and rises in amplitude from 1.2 ps to 2.1 ps. Then from 2.4 ps to 6 ps, the Lorentzian lineshape becomes significantly broadened, while the peak frequency blue shifts to  $802\text{ cm}^{-1}$ . Finally, the lineshape stabilizes and remains unchanged after 6 ps.

Another spectroscopic signature of the local electronic structure of the surface species is the polarized transition optical dipole. In order to characterize the polarization properties more quantitatively, we measured the absorption change between 0-5 ps as a function of the probe polarization. At the incident angle of  $35^\circ$ , the 400 nm polarization was tuned from an *s*-polarized ( $\theta = 0^\circ$ ) probe to a *p*-polarized

( $\theta = 90^\circ$ ) probe. In this geometry, the s-polarized ( $0^\circ$ ) probe is fully *in-plane*, whereas the p-polarized ( $90^\circ$ ) probe is a ratio of *out-of-plane* to *in-plane* components defined by the incident angle.

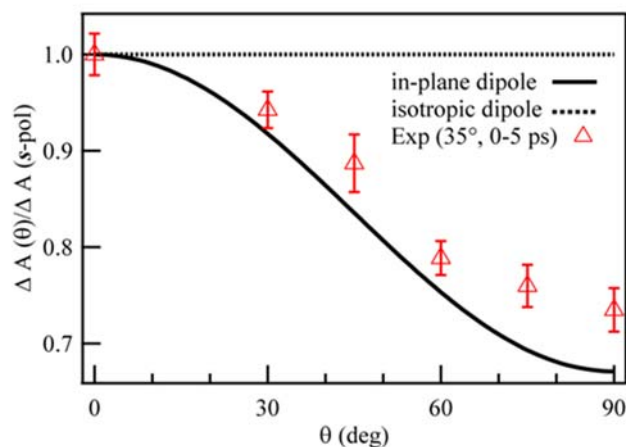


**Figure 5.16:** Polarization dependence of the absorption change reported as  $\Delta A(\theta)/\Delta A(s-pol)$  (red, triangle) and compared to that predicted for transitions with a fully *in-plane* optical dipole moment (black, solid line) and isotropic dipole moment (black, dashed line). The standard error is calculated from three experimental runs for data between 0-5 ps.  $\theta$  is the polarizer angle, tuned between s-polarization ( $0^\circ$ ) and p-polarization ( $90^\circ$ ).

Figure 5.16 reports the absorption change at each angle with respect to the absorption change for the s-polarized ( $0^\circ$ ) probe:  $\left(\frac{\Delta A(\theta)}{\Delta A(s-pol)}\right)$ . For radicals with transitions characterized by totally *in-plane* optical dipole moments, the  $\theta$ -dependence of the ratio is  $\frac{\Delta A(\theta)}{\Delta A(s-pol)} = (\cos(\theta))^2 + (\cos(35^\circ))^2(\sin(\theta))^2$  (solid black line, Figure 5.16); no  $\theta$ -dependence is expected for radicals with transitions characterized by isotropic dipole moments (dotted black line, Figure 5.16) and the opposite  $\theta$ -dependence is expected for radicals with transitions characterized by fully *out-of-plane* dipole moments (Figure 5.10 b). The measured ratio largely tracks the *in-plane* prediction, which means that a specific type of radical that has a predominant *in-plane* transition optical dipole populates the surface. At large  $\theta$  that maximizes the *out-of-plane* component, the measured ratio deviates from the fully *in-plane* prediction. The assumption of two radical species with similar optical cross-sections, but oppositely polarized dipole moments, suggests a  $\sim 80/20$  ratio of radicals with *in-plane* to *out-of-plane* optical dipole transitions.

### 5.3.2 Theoretical calculation of transition optical dipoles of Bridge & Oxyl radicals

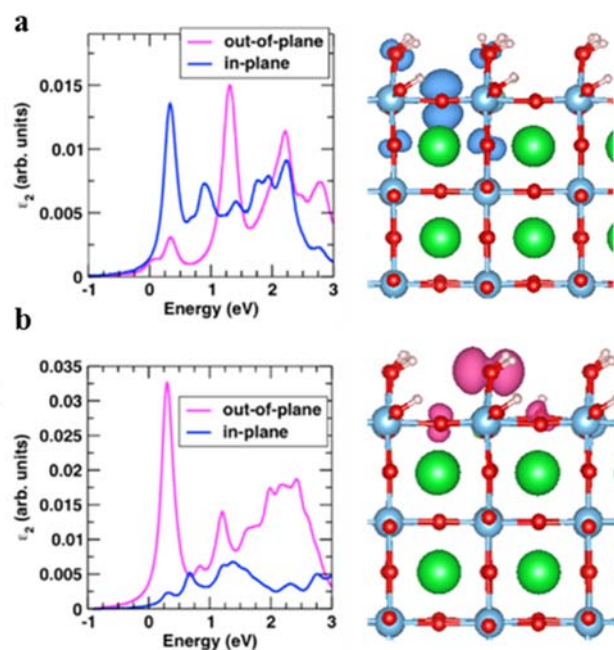


**Figure 5.17:** Theoretical calculation of optical transition dipole strengths. **a**, (left) Intensity and polarization dependence of optical transitions between the mid-gap bridge (Ti-O•-Ti) surface hole radical and the conduction band of SrTiO<sub>3</sub>. Since absolute transition energies are not calculated, for clarity, the energy of the transition to the lowest conduction band state is referenced to 0.0 eV. (right) Spin density isosurface (purple) for the localized bridge surface radical is shown. **b**, (left) Intensity and polarization dependence of optical transitions between the mid-gap surface oxyl (Ti-O•) hole state and the conduction band of SrTiO<sub>3</sub>. For clarity, the energy of the transition to the lowest conduction band state is referenced to 0 eV. (right) Spin density isosurface (deep-blue) for the localized oxyl surface radical is shown.

We now turn to the theoretical calculations that assign the *in-plane* optical dipole moment to bridge radical transitions and the *out-of-plane* optical dipole moment to oxyl radical transitions. First-principles density functional theory (DFT) simulations were performed to investigate the light-polarization dependence of emissive

transitions between conduction band states and localized mid-gap hole radical states at the SrTiO<sub>3</sub> surface. A 384-atom supercell (Figure 5.17) consists of a 7-layer SrTiO<sub>3</sub> slab terminated on either side by TiO<sub>2</sub> layers and functionalized by water molecules. We find that the lowest energy solvent configuration at the surface involves a partial dissociation of adsorbed water molecules so that 50% of the Ti sites are H<sub>2</sub>O adsorbed while the rest are OH<sup>-</sup> adsorbed and the dissociated protons attach to nearby surface O sites. The top TiO<sub>2</sub> layer of all the slabs considered is modeled with this partially dissociated water configuration. Intact water molecules functionalize the bottom TiO<sub>2</sub> layer of the slabs which renders it inactive to hole doping relative to the top layer. The geometry of the bottom TiO<sub>2</sub> layer and adsorbed water is held fixed across all the hole-doped configurations considered. We model five different O-2p hole-radical configurations where the hole is localized either in the central bulk region of the slab or at the surface where it can form oxyl (Ti-O<sup>•</sup>) or bridge (Ti-O<sup>•</sup>-Ti) radicals. Among these, we find the bridge (Ti-O<sup>•</sup>-Ti) radical configuration with a O-2p<sub>y</sub> hole to be the lowest in energy separated by ~0.1 eV from the nearest oxyl (Ti-O<sup>•</sup>) radical configuration. Interestingly, the magnitude of the (Ti-O<sup>•</sup>-Ti) and (Ti-O<sup>•</sup>) energy difference is smaller but is opposite in sign to that predicted at the rutile TiO<sub>2</sub> surface where the geometry and water adsorption characteristics are different. Within the theoretical framework employed in this work, the configurational energies of the surface radicals can be calculated relative to the O-2p hole localized in the bulk region of the slab. By referencing this bulk-localized hole configuration to the self-trapped hole configuration in bulk SrTiO<sub>3</sub> from previous calculations by Janotti *et. al.*,<sup>96</sup> we assume a self-trapping energy of the bulk hole polaron to be ~0.05 eV. Relative energy differences between this bulk-localized configuration and oxyl or bridge surface-localized configurations calculated in the current work (Table 5.1) then indicate that the surface-localized configurations have self-trapping energies in the range of 0.19-0.43 eV.

	Valence band hole	Bulk	Oxyl1	Lateral1	Oxyl2	Lateral2
Relative Energy (eV)	0.0	-0.05*	-0.19	-0.31	-0.34	-0.43

**Table 5.1:** Relative energies of different localized hole configurations with respect to a delocalized valence band hole configuration. \* The bulk hole self-trapping energy is taken from Janotti *et. al.*<sup>96</sup>

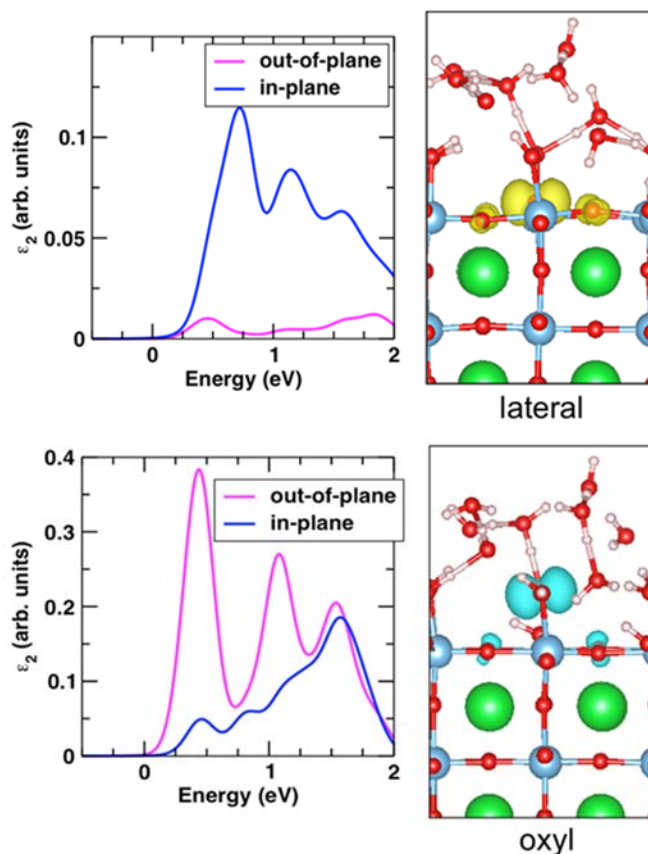


**Figure 5.18:** Polarization resolved optical dipole transition strengths from the mid-band gap O 2p hole state to conduction band orbitals for lateral (Ti-O•-Ti) and oxyl (Ti-O•) surface hole radicals at 25% surface hole coverage are shown along with corresponding spin-density iso-surfaces for the localized hole orbitals. As in the case if low 6.25% hole coverage, the lateral hole configuration is predominantly associated with in-plane polarized transitions while the oxyl radical exhibits mainly out-of-plane character.

Therefore, optically excited valence band hole carriers can transform into either bridge or oxyl radicals at the surface by transferring energy to vibrational degrees of freedom during the relaxation process. Density of states plots in Figure 5.18, indicate all radicals lead to localized mid gap hole states that are optically active with respect to emissive transitions from free-carrier like conduction-band states that are populated either by n-doping or photoexcitation. Accordingly, the contribution to the imaginary part of the dielectric matrix ( $\epsilon_2$ ) obtained by restricting the allowed transitions to those between the mid-gap hole states and the conduction band manifold was calculated which provides a qualitatively accurate description of the

nature of the emissive transitions probed in the experiment. The calculated diagonal components of  $\epsilon_2$  were separated into *in-plane* and *out-of-plane* components of light-polarization and are shown in Figure 5.17 for the two lowest energy configurations. Assessments of *in-plane* and *out-of-plane* character are independent of surface excitation (Figure 5.18). We find that optical transitions involving the bridge (Ti-O•-Ti) radical state and states near the conduction band minimum are principally *in-plane*-polarized (Figure 5.17 a) and this character of the optical transitions also extends up to 1 eV higher into the conduction band. Given that the exciton binding energy in SrTiO<sub>3</sub> is  $\sim 0.22$  eV,<sup>97</sup> we expect the *in-plane* polarization in the case of the bridge (Ti-O•-Ti) radical to be a feature that is robust with respect to the independent particle approximation employed for the calculation of the optical transitions. In contrast, optical transitions involving the oxyl (Ti-O•) radical state and low-lying conduction band states are largely of *out-of-plane*-polarized character and transitions from states  $\sim 0.75$  eV higher are of mixed character. Bulk-localized hole states on the other hand are not expected to produce a polarization-dependent signal as the *x*-, *y*- and *z*- directions are equivalent within the bulk of the material.

### 5.3.3 Radical Distribution & Surface-Limited Reaction Kinetics: Voltage dependence with 400 nm probe

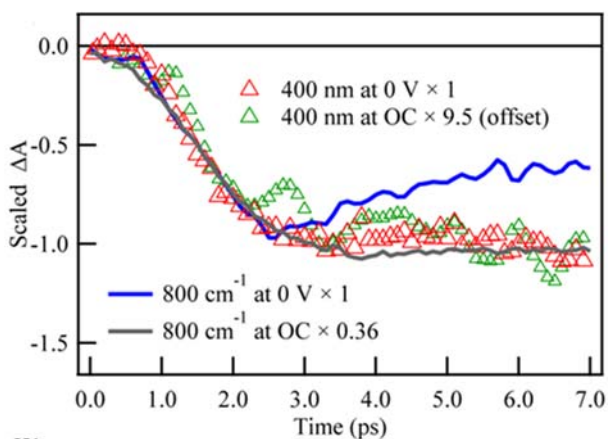


**Figure 5.19:** Mid-gap state (400 nm) at 0 V (red, open triangle) and open circuit (green, open triangle) compared to the oxyl's subsurface vibration ( $800\text{ cm}^{-1}$ ) at 0 V (blue, solid line) and at open circuit (grey, solid line). The scale factors of the open circuit traces are noted with respect to the 0 V traces. The 0 V traces (400 nm and  $800\text{ cm}^{-1}$ ) are normalized to each other.

We turn to further experiments with the 400 nm probe, but now under different applied voltages. The experiments described complete the picture of a single time constant of a surface-limited reaction producing a distribution of both bridge and oxyl radicals. First, we address a disparate voltage dependence of the bridge and oxyl radical populations. Figure 5.19 shows time traces of the maximum absorption change for the oxyl's subsurface vibration at open circuit and 0 V ( $800\text{ cm}^{-1}$ ), compared to that of the radicals' mid-gap state at open circuit and 0 V (400 nm). The infrared and optical data at 0 V are normalized to each other, while the open circuit data are denoted by a scale factor with respect to this normalization. For the 400 nm trace at open circuit, there is an additional offset due to the bulk carrier contribution. While the oxyl's population, measured by its specific vibration, is smaller at 0 V ( $\times 0.36$ ) than at open circuit, the radicals' population, measured by the mid-gap state, is much larger ( $\times 9.5$ ). Throughout, the 1.3 ps formation time constant is preserved. The disparate voltage dependence implies that, while oxyl and bridge radicals are both created and with the same time constant, the bridge radicals preferentially populate the surface at oxidative potentials. This is also suggested by the 80/20 ratio derived from the polarized transition optical dipole (Figure 5.16). For oxyl and bridge radicals to populate the O-sites indiscriminately, the anticipated ratio of bridge to oxyl radicals on the 100 surface of  $\text{SrTiO}_3$  would be 67/33.

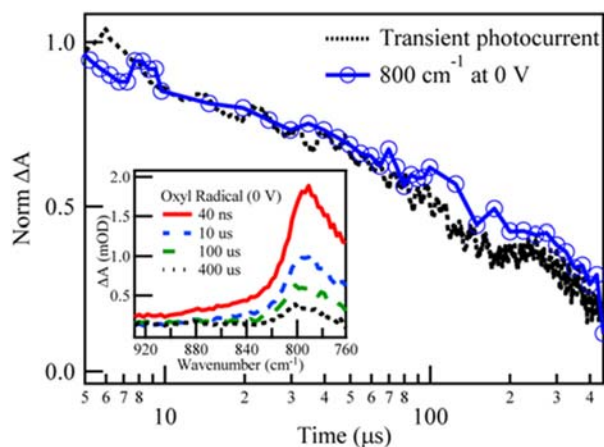


**Figure 5.20:** Time-resolved photo-current at 0 V (black, dashed line) compared to the decay of the oxyl's subsurface vibration ( $800\text{ cm}^{-1}$ ) at 0 V (blue line, open circle). The inset shows the spectrum of the sub-surface vibration at 40 ns (red, solid), 10  $\mu\text{s}$  (blue, dashed), 100  $\mu\text{s}$  (green, dashed) and 400  $\mu\text{s}$  (black, dashed).

To show that the surface thus populated is involved in bond formation, Figure 5.20 compares a spectroscopic probe of the surface to the time-resolved photocurrent. Here, the spectroscopic probe chosen is the oxyl's subsurface vibration, rather than the mid-gap state. Since the vibration is very specific to charge localized into a titanium oxyl, its decay in principle counts charge leaving the surface while avoiding dynamics associated with later intermediates of the cycle. Indeed, the decay of the oxyl's subsurface vibration parallels the decay of the photocurrent between 5-400  $\mu$ s. The fact that a single type of O-site radical decays with the same time constant as the overall charge leaving the surface implies that the initial radical distribution created by the 1.3 ps time constant and consisting of diverse O-site radicals (Figure 5.19) concertedly decays to form chemical bonds (Figure 5.20).

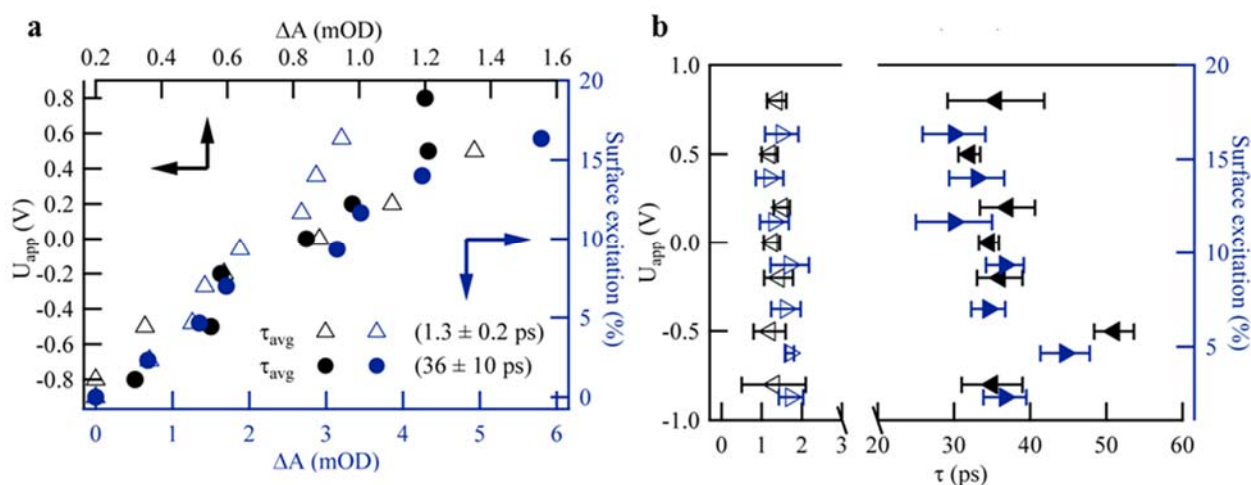


**Figure 5.21:** **a**, Amplitudes obtained for the two component fit of Figure 5.11 with applied voltage from -0.8 V to +0.8 V (left, top, black dots and open black triangles) and 0-20% surface excitation at 0 V (right, bottom, blue dots and open blue triangles). **b**, Time constants for the two component fit with applied voltage from -0.8 V to +0.8 V at 2.3 % surface excitation (left, black triangles) and at 0 V with 0-20% surface excitation (right, blue triangles). The reported time constants (1.3 ps, 36 ps) and their error (0.2 ps, 10 ps) come from an average of all the data points shown.

Finally, the voltage independence of the formation time constants demonstrates explicitly a single, surface-limited reaction of:  $[h^+] + [S] \rightarrow [R]$ , where  $[S]$ ,  $[R]$ , and  $[h^+]$  denote respectively the concentration of surface active sites, radicals, and valence band holes. As shown in Figure 5.21 a, the applied voltage and light excitation modulate the reactant  $[h^+]$  and product  $[R]$  concentrations. The light excitation is reported as a % surface excitation of all available surface O sites, where

all the photo-holes generate radicals. At higher oxidative potentials (greater than -0.8V), the radicals' absorption change increases (Figure 5.21 a) while the time constants (1.3 ps, 36 ps) are not altered (Figure 5.21 b). With increasing surface excitation at 0 V, the radicals' absorption change also increases (Figure 5.21 a, Figure 5.22 a) while the time constants are not altered (Figure 5.21 b, Figure 5.22 b). The fact that increasing the product concentration does not modify the time constants demonstrates a surface limited, zero-order reaction. Further, at open circuit, the radical concentration saturates with excitation (Figure 5.23) at ~4-5%.

While the reaction is surface limited, the product concentration increases with both oxidative potential and surface excitation. The surface excitation concomitantly increases the anodic current (Figure 5.23). Hence, both potential and current modify the surface active site concentration, [S]. Specifically, for surface sites associated with localized holes, the observed linear increase (Figure 5.21 a) with oxidative potential and anodic current is expected.

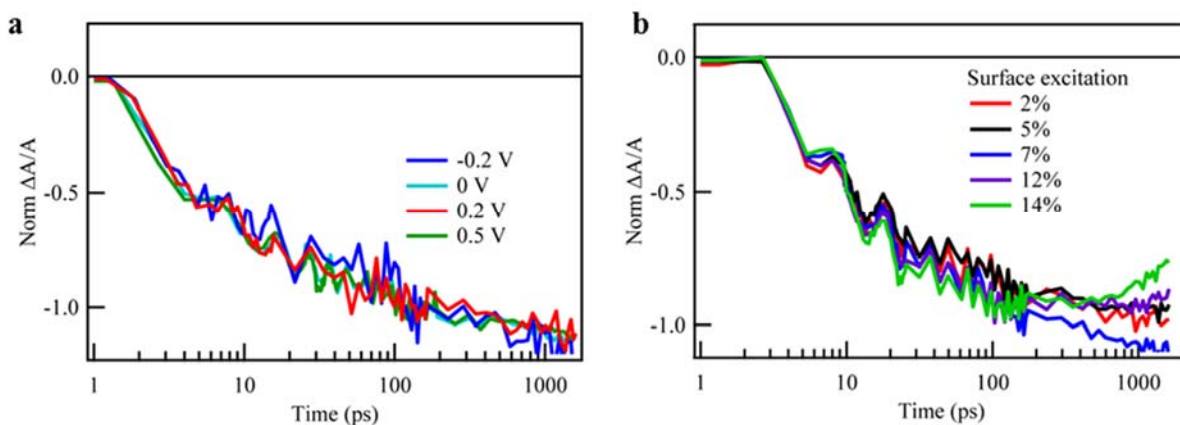


**Figure 5.22: a**, Normalized kinetics for the 0.1% Nb-doped SrTiO<sub>3</sub> at -0.2 V (blue), 0 V (cyan), 0.2 V (red) and 0.5 V (green) in 0.1 M NaOH. No measurable difference in time dynamics is observed between different applied potentials when normalized. **b**, Normalized kinetics for the 0.1% Nb-doped SrTiO<sub>3</sub> at 0 V in 0.1 M NaOH solution with 2% (red), 5% (black), 7% (blue), 12% (purple) and 14% (green) surface excitation. No measurable difference in time dynamics is observed between different surface excitation when normalized.

A rate model of the reaction  $[h^+] + [S] \rightarrow [R]$  summarizes the dynamics. The rate equations for [R] and [S] are  $\frac{d[R]}{dt} = k [h^+]^x [S]^y$  (1) and  $\frac{d[S]}{dt} = -k [h^+]^x [S]^y$  (2), where  $k$  is the equilibrium rate constant. A zero order, surface limited reaction is

given by  $x = 0$  and  $y = 1$ , which is also consistent with a one hole transfer reaction ( $x$  and  $y$  are both  $\leq 1$ ). Solving equations (1) and (2) leads to  $[R]_t = [S]_0(1 - e^{-kt})$ , where  $[S]_0$  is the concentration at which the surface saturates with radicals (tuned by the reaction conditions) and at the potentials investigated,  $k$  is constant. This reaction models the observed kinetics because the formation dynamics can indeed be fit with rising exponentials, the radical concentration increases with the available surface sites (e.g.,  $[S]_0$ ), and the rate constants are independent of potential. Finally, the 1.3 ps time constant derived from this rate model is especially preserved under a wide range of experimental conditions, with an average deviation of  $\pm 0.2$  ps (Figure 5.21 b).

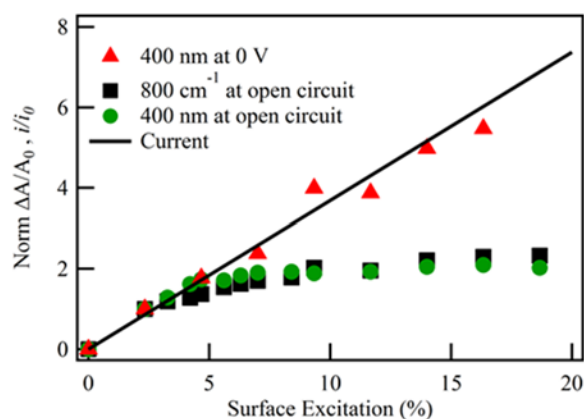


**Figure 5.23:** The absorption change at 1 ns and 400 nm (red, triangle) compared with the steady-state photocurrent (black, line), both measured at 0 V, with increasing surface excitation. The absorption change at 1 ns and 400 nm (green, circle) compared with the oxyl's absorption change at 1 ns and 800  $\text{cm}^{-1}$  (black, square), both measured at open circuit, with increasing surface excitation.  $\Delta A$  and  $i$  have been normalized to their respective value at a fluence of  $0.05 \text{ mJ cm}^{-2}$  (2.33% surface excitation). Note that under reaction condition, photo-induced stimulated emission is not saturating up to 20% surface excitation while at open circuit, photo-induced stimulated emission is saturating at 5% surface excitation.

### 5.3.4 Charge transfer kinetics of Radicals & VB holes: Decomposition of white light probe with applied voltage

In this section, we turn to experiments that finish the description of the full charge-transfer reaction required to create one-electron intermediates. Namely, the formation of the O-site radicals is observed to arise from the concomitant decay of

valence band holes. A broad-band white light probe of the n-SrTiO<sub>3</sub> surface with applied voltage, together with singular value decomposition (SVD), is employed. Figure 5.24 a and 5.24 b show, as a function of applied voltage, the first principal component of the kinetics and their associated spectra respectively. This analysis also defines the spectrum of the oxy and bridge radicals' optical emission.

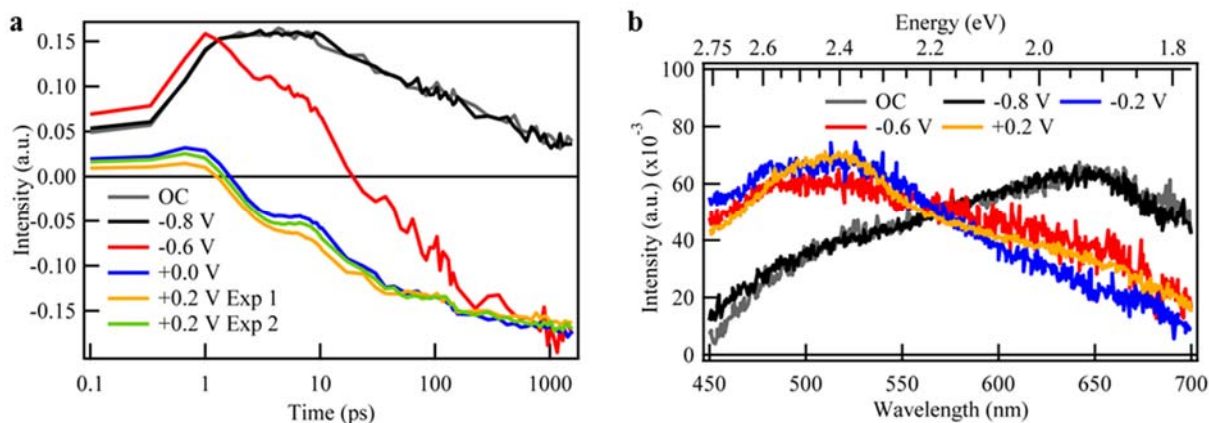


**Figure 5.24:** Broad-band white light probe of both radicals and valence band holes. From the singular value decomposition analysis, **a**, the eigenkinetics and **b**, eigenspectra of the first principal component at select voltages

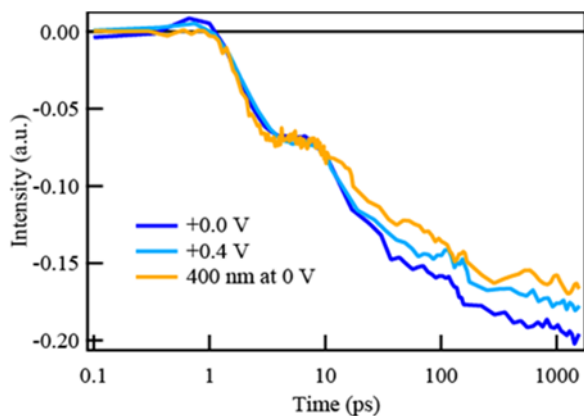


**Figure 5.25:** The eigenkinetics of the first principal component under voltage from the singular value decomposition analysis compared with kinetics at 400 nm at 0 V applied potential. Similar kinetics are observed for both probe.

At voltages greater than 0 V, the absorption change is almost entirely emissive and the dynamics, containing two formation times with a delay in-between, are identical

to the 400 nm probe (Figure 5.25). The spectrum of the radicals at 0 V and beyond peaks at 2.6 eV (475 nm), but is spectrally very broad (400-600 nm). The radicals' decomposed spectrum is identical to the photoluminescence spectrum from SrTiO<sub>3</sub> (Figure 5.26 a), which had previously been associated with various proposed mid-gap states.<sup>96,98</sup> The photoluminescence shown in Figure 5.26 is specifically from a sample dipped in pH 13 water, which significantly enhances the photoluminescence compared to air (Figure 5.26 b). Importantly, the measured, decomposed spectrum can differ between samples, shifting by  $\sim 0.2$  eV (Figure 5.26 a) while the formation dynamics are not altered (Figure 5.24 a). This suggests that diverse radical species encompassed by the emission form in ratios sensitively subject to reaction conditions. Furthermore, through the SVD analysis, we can assign the 1.3 ps, 4.5 ps, and 36 ps formation dynamics to the entire emission spectrum.

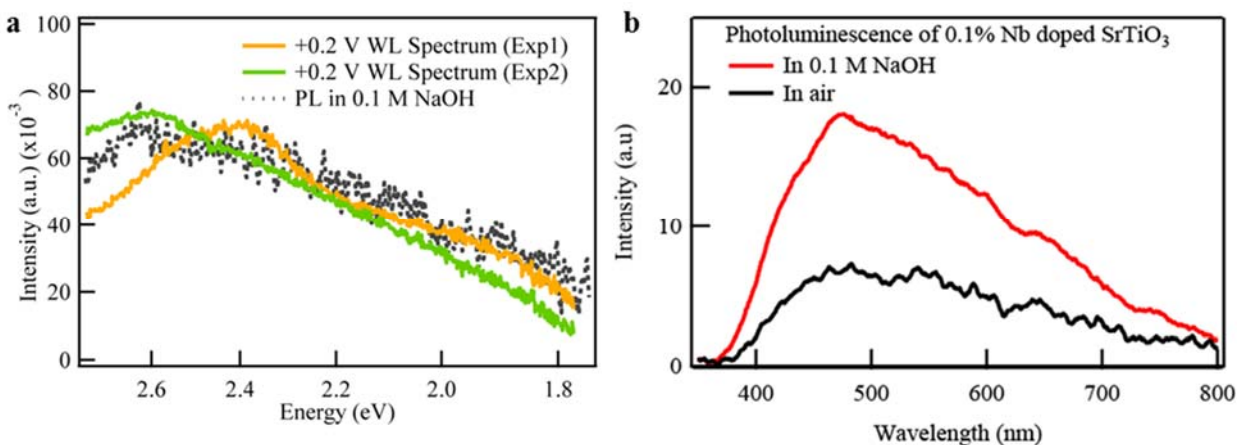


**Figure 5.26:** **a**, From the singular value decomposition analysis, eigenspectra at +0.2 V (two trials, Exp1 and Exp2) compared to photoluminescence spectra of 0.1% Nb doped SrTiO<sub>3</sub> in 0.1 M NaOH. **b**, Photoluminescence spectrum of 0.1% Nb doped SrTiO<sub>3</sub> in 0.1 M NaOH (red) compared to in air (black). The photoluminescence intensity increases in electrolyte solution.

At more reductive potentials, there is an additional, positive absorption change with its own kinetic component. At open circuit or equivalently, -0.8 V, the absorption change is entirely positive and displays a  $\sim 150$  ps exponential decay. The transient spectrum associated with the positive absorption change at -0.8 V peaks at 1.9 eV (650 nm). Unlike the radicals' absorption change that saturates with surface excitation at open circuit (Figure 5.23), this redshifted absorption change only increases with fluence (Figure 5.27 a and Figure 5.27 b). Further, it is not affected by methanol or pH (Figure 5.27 c and Figure 5.27 d). Taken together, the significant redshift of the spectrum, the lack of a surface saturation, and no spectral or kinetic

change with different electrolytes, the spectral component isolated at -0.8 V is naturally assigned to bulk holes in the valence band. The overlap of this transient spectrum with that of the radicals' spectrum explains why only at shorter wavelengths, near 400 nm, are the formation dynamics of the radicals isolated across a broad voltage range, including at open circuit. It also explains the bulk hole component observed at open circuit with a 400 nm probe and used to identify time zero.

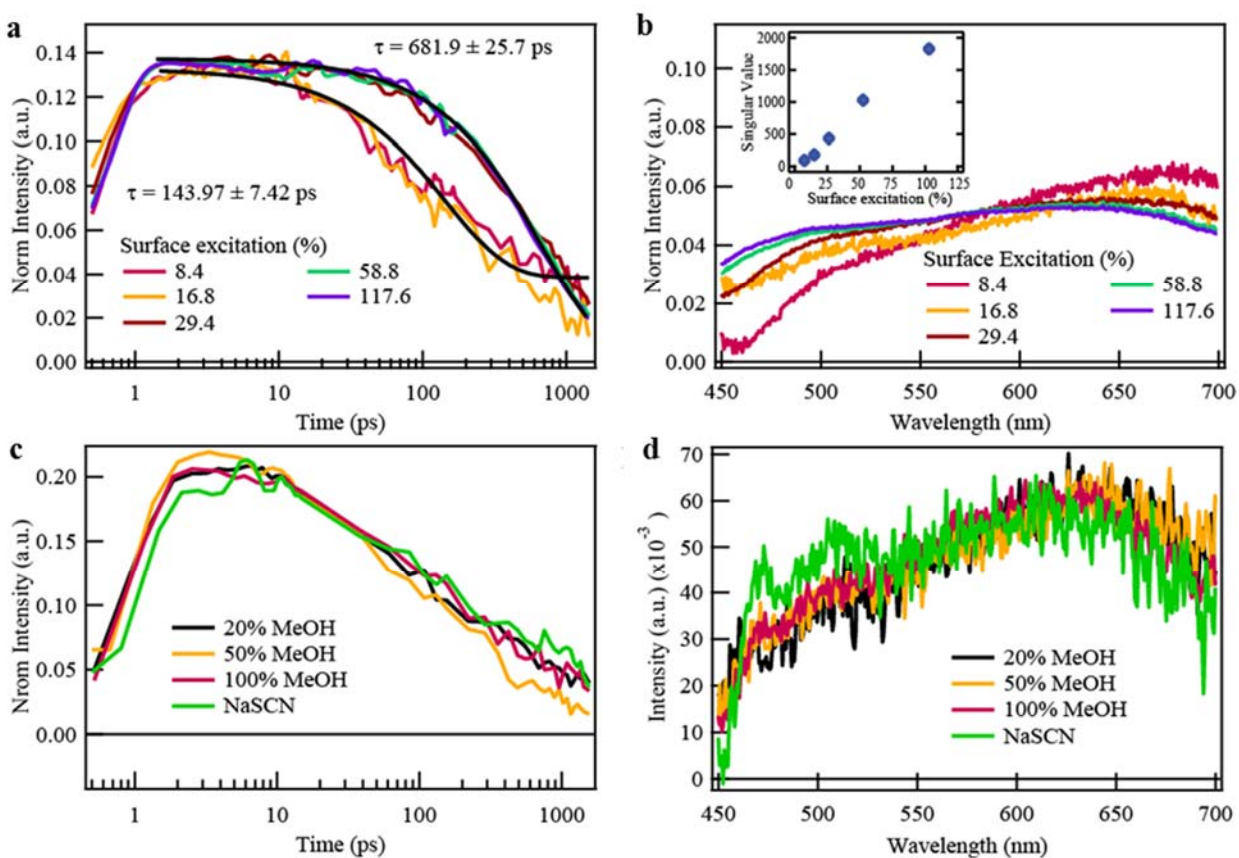


**Figure 5.27:** The kinetics and spectra shown here are from a singular value decomposition analysis of the white light probe. **a**, Kinetics for spectra component peaks at 650 nm at open circuit for 0.1% Nb-doped SrTiO<sub>3</sub> at 8.4% (pink), 16.8% (yellow), 29.4% (red), 58.8% (green) and 117.6% (purple) surface excitation. **b**, The corresponding spectrum for **a**. The inset of **b** shows this component has a singular value that increases with increasing surface excitation. **c**, Kinetics for spectra component peaks at 650 nm at open circuit for 0.1% Nb-doped SrTiO<sub>3</sub> in different methanol concentration and NaSCN. **d**, The corresponding spectrum for **c**. No change is observed with varying methanol concentration or NaSCN.

Clearly, the potential-dependent white light spectra identify the dynamics of two distinctly different species: at oxidative potentials, the formation of oxyl and bridge radicals, and at reductive potentials, the decay of valence band holes. Similar to that observed with a 400 nm probe, the radical population increases linearly with oxidative potential (Figure 5.28). Since the formation time constants are not altered by the potential, but the radicals' population increases, the valence band hole decay should be potential-dependent: in order to fill more surface sites with radicals within the same time frame, the hole population has to deplete faster. Such a potential dependence was observed previously<sup>84</sup> and a detailed model that includes the potential dependent decay of holes  $k(V)$  and the potential independent formation dynamics of the radicals will be considered in a separate publication. We note that the potential dependence should result from a change in the free energy difference across the interface. Indeed, the applied voltage can drop across the screening, Helmholtz layer at the interface and move the valence band down in energy,<sup>23,25,29,30,84</sup> lowering the potential of the valence band holes.

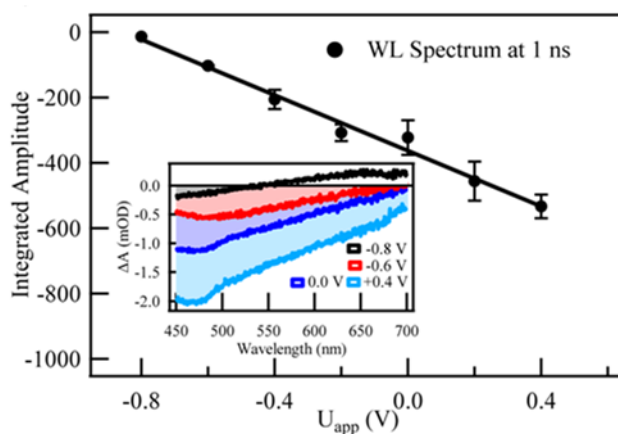


**Figure 5.28:** Integrated amplitude of the emission at 1 ns after pump excitation for -0.8 V to +0.4 V. Error bars represent the standard deviation between two measurements at each voltage. The inset shows the raw, noise-reduced traces at 1 ns at select voltages.

## 5.4 Discussion

In this section, we focused on assigning the 1.3 ps formation time constant of the mid-gap state to particular one-electron intermediates of photo-catalytic water oxidation at the n-SrTiO<sub>3</sub>/aqueous interface. The 1.3 ps time constant, along with the 4.5 ps delay, are separately attributed to titanium oxyl and bridge radicals by: (1) An

identical population time for oxyl radicals, as measured by its subsurface vibration at  $800\text{ cm}^{-1}$ . (2) A predominantly *in-plane* optical dipole moment ascribed specifically to bridge radicals (Ti-O•-Ti).

The fact that the two limiting structures of single O-site radicals—oxyl(*out-of-plane*) and bridge(*in-plane*)—simultaneously populate the surface is given by: (1) A detailed polarization dependence that shows the measured dipole moment to include an *out-of-plane* component (2) A disparate potential dependence of the bridge (via the mid-gap state) and oxyl (via the subsurface vibration) populations, while the time constants (1.3 ps, 4.5 ps) are potential independent (3) A broad emission assigned to the same time constants (1.3 ps, 4.5 ps), which can shift depending on the radical distribution ( $\sim 0.2\text{ eV}$ ).

We now turn to the physical process that defines the 1.3 ps and 4.5 ps time constants. Most generally, localizing a valence band hole to a water adsorbed surface site involves hole transport across the depletion region of the semiconductor, molecularly specific surface events such PCET, and the solvation dynamics of water. However, since the time constants are surface-limited, they should be independent of the hole location within the depletion region. Further, applied voltages, which significantly modify the electric field across the depletion region (from  $7 \times 10^5\text{ V/cm}$  at  $-0.6\text{ V}$  to  $1.4 \times 10^6\text{ V/cm}$  at  $0\text{ V}$ ), do not alter the time constants.

The fact that the time constants are exclusively associated with the reactive, aqueous interface, not altered by potential and surface excitation, and describe populating the surface with two limiting structures of O-site radicals (*in-plane* and *out-of-plane*), suggests that they are not controlled by PCET, but are rather defined by the solvation dynamics of water. We first discuss the 1.3 ps time constant in this context. Importantly, a similar time constant appears in mid-infrared pump-probe spectroscopy of bulk and interfacial water, where the hydroxyl stretch vibration (0-1) is excited and its relaxation probed over a broad frequency range. The hydroxyl stretch transfers its energy to lower energy excitations of neighboring water molecules, which include bending and librational modes, as well as the collective H-bond network.<sup>87-89,99-103</sup> In most studies, HOD within either H<sub>2</sub>O or D<sub>2</sub>O probes the relevant dynamics. The time constant reported spans between 0.7-1 ps for OH within D<sub>2</sub>O<sup>89,100,102</sup> and 1.4-1.8 ps for OD within H<sub>2</sub>O.<sup>66,89,99,100,103</sup> Though more challenging to determine, a faster relaxation time of 200-300 fs was suggested for OH stretches within bulk H<sub>2</sub>O.<sup>87,104</sup> At interfaces, sum frequency generation investigates adsorbed OH: a time constant of 1.3 ps is found at a hydrophobic silica surface<sup>87</sup> and a probe frequency-dependent time constant of 0.5-1.3 ps is found at the hydrophilic silica surface.<sup>105</sup> A 1.3 ps time constant is also found for hydroxyl stretch relaxation of water molecules surrounded by acetone in CCl<sub>4</sub>.<sup>88</sup>

The longer ( $> 1$  ps) time constant observed for radical formation suggests the relevance of a dilute H-bond network. In the systems quoted above, the ones that represent a dilute H-bond network with a 1-1.8 ps time constant are: (1) Isotopically dilute water networks (e.g. HOD in  $\text{H}_2\text{O}$ )<sup>89,100</sup> (2) A H-bond network for mixed water: acetone:  $\text{CCl}_4$  where it is suggested that one hydrogen interacts with acetone at a time<sup>88</sup> and (3) Adsorbed OH at a hydrophilic (0.5-1.3 ps)<sup>105</sup> and hydrophobic (1.3 ps) surfaces.<sup>87</sup>

The lack of an effect of deuteration on the kinetics supports a dilute H-bond network limit. As observed for the vibrational relaxation of the hydroxyl stretch in water: acetone:  $\text{CCl}_4$  mixtures, the radicals' formation time lacks an H/D exchange (Figure 5.29). Further, the coupling constant defining the Fano resonance between the oxyl's subsurface vibration and librations is not sensitive to deuteration, despite deuteration significantly modifying the density of librations near the vibration. This is reflected in the relatively constant width of the Fano resonance ( $30$  - $45$   $\text{cm}^{-1}$  or  $3$ - $4$  meV).<sup>85</sup>

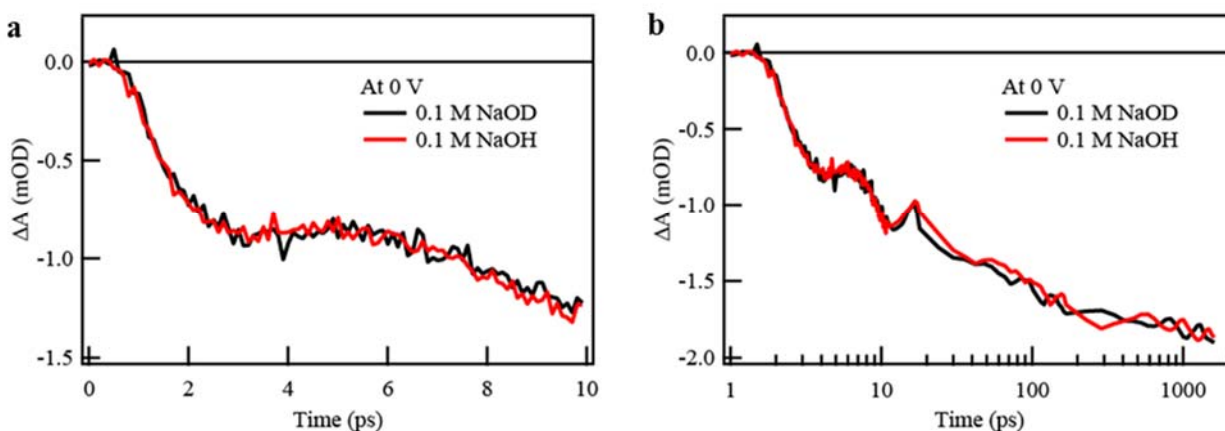


**Figure 5.29:** Kinetics for the 0.1% Nb-doped  $\text{SrTiO}_3$  at 0 V in 0.1M NaOH (red) compared with in 0.1M NaOD (black) from **a**, 0 to 10 ps **b**, 0 to 1.6 ns. No difference in time dynamics is observed between H and D.

By connecting the vibrational dynamics of the hydroxyl stretch to the formation of surface radicals, a kinetic mechanism emerges to describe how a delocalized valence band hole generates an O-site radical. As noted earlier in the theory section, the surface-localized radicals are characterized by energies  $\sim 0.19$ - $0.43$  eV lower than a valence band hole. Therefore, as the initially photo-excited VBM holes relax firstly into sub-surface hole-polarons and subsequently into surface-localized bridge or oxyl radicals, they are expected to transfer the excess energy into the nearby solvent

vibrational degrees of freedom. In particular, it emerges clearly from the theoretical modeling that assuming a 50% admixture of adsorbed  $\text{H}_2\text{O}$  and  $\text{OH}^-$  species, creating any of the stable surface-localized radical configurations requires the breaking of one OH bond. The non-adiabatic transfer of some of the VBM hole excess energy into a hydroxyl stretch could facilitate this process by reorganizing water molecules near the host O-2p hole site. We further note that starting from a sub-surface localized hole, the non-adiabatic relaxation process into bridge and oxyl radicals could proceed via similar transition states involving a stretched O--H--O configuration wherein an oxygen site in the top  $\text{TiO}_2$  layer exchanges a proton with a Ti adsorbed oxygen with the direction of the exchange determining the final product. Alternatively, a Ti adsorbed  $\text{H}_2\text{O}$  and Ti adsorbed  $\text{OH}^-$  group could exchange a proton to facilitate the stabilization of a surface radical. Such a mechanism is schematically diagrammed in Figure 5.30: The photo-hole in the solid-state band loses some of its energy to excite a hydroxyl stretch either as a 0-1 vibration in nearby water or on a surface-adsorbed species. As the hydroxyl stretch evolves and transfers energy to neighboring water molecules, the solvation environment engenders the transition state needed for radical formation. The solvation environment created by such a high energy, non-adiabatic mechanism is expected to yield diverse oxygen radicals likely through similar transition states that are not unique to a particular molecular structure, e.g. bridge or oxyl. Assuming the initial descent towards the transition state is rapid compared to the dynamics associated with the hydroxyl stretch relaxation, the latter, with a 1.3 ps time constant would be the rate-determining factor for all radicals. We note that molecular dynamics simulations<sup>106</sup> that start on the ground state potential energy surface and depend on thermal fluctuations to access the transition states do not describe this mechanism. More extensively, non-adiabatic molecular dynamics simulations<sup>107</sup> will be necessary to model the dynamics of the relaxation process that converts VBM delocalized holes into surface-localized radicals.

The thermodynamics required for this kinetic mechanism matches that expected. While the exact energetic position of the oxyl and bridge radicals within the gap may not be known yet precisely, theory suggests they are approximately  $\sim 0.4$  eV away from the valence band. Further, a  $\sim 0.3$ - $0.4$  eV potential energy difference to the  $\text{O}_2/\text{H}_2\text{O}$  Nernstian potential is common for photo-catalytic water oxidation on a number of transition metal oxides, as evidenced by catalysis initiated using the  $\text{Ru}(\text{bpy})_3$  dye.<sup>108</sup> Such a potential energy difference is the minimum necessary to excite the hydroxyl stretch vibration.

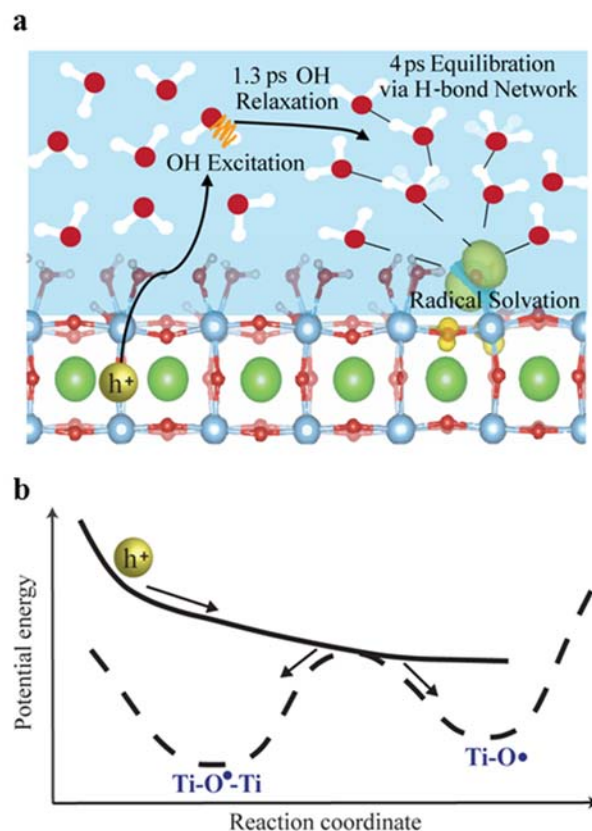


**Figure 5.30:** Diagram of non-adiabatic kinetic mechanism **a**, By exciting a hydroxyl stretch vibration that transfers energy to neighboring water molecules, a photo-hole engenders the solvation environment necessary for radical formation. The 1.3 ps vibrational relaxation is followed by a  $\sim 4$  ps period of H-bond equilibration. **b**, Proposed reaction diagram of forming oxyl ( $Ti-O\bullet$ ) and bridge ( $Ti-O\bullet-Ti$ ) radicals from energetic valence band holes.

We now turn to the concomitant nature of the 1.3 ps and 4.5 ps time constants observed. Following the relaxation of the hydroxyl stretch inter-molecularly, water forms an elevated temperature equilibrium. A number of studies<sup>87,99,104</sup> find that the equilibration occurs after the hydroxyl stretch relaxes and primarily by the breaking of H-bonds. For the dilute H-bond network of the OD stretch in  $H_2O$ , the time scale to reach the elevated temperature equilibrium is 4 ps.<sup>99,100</sup> This  $\sim 4$  ps time scale is seen to follow the 1.3 ps time constant for both the mid-gap state and the oxyl's subsurface vibration. In the latter, it appears as a 2-6 ps interval during which the Fano resonance evolves. Intriguingly, this suggests—through the vibration's coupling to librations—that we have a direct probe of the H-bond breaking events involved in

the equilibration process. Future work will investigate the vibrational and librational dynamics of water that respond to the generation of oxyl and bridge radicals, through both the evolution of the Fano resonance and a direct mid-infrared probe of the water molecules.

All of these dynamics concern the conversion of a hole into a radical that localizes the positive charge. However, in order to form the radical, this hole had to separate from the initially excited valence band population. Using the broad-band white light probe and SVD analysis, we were able to separately identify the formation dynamics of radicals and the decay of the valence band hole population. We demonstrated that reaction conditions, tuned by potential and surface excitation, modify the number of surface active sites. Future studies will explore this connection between the number of active sites, reaction conditions, and the solvation dynamics of water that stabilize the radicals.

## 5.5 Conclusion

We have identified the time constant (1.3 ps) by which oxyl ( $\text{Ti-O}\bullet$ ) and bridge ( $\text{Ti-O}\bullet\text{-Ti}$ ) radicals arise from valence band holes at the n-SrTiO<sub>3</sub>/aqueous interface during photo-catalytic water oxidation. The fact that the time constant is exclusively associated with the reactive, aqueous interface, is not altered by potential and surface excitation, and describes populating the surface with two limiting structures of O-site radicals (in-plane and out-of-plane), led to a proposed, non-adiabatic mechanism for forming stable one-electron reaction intermediates based on their solvation at aqueous interfaces.

## Chapter 6

# The dynamics of transforming initial water oxidation intermediates at n-SrTiO<sub>3</sub>/aqueous interface

### 6.1 Introduction

At solid-liquid interface, chemical bonds formation proceeds after the ultrafast formation of initial photogenerated intermediates. For the case of multi-step water oxidation on metal oxide photocatalyst, the first chemical bond formed after initial radicals are thought to be the O-O bond.<sup>13,109</sup> Many studies have suggested the existence of the O-O bond. Time-resolved infrared measurement has shown the existence of Co-O-O-H for reactions happened on photocatalyst Co<sub>3</sub>O<sub>4</sub>.<sup>9</sup> Steady state infrared measurement has shown Ti-O-O-H served as a very important intermediate for water splitting on anatase and rutile photocatalytic TiO<sub>2</sub>.<sup>17,55</sup> Ir-O-O-H is also shown as a critical intermediate for water oxidation on IrO<sub>2</sub> photocatalyst.<sup>110</sup> It is important to identify the formation dynamics of first chemical bond as it provides information towards understanding the whole water oxidation cycle. Also, the formation time of O-O bond can be much longer than the time range of ultrafast spectroscopy (fs-ps). Such that an ns to μs setup needs to be constructed to tracked the dynamics of O-O bond formation.

At n-SrTiO<sub>3</sub>/aqueous interface, as shown previously,<sup>10</sup> formation of initial intermediates of water oxidation will induce a mid-gap electronic state. Such a mid-gap state has induced a sub-bandgap optical signal with 400 nm and white light continuum. Such that tracking the mid-gap state signal with sub-bandgap optical spectroscopy provides dynamically information about the transformation of initial formed radicals.

Here, transient optical spectroscopy of efficient, photo-catalytic water oxidation at the single crystal n-SrTiO<sub>3</sub>/aqueous interface, probed by 400 nm and white light in reflectance, isolates the reaction dynamics of distinct water oxidation radicals. The distinct decay dynamics define two pathways to form potentially the O-O bond:

one occurring with an 8  $\mu\text{s}$  time constant, and another occurring with a 60  $\mu\text{s}$  time constant. The faster pathway (8  $\mu\text{s}$ ) is shown to be highly dependent on solution ionic strength, suggesting potential dependence of surface diffusivity. The slower pathway (60  $\mu\text{s}$ ) shows a distinctive kinetic isotope effect. With the use of  $\text{D}_2\text{O}$ , the time constant of reaction increased by a factor of  $\sim 1.8$ .

## 6.2 Experimental setup

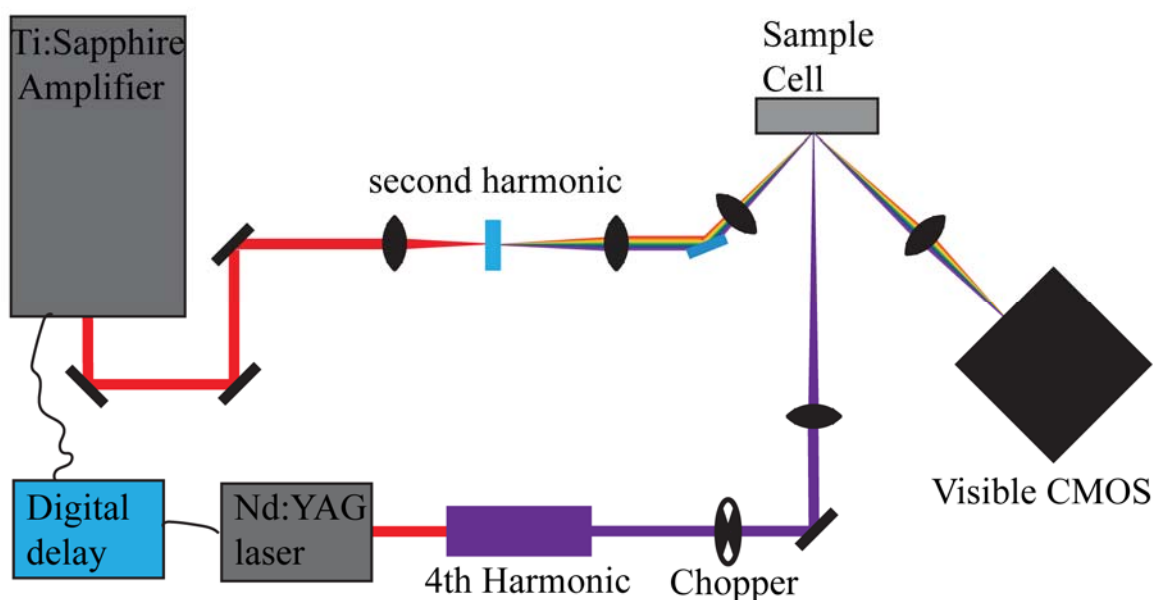


**Figure 6.1:** Representation of ns- $\mu\text{s}$  optical laser setup.

The ns- $\mu\text{s}$  optical laser setup is depicted in figure 6.1. The same sample cell is used from ultrafast measurement. For the transient experiments, the probe beam was derived from a regeneratively amplified Ti: sapphire laser system (Coherent Legend; Coherent, Inc., Santa Clara, CA) producing pulses with a center wavelength of 800 nm and  $\approx 150$  fs temporal width at a 1 kHz repetition rate. Then the 800 nm beam was frequency doubled to generate 400 nm light as probe. The pump beam was derived from a Nd:YAG laser system producing pulses with a center wavelength of 1064 nm and  $\approx 28$  ns temporal width at a 1 kHz repetition rate. Then it was directed to a fourth harmonic generation setup to generate 266 nm light as pump. Pump was incident normal to the sample surface. After the sample, the reflected probe beam was focused into an optical fiber, which was coupled to a CMOS array spectrometer (CAM-VIS-3; Ultrafast Systems, LLC, Sara-sota, FL). In all experiments, the pump

beam was modulated by a mechanical chopper (3501; Newport, Inc., Irvine, CA) at a frequency of 500 Hz. The detector output was interfaced with a personal computer, which provided automated control over an electronic delay generator (DG645; Stanford Research System, Inc., Sunnyvale, CA).

### 6.3 Results

At the perovskite n-SrTiO<sub>3</sub> (100)/aqueous interface, the water oxidation reaction is initiated by exciting above the band gap (3.25 eV) with a 266 nm (4.66 eV) laser pulse. With this deep UV pulse, a near ideal photon-to-current conversion efficiency (> 80%) is achieved. Therefore, photo-holes generated in the O 2p valence band efficiently migrate to the surface. Initially, surface holes localize on O-site to form radicals such as Ti-O• and Ti-O•-Ti, then the formed radicals transform into critical reaction intermediates such as Ti-O-O-Ti or Ti-O-O-H and final products O<sub>2</sub>. The graphical representation of this process is shown in Figure 6.2.

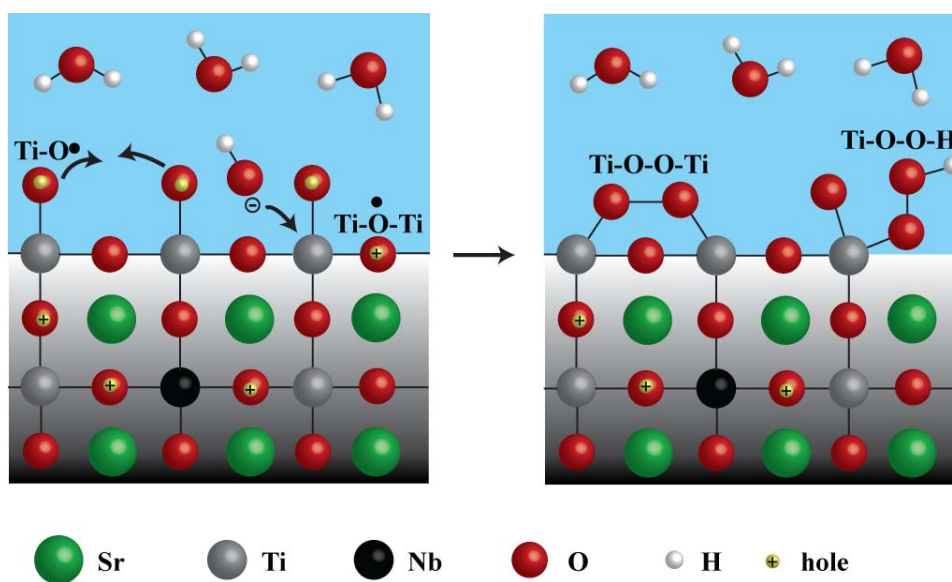


**Figure 6.2:** Representation of n-SrTiO<sub>3</sub> photo-electrode after bandgap (266 nm) photoexcitation. Photo-holes initially create O-site radicals: the titanium oxyl (Ti-O•) and the bridge (Ti-O•-Ti) radicals. These radicals subsequently react and form critical intermediates in the form of Ti-O-O-Ti and Ti-O-O-H.

### 6.3.1 Transformation of Oxyl & Bridge Radicals

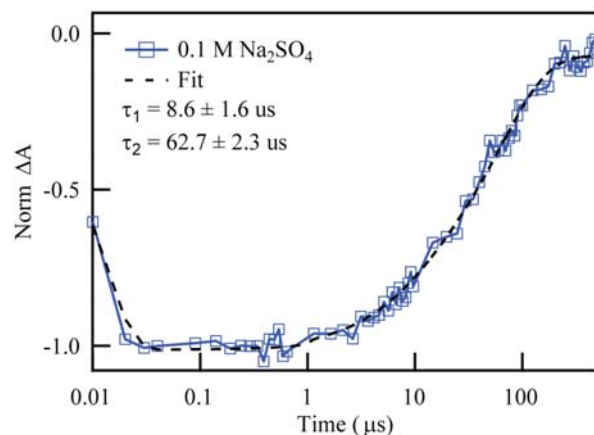


**Figure 6.3:** Transient kinetics (cyan, square) and fits (black) with a 400 nm at 0 V in 0.1 M Na<sub>2</sub>SO<sub>4</sub> solution. The total signal could be fitted with an exponential rise of 6 ns and two exponential decay of 8.6 μs and 62.7 μs

Figure 6.3 shows the kinetic trace of the 400 nm probe at 0 V in pH = 7 0.1 M Na<sub>2</sub>SO<sub>4</sub> solution. 400 nm is shown to probe initial water oxidation intermediates such as Ti-O• and Ti-O•-Ti.<sup>10</sup> Negative transient absorption occurs and it is a feature of photo generated holes localized at aqueous interface. The full kinetic traces can be fitted with one rising exponentials and two decaying exponential functions. The exponential rise has a time constant of 6 ns and it corresponds to radicals' formation time. Previous study suggests Ti-O• and Ti-O•-Ti can be formed within 100 ps,<sup>10</sup> the observed 6 ns time constant here is the result of instrument resolution time of 28 ns.

The two-exponential decay have the form  $\Delta A = A_1 e^{\frac{-t}{\tau_1}} + A_2 e^{\frac{-t}{\tau_2}}$ . Two time constants of 8.6 μs (τ<sub>1</sub>, fast) and 62.7 μs (τ<sub>2</sub>, slow) can be extracted which correspond to initial formed radicals transforming into other types of intermediates that do not have an optical transition at 400 nm, potentially molecular moiety like Ti-O-O-Ti and Ti-O-O-H. It is quite interesting to observe the transformation of initial Ti-O• and Ti-O•-Ti takes place in the microsecond range as they form very fast in the ps time scale. This suggests the initial water oxidation intermediates have to be stabilized at metal oxide/aqueous interface for a prolonged period of time before the next reaction step takes place. Two distinctive decay time constants indicate potential two separate reaction pathways are involved. For now, it is labelled as fast τ<sub>1</sub> and slow τ<sub>2</sub> kinetics.

### 6.3.2 Ionic strength influence on the transformation dynamics

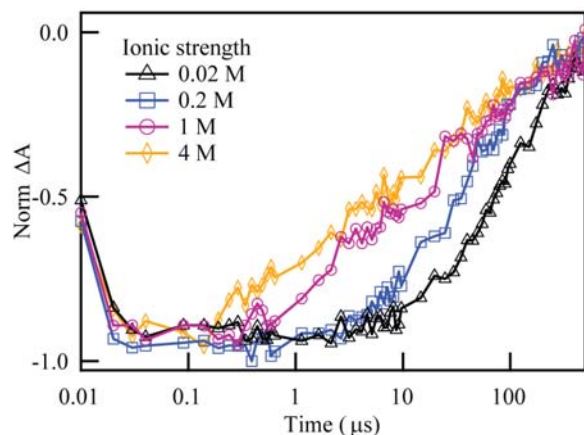


**Figure 6.4:** Normalized kinetics of the transient response at 0 V with a 400 nm probe in 0.02 M (black, triangle), 0.2 M (cyan, square), 1 M (Magenta, circle) and 4 M (orange, rhombus)  $\text{Na}^+$  solution,  $\text{pH} = 7$ .

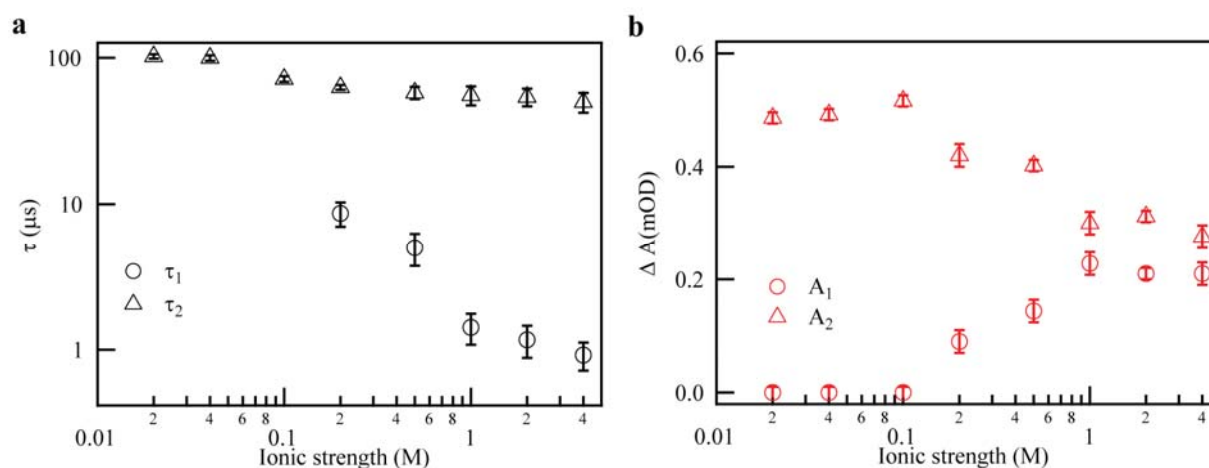


**Figure 6.5:** **a**, Transformation rate constants and **b**, Amplitudes for the two-component fit with ionic strength from 0.02 M to 4 M at 0 V applied potential. With higher ionic strength, transformation rate constant decreases. Both rate constant and amplitude saturates near 1 M ionic strength.

Figure 6.4 shows the kinetics of transforming initial water oxidation intermediates with 0.02 M to 4 M ionic strength counting  $\text{Na}^+$  ions, i.e. 0.01 M to 2 M  $\text{Na}_2\text{SO}_4$ .  $\text{Na}_2\text{SO}_4$  is known to not be oxidized by n-SrTiO<sub>3</sub> in current reaction condition as the

$\text{SO}_4^{2-}$  are in the highest oxidation state. With higher ionic strength in the solution, faster reaction rate observed for  $\text{Ti-O}\cdot$  and  $\text{Ti-O}\cdot\text{-Ti}$ . Following the same fitting procedure in Figure 6.3, two decay components for every ionic strength are obtained and plotted in Figure 6.5. Both rate constant decrease with increasing ionic strength and saturate near 1 M. And at low ionic strength  $< 0.1\text{M}$ ,  $\tau_1$ , the fast component of the decay vanishes and it recovers at 0.2 M ionic strength. Also, the amplitude  $A_1$  associated with fast  $\tau_1$  kinetics increases with ionic strength and saturates near 1M. The opposite trend is observed for  $A_2$  which is associated with slow  $\tau_2$  kinetics. The amplitude for two components with each ionic strength is plotted in Figure 6.5 b.

### 6.3.3 pH dependence

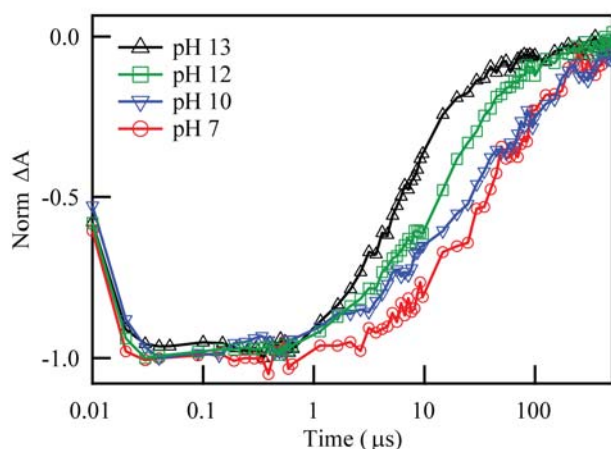


**Figure 6.6:** Normalized kinetics of the transient response at 0 V with a 400 nm probe in pH 13 (black, triangle), 12 (orange, square), 10 (cyan, upside-down triangle) and 7 (Magenta, circle) solution.

Solution pH can also affect the rate of  $\text{Ti-O}\cdot$  and  $\text{Ti-O}\cdot\text{-Ti}$  transformation. To study the pH effect on transformation rate, equal ionic strength solution is prepared at 0.2 M with varying pH. Figure 6.6 shows the normalized kinetic traces of the 400 nm probe at 0 V in different pH solution with 0.2 M ionic strength counting  $\text{Na}^+$  ions. The graph seems to indicate a faster transformation with higher solution pH. However, following the same fitting procedure in Figure 6.6, two decay components for every ionic strength are obtained and plotted in Figure 6.7. With the same ionic strength, changes in pH do not affect both kinetic rate constant  $\tau_1$  and  $\tau_2$  from pH 7 -13. Changes mainly comes from amplitude. With increasing pH, there is an increase

for fast  $A_1$  component. At  $\text{pH} > 13$ , transformation rate constant is changed and the reaction becomes faster with increasing  $\text{pH}$ .

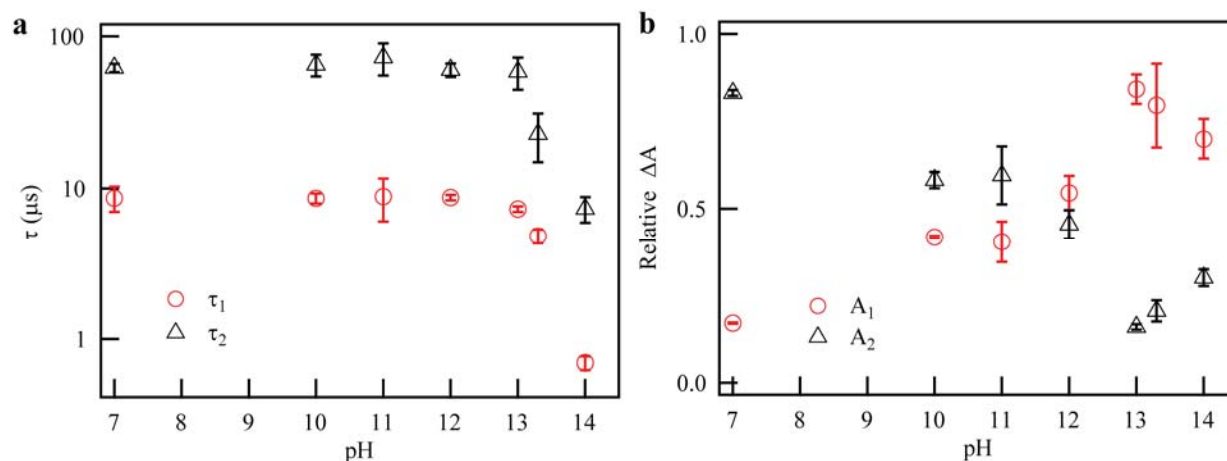


**Figure 6.7:** **a**, Transformation rate constants and **b**, Amplitudes for the two-component fit with different  $\text{pH}$ .

### 6.3.4 Kinetic isotope effect

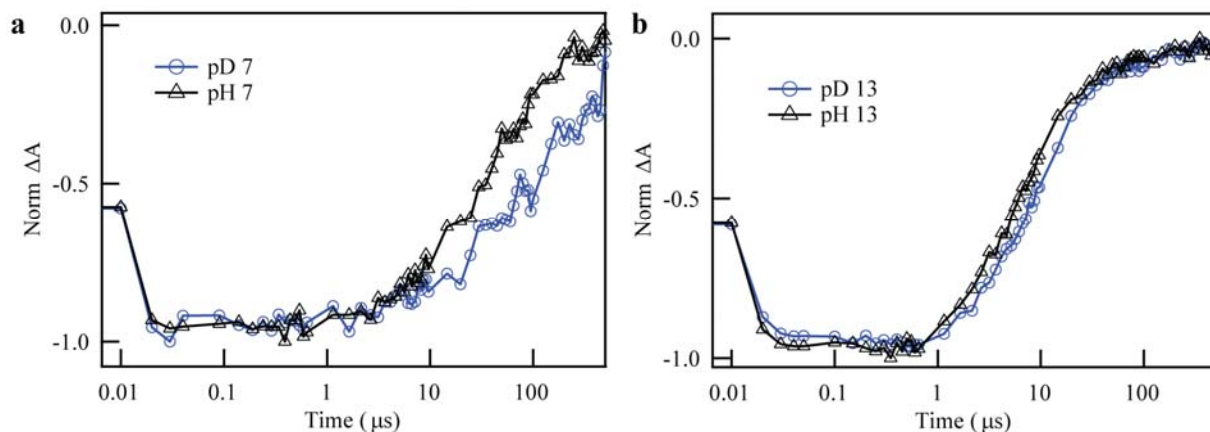


**Figure 6.8:** Normalized kinetics of the transient response at 0 V with a 400 nm probe in **a**, pD 7 (cyan, circle) and pH 7 (black, triangle), **b**, pD 13 (cyan, circle) and pH 13 (black, triangle) solution.

To further study the mechanism of full catalytic cycle, isotope exchange experiments are performed at various  $\text{pH}$ 's with 0.2 M ionic strength except  $\text{pH} > 13.3$ . Figure 6.8 shows the normalized kinetic traces of the 400 nm probe at 0 V in

pH/D 7 and 13 solutions. And figure 6.9 shows the difference in kinetics between H<sub>2</sub>O and D<sub>2</sub>O.

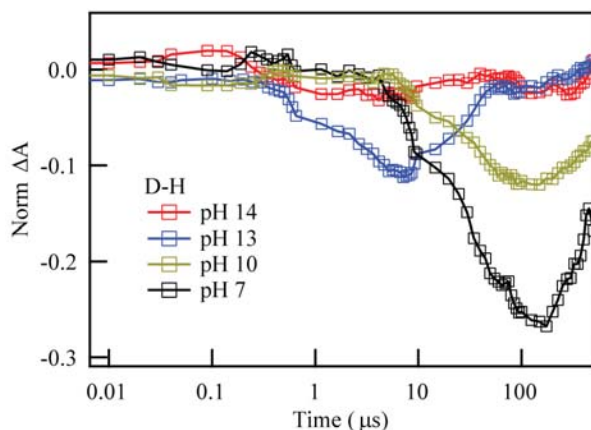


**Figure 6.9:** The difference in transient kinetics between D and H at pH 14 (red), pH 13 (cyan), pH 10 (yellow) and pH 7 (black). It is observed that with decreasing solution pH, the difference in kinetics shifts its peak position from very short time  $< 0.1 \mu\text{s}$  to long time  $> 100 \mu\text{s}$ . At pH 14, there is no significant difference present. At pH 13, the difference in kinetics is centered at 8  $\mu\text{s}$ . At pH 10, the difference is centered at 100  $\mu\text{s}$ . At pH 7, the difference is centered at 120  $\mu\text{s}$ .

At pH = 14, isotope exchange nearly has no effect on the transient kinetics. Reaction rate stays the same for both H<sub>2</sub>O and D<sub>2</sub>O. However, at pH  $< 13$ , isotope exchange shows a difference with longer reaction time in D<sub>2</sub>O solution. Following two exponential fitting procedure described above, rate constants can be extracted and plotted in Table 1. The error bar indicates uncertainty in fittings. The most significant difference lies in the second reaction pathway,  $\tau_2$ . For pH  $< 13$ , the extracted rate constant shows a prolonged  $\tau_2$  close to 120  $\mu\text{s}$  in D<sub>2</sub>O solution, indicating a slower reaction rate. Quantitatively, the ratio of  $\tau_2(\text{D})/\tau_2(\text{H})$  is close to 1.8. For pH = 14,  $\tau_2(\text{D})$  remains the same with  $\tau_2(\text{H})$  at low excitation density. At higher excitation density,  $\tau_2(\text{D})/\tau_2(\text{H})$  recovers to 1.8. Rate constant ratio of 1.8 has been observed before in other catalytic systems<sup>111-114</sup> and it is an indication of H<sub>2</sub>O participating in the reaction process.

## 6.4 Discussion

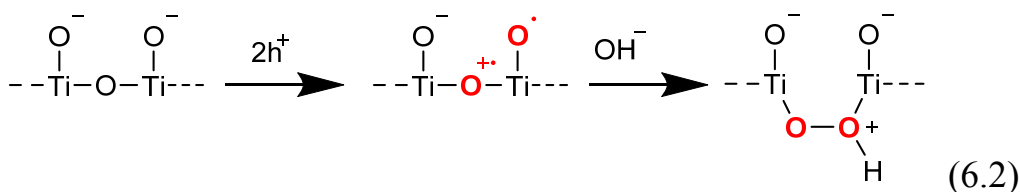
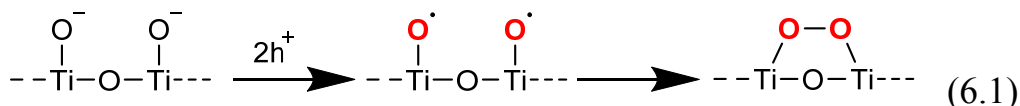
The decay time constant of initial water oxidation intermediates highly depends on ionic strength, solution pH and isotopes. The combination of three can provide

some insights into understanding water oxidation process. The following reaction pathways can be proposed.

Table 1: Fitted rate constant for different pH's in H<sub>2</sub>O and D<sub>2</sub>O

pH	H <sub>2</sub> O		D <sub>2</sub> O		$\tau_1(\text{D})/\tau_1(\text{H})$	$\tau_2(\text{D})/\tau_2(\text{H})$
	$\tau_1(\mu\text{s})$	$\tau_2(\mu\text{s})$	$\tau_1(\mu\text{s})$	$\tau_2(\mu\text{s})$		
7	$8.6 \pm 1.6$	$62.7 \pm 2.3$	$9.2 \pm 2.6$	$113.1 \pm 10$	1.07	1.8
10	$8.6 \pm 0.7$	$65 \pm 10.7$	$8.5 \pm 1$	$115.5 \pm 12.4$	0.99	1.78
11	$8.8 \pm 2.8$	$72.5 \pm 17.4$	$10.9 \pm 1.3$	$125.2 \pm 13.6$	1.24	1.73
12	$8.7 \pm 0.4$	$60 \pm 6.2$	$10 \pm 1.2$	$100 \pm 10.1$	1.15	1.67
13	$7.3 \pm 0.3$	$58.5 \pm 14$	$10.6 \pm 1$	$103.7 \pm 14$	1.45	1.77
13.3	$4.8 \pm 0.5$	$22.9 \pm 8$	$5.8 \pm 0.3$	$38.4 \pm 8$	1.21	1.68
14	$0.7 \pm 0.1$	$7.3 \pm 1.4$	$0.7 \pm 0.1$	$7.7 \pm 1.4$	1	1.05
14*	$1.5 \pm 0.1$	$18.9 \pm 4.2$	$2.0 \pm 0.1$	$35.4 \pm 5.1$	1.33	1.87

\* indicating at higher incident fluence of 0.2 mJ/cm<sup>2</sup>



Pathway 6.1 represents the fast  $\tau_1$  kinetics to form the critical O-O bond from initial intermediates. Two Ti-O• directly combine and form an *out-of-plane* O-O bond. Water does not participate O-O bond formation and no H/D isotope effect is expected. Ionic strength though affect the speed of this process as two Ti-O• have to be nearest neighbor in order to combine. Higher ionic strength might facilitate the process of moving two Ti-O• next to each other. Pathway 6.2 represents the slower  $\tau_2$  kinetics to form O-O bond. One Ti-O• and one Ti-O•-Ti react with one OH<sup>-</sup> to form *in-plane* O-O bond. An OH<sup>-</sup> is needed in this process such that kinetic isotope effect can be observed. Ionic strength could also affect this process. With change in solution pH, the initial surface condition is changed and potentially, the relative

number of  $\text{Ti-O}\cdot$  and  $\text{Ti-O}\cdot\text{-Ti}$  reacting through each pathway are changed accordingly.

## 6.5 Conclusion

We have identified the time constant by which oxyl ( $\text{Ti-O}\cdot$ ) and bridge ( $\text{Ti-O}\cdot\text{-Ti}$ ) radicals react to form critical intermediates ( $\text{O-O}$ ) at the  $\text{n-SrTiO}_3$ /aqueous interface during photo-catalytic water oxidation. The time constants are dependent on solution ionic strength and isotopes but not on solution pH. This led to two proposed mechanisms for forming stable  $\text{O-O}$  reaction intermediates.

# Bibliography

1. IEA Key World Energy Statistics. **2016**.
2. American Association for the Advancement of Science Joint-statement on climate change by leaders of 18 scientific organizations. **2014**.
3. Bube, R. H. *Photovoltaic Materials*; Imperial College Press: London, 1998; .
4. Heeger, A. Solar Fuels and Artificial Photosynthesis. *RSC* **2012**.
5. Styring, S. Artificial photosynthesis for solar fuels. *Faraday Discuss.* **2012**, *155*, 357-376.
6. FUJISHIMA, A.; HONDA, K. Electrochemical Photolysis of Water at a Semiconductor Electrode. *Nature* **1972**, *238*, 37-38.
7. Ascroft, N. M.; Mermin, N. D. *Solid State Physics*; Holt, Rinehart and Winston: 1976; .
8. Sze, S. M.; Ng, K. K. *Physics of Semiconductor Devices, 3rd Edition*; Wiley-Interscience: 2006; .
9. Zhang, M.; de Respinis, M.; Frei, H. Time-resolved observations of water oxidation intermediates on a cobalt oxide nanoparticle catalyst. *Nat Chem* **2014**, *6*, 362-367.
10. Chen, X.; Choing, S. N.; Aschaffenburg, D. J.; Pemmaraju, C. D.; Prendergast, D.; Cuk, T. The Formation Time of Ti-O• and Ti-O•-Ti Radicals at the n-SrTiO<sub>3</sub>/Aqueous Interface during Photocatalytic Water Oxidation. *J. Am. Chem. Soc.* **2017**, *139*, 1830-1841.
11. Khaselev, O.; Turner, J. A. A Monolithic Photovoltaic-Photoelectrochemical Device for Hydrogen Production via Water Splitting. *Science* **1998**, *280*, 425-427.
12. Reece, S. Y.; Hamel, J. A.; Sung, K.; Jarvi, T. D.; Esswein, A. J.; Pijpers, J. J. H.; Nocera, D. G. Wireless Solar Water Splitting Using Silicon-Based Semiconductors and Earth-Abundant Catalysts. *Science* **2011**, *334*, 645-648.
13. Kudo, A.; Miseki, Y. Heterogeneous photocatalyst materials for water splitting. *Chem. Soc. Rev.* **2009**, *38*, 253-278.
14. Moulton, P. F. Spectroscopic and laser characteristics of Ti:Al<sub>2</sub>O<sub>3</sub>. *J Opt Soc Am B* **1986**, *3*, 125-133.
15. Bockris, J. O. M.; Khan, S. U. M. *Surface Electrochemistry*; Springer: New York, NY, 1993; .
16. Kasinski, J. J.; Gomez-Jahn, L. A.; Faran, K. J.; Gracewski, S. M.; Miller, R. J. D. Picosecond dynamics of surface electron transfer processes: Surface

- restricted transient grating studies of the n-TiO<sub>2</sub>/H<sub>2</sub>O interface. *J. Chem. Phys.* **1989**, *90*, 1253-1269.
17. Nakamura, R.; Nakato, Y. Primary Intermediates of Oxygen Photoevolution Reaction on TiO<sub>2</sub> (Rutile) Particles, Revealed by in Situ FTIR Absorption and Photoluminescence Measurements. *J. Am. Chem. Soc.* **2004**, *126*, 1290-1298.
  18. Lantz, J. M.; Corn, R. M. Time-resolved optical second harmonic generation measurements of picosecond band flattening processes at single crystal TiO<sub>2</sub> electrodes. *J. Phys. Chem.* **1994**, *98*, 9387-9390.
  19. Tang, J.; Durrant, J. R.; Klug, D. R. Mechanism of Photocatalytic Water Splitting in TiO<sub>2</sub>. Reaction of Water with Photoholes, Importance of Charge Carrier Dynamics, and Evidence for Four-Hole Chemistry. *J. Am. Chem. Soc.* **2008**, *130*, 13885-13891.
  20. Cowan, A. J.; Barnett, C. J.; Pendlebury, S. R.; Barroso, M.; Sivula, K.; Grätzel, M.; Durrant, J. R.; Klug, D. R. Activation Energies for the Rate-Limiting Step in Water Photooxidation by Nanostructured  $\alpha$ -Fe<sub>2</sub>O<sub>3</sub> and TiO<sub>2</sub>. *J. Am. Chem. Soc.* **2011**, *133*, 10134-10140.
  21. Huang, Z.; Lin, Y.; Xiang, X.; Rodriguez-Cordoba, W.; McDonald, K. J.; Hagen, K. S.; Choi, K.; Brunschwig, B. S.; Musaev, D. G.; Hill, C. L.; Wang, D.; Lian, T. In situ probe of photocarrier dynamics in water-splitting hematite ( $\alpha$ -Fe<sub>2</sub>O<sub>3</sub>) electrodes. *Energy Environ. Sci.* **2012**, *5*, 8923-8926.
  22. Green, M. Electrochemistry of the Semiconductor-Electrolyte Electrode. I. The Electrical Double Layer. *J. Chem. Phys.* **1959**, *31*, 200-203.
  23. De Gryse, R.; Gomes, W. P.; Cardon, F.; Vennik, J. On the Interpretation of Mott-Schottky Plots Determined at Semiconductor/Electrolyte Systems. *J. Electrochem. Soc.* **1975**, *122*, 711-712.
  24. Uosaki, K.; Kita, H. Effects of the Helmholtz Layer Capacitance on the Potential Distribution at Semiconductor/Electrolyte Interface and the Linearity of the Mott-Schottky Plot. *J. Electrochem. Soc.* **1983**, *130*, 895-897.
  25. Cooper, G.; Turner, J. A.; Parkinson, B. A.; Nozik, A. J. Hot carrier injection of photogenerated electrons at indium phosphide-electrolyte interfaces. *J. Appl. Phys.* **1983**, *54*, 6463-6473.
  26. Turner, J. A.; Manassen, J.; Nozik, A. J. Photoelectrochemistry with p-Si electrodes: Effects of inversion. *Appl. Phys. Lett.* **1980**, *37*, 488-491.
  27. van Benthem, K.; Elsässer, C.; French, R. H. Bulk electronic structure of SrTiO<sub>3</sub>: Experiment and theory. *J. Appl. Phys.* **2001**, *90*, 6156-6164.
  28. van de Krol, R.; Grätzel, M. *Photoelectrochemical Hydrogen Production*; Springer: New York, NY, 2012; Vol. 102, pp 13-67.

29. Green, M. Electrochemistry of the Semiconductor□Electrolyte Electrode. I. The Electrical Double Layer. *J. Chem. Phys.* **1959**, *31*, 200-203.
30. Uosaki, K.; Kita, H. Effects of the Helmholtz Layer Capacitance on the Potential Distribution at Semiconductor/Electrolyte Interface and the Linearity of the Mott-Schottky Plot. *J. Electrochem. Soc.* **1983**, *130*, 895-897.
31. Du, C.; Yang, X.; Mayer, M. T.; Hoyt, H.; Xie, J.; McMahon, G.; Bischoff, G.; Wang, D. Hematite-Based Water Splitting with Low Turn-On Voltages. *Angew. Chem. Int. Ed.* **2013**, *52*, 12692-12695.
32. Bard, A. J.; Bocarsly, A. B.; Fan, F. R. F.; Walton, E. G.; Wrighton, M. S. The concept of Fermi level pinning at semiconductor/liquid junctions. Consequences for energy conversion efficiency and selection of useful solution redox couples in solar devices. *J. Am. Chem. Soc.* **1980**, *102*, 3671-3677.
33. Xu, Y.; Schoonen, M. A. A. The absolute energy positions of conduction and valence bands of selected semiconducting minerals. *Am. Mineral.* **2000**, *85*, 543-556.
34. Fishman, I. M.; Marshall, C. D.; Meth, J. S.; Fayer, M. D. Surface selectivity in four-wave mixing: transient gratings as a theoretical and experimental example. *J Opt Soc Am B* **1991**, *8*, 1880-1888.
35. Yamada, Y.; Yasuda, H.; Tayagaki, T.; Kanemitsu, Y. Photocarrier recombination dynamics in highly excited SrTiO<sub>3</sub> studied by transient absorption and photoluminescence spectroscopy. *Appl. Phys. Lett.* **2009**, *95*, 121112.
36. Tufte, O. N.; Chapman, P. W. Electron Mobility in Semiconducting Strontium Titanate. *Phys. Rev.* **1967**, *155*, 796-802.
37. Wardman, P. Reduction Potentials of One□Electron Couples Involving Free Radicals in Aqueous Solution. *J. Phys. Chem. Ref. Data* **1989**, *18*, 1637-1755.
38. Bard, A. J.; Faulkner, L. R. *Electrochemical Methods: Fundamentals and Applications, 2nd edition*; Wiley: Hoboken, NJ, 2000; .
39. Koppenol, W. H.; Liebman, J. F. The oxidizing nature of the hydroxyl radical. A comparison with the ferryl ion (FeO<sub>2</sub><sup>+</sup>). *J. Phys. Chem.* **1984**, *88*, 99-101.
40. Bard, A. J.; Parsons, R.; Jordan, J. *Standard Potentials in Aqueous Solution*; Taylor & Francis: 1985; .
41. Cheng, J.; Sulpizi, M.; VandeVondele, J.; Sprik, M. Hole Localization and Thermochemistry of Oxidative Dehydrogenation of Aqueous Rutile TiO<sub>2</sub>(110). *ChemCatChem* **2012**, *4*, 636-640.
42. Su, H.; Gorlin, Y.; Man, I. C.; Calle-Vallejo, F.; Norskov, J. K.; Jaramillo, T. F.; Rossmeisl, J. Identifying active surface phases for metal oxide electrocatalysts: a study of manganese oxide bi-functional catalysts for oxygen

- reduction and water oxidation catalysis. *Phys. Chem. Chem. Phys.* **2012**, *14*, 14010-14022.
43. Liao, P.; Keith, J. A.; Carter, E. A. Water Oxidation on Pure and Doped Hematite (0001) Surfaces: Prediction of Co and Ni as Effective Dopants for Electrocatalysis. *J. Am. Chem. Soc.* **2012**, *134*, 13296-13309.
  44. Bajdich, M.; García-Mota, M.; Vojvodic, A.; Nørskov, J. K.; Bell, A. T. Theoretical Investigation of the Activity of Cobalt Oxides for the Electrochemical Oxidation of Water. *J. Am. Chem. Soc.* **2013**, *135*, 13521-13530.
  45. Alibabaei, L.; Brennaman, M. K.; Norris, M. R.; Kalanyan, B.; Song, W.; Losego, M. D.; Concepcion, J. J.; Binstead, R. A.; Parsons, G. N.; Meyer, T. J. Solar water splitting in a molecular photoelectrochemical cell. *Proc. Natl. Acad. Sci. U. S. A.* **2013**, *110*, 20008-20013.
  46. Liu, F.; Concepcion, J. J.; Jurss, J. W.; Cardolaccia, T.; Templeton, J. L.; Meyer, T. J. Mechanisms of Water Oxidation from the Blue Dimer to Photosystem II. *Inorg. Chem.* **2008**, *47*, 1727-1752.
  47. Ramasesha, K.; De Marco, L.; Mandal, A.; Tokmakoff, A. Water vibrations have strongly mixed intra- and intermolecular character. *Nat Chem* **2013**, *5*, 935-940.
  48. Renger, G. Light induced oxidative water splitting in photosynthesis: Energetics, kinetics and mechanism. *Journal of Photochemistry and Photobiology B: Biology* **2011**, *104*, 35-43.
  49. Yano, J.; Yachandra, V. K. Where Water Is Oxidized to Dioxygen: Structure of the Photosynthetic Mn<sub>4</sub>Ca Cluster from X-ray Spectroscopy. *Inorg. Chem.* **2008**, *47*, 1711-1726.
  50. Tagore, R.; Crabtree, R. H.; Brudvig, G. W. Oxygen Evolution Catalysis by a Dimanganese Complex and Its Relation to Photosynthetic Water Oxidation. *Inorg. Chem.* **2008**, *47*, 1815-1823.
  51. Siegbahn, P. E. M. Theoretical Studies of O-O Bond Formation in Photosystem II. *Inorg. Chem.* **2008**, *47*, 1779-1786.
  52. Cummings, C. Y.; Marken, F.; Peter, L. M.; Wijayantha, K. G. U.; Tahir, A. A. New Insights into Water Splitting at Mesoporous  $\alpha$ -Fe<sub>2</sub>O<sub>3</sub> Films: A Study by Modulated Transmittance and Impedance Spectroscopies. *J. Am. Chem. Soc.* **2012**, *134*, 1228.
  53. Klahr, B.; Hamann, T. Water Oxidation on Hematite Photoelectrodes: Insight into the Nature of Surface States through In Situ Spectroelectrochemistry. *J. Phys. Chem. C* **2014**, *118*, 10393.

54. Norton, A. P.; Bernasek, S. L.; Bocarsly, A. B. Mechanistic aspects of the photooxidation of water at the n-titania/aqueous interface: optically induced transients as a kinetic probe. *J. Phys. Chem.* **1988**, *92*, 6009-6016.
55. Imanishi, A.; Okamura, T.; Ohashi, N.; Nakamura, R.; Nakato, Y. Mechanism of Water Photooxidation Reaction at Atomically Flat TiO<sub>2</sub> (Rutile) (110) and (100) Surfaces: Dependence on Solution pH. *J. Am. Chem. Soc.* **2007**, *129*, 11569-11578.
56. Micic, O. I.; Zhang, Y.; Cromack, K. R.; Trifunac, A. D.; Thurnauer, M. C. Trapped holes on titania colloids studied by electron paramagnetic resonance. *J. Phys. Chem.* **1993**, *97*, 7277-7283.
57. Kanan, M. W.; Yano, J.; Surendranath, Y.; Dincă, M.; Yachandra, V. K.; Nocera, D. G. Structure and Valency of a Cobalt-Phosphate Water Oxidation Catalyst Determined by in Situ X-ray Spectroscopy. *J. Am. Chem. Soc.* **2010**, *132*, 13692-13701.
58. McAlpin, J. G.; Stich, T. A.; Ohlin, C. A.; Surendranath, Y.; Nocera, D. G.; Casey, W. H.; Britt, R. D. Electronic Structure Description of a [Co(III)<sub>3</sub>Co(IV)O<sub>4</sub>] Cluster: A Model for the Paramagnetic Intermediate in Cobalt-Catalyzed Water Oxidation. *J. Am. Chem. Soc.* **2011**, *133*, 15444-15452.
59. Surendranath, Y.; Kanan, M. W.; Nocera, D. G. Mechanistic Studies of the Oxygen Evolution Reaction by a Cobalt-Phosphate Catalyst at Neutral pH. *J. Am. Chem. Soc.* **2010**, *132*, 16501-16509.
60. Bediako, D. K.; Costentin, C.; Jones, E. C.; Nocera, D. G.; Savéant, J. Proton-Electron Transport and Transfer in Electrocatalytic Films. Application to a Cobalt-Based O<sub>2</sub>-Evolution Catalyst. *J. Am. Chem. Soc.* **2013**, *135*, 10492-10502.
61. Bediako, D. K.; Surendranath, Y.; Nocera, D. G. Mechanistic Studies of the Oxygen Evolution Reaction Mediated by a Nickel-Borate Thin Film Electrocatalyst. *J. Am. Chem. Soc.* **2013**, *135*, 3662-3674.
62. Huynh, M.; Bediako, D. K.; Nocera, D. G. A Functionally Stable Manganese Oxide Oxygen Evolution Catalyst in Acid. *J. Am. Chem. Soc.* **2014**, *136*, 6002-6010.
63. Lane, I. M.; King, D. A.; Liu, Z.; Arnolds, H. Real-Time Observation of Nonadiabatic Surface Dynamics: The First Picosecond in the Dissociation of NO on Iridium. *Phys. Rev. Lett.* **2006**, *97*, 186105.
64. Haran, G.; Sun, W. D.; Wynne, K.; Hochstrasser, R. M. Femtosecond far-infrared pump-probe spectroscopy: A new tool for studying low-frequency

- vibrational dynamics in molecular condensed phases. *Chem. Phys. Lett.* **1997**, *274*, 365-371.
65. Roberts, S. T.; Ramasesha, K.; Petersen, P. B.; Mandal, A.; Tokmakoff, A. Proton Transfer in Concentrated Aqueous Hydroxide Visualized Using Ultrafast Infrared Spectroscopy. *J. Phys. Chem. A* **2011**, *113*, 3957.
  66. Bakker, H.; Bonn, M.; Fayer, M. *Femtosecond Vibrational Spectroscopy of Aqueous Systems*; CRC Press: Florida: 2013; .
  67. Milosevic, M. *Internal Reflection and ATR Spectroscopy*; John Wiley & Sons, Inc: 2012; , pp 264.
  68. Hussain, H.; Torrelles, X.; Rajput, P.; Nicotra, M.; Thornton, G.; Zegenhagen, J. A Quantitative Structural Investigation of the 0.1 wt % Nb-SrTiO<sub>3</sub>(001)/H<sub>2</sub>O Interface. *J. Phys. Chem. C* **2014**, *118*, 10980-10988.
  69. Ketteler, G.; Yamamoto, S.; Bluhm, H.; Andersson, K.; Starr, D. E.; Ogletree, D. F.; Ogasawara, H.; Nilsson, A.; Salmeron, M. The Nature of Water Nucleation Sites on TiO<sub>2</sub>(110) Surfaces Revealed by Ambient Pressure X-ray Photoelectron Spectroscopy. *J. Phys. Chem. C* **2007**, *111*, 8278-8282.
  70. Barker, A. S. Temperature Dependence of the Transverse and Longitudinal Optic Mode Frequencies and Charges in SrTiO<sub>3</sub> and BaTiO<sub>3</sub>. *Phys. Rev.* **1966**, *145*, 391-399.
  71. Fischer, B.; Bäuerle, D.; Buckel, W. J. Surface polaritons in KTaO<sub>3</sub> and SrTiO<sub>3</sub>. *Solid. State. Commun.* **1974**, *14*, 291-294.
  72. Wrighton, M. S.; Ellis, A. B.; Wolczanski, P. T.; Morse, D. L.; Abrahamson, H. B.; Ginley, D. S. Strontium titanate photoelectrodes. Efficient photoassisted electrolysis of water at zero applied potential. *J. Am. Chem. Soc.* **1976**, *98*, 2774-2779.
  73. Zhu, Y.; Uchida, H.; Watanabe, M. Oxidation of Carbon Monoxide at a Platinum Film Electrode Studied by Fourier Transform Infrared Spectroscopy with Attenuated Total Reflection Technique. *Langmuir* **1999**, *15*, 8757-8764.
  74. Zhu, Y.; Uchida, H.; Yajima, T.; Watanabe, M. Attenuated Total Reflection-Fourier Transform Infrared Study of Methanol Oxidation on Sputtered Pt Film Electrode. *Langmuir* **2001**, *17*, 146-154.
  75. Fano, U. Effects of Configuration Interaction on Intensities and Phase Shifts. *Phys. Rev.* **1961**, *124*, 1866-1878.
  76. Gervais, F.; Servoin, J.; Baratoff, A.; Bednorz, J. G.; Binnig, G. Temperature dependence of plasmons in Nb-doped SrTiO<sub>3</sub>. *Phys. Rev. B* **1993**, *47*, 8187-8194.
  77. Giguère, P. A.; Harvey, K. B. On the infrared absorption of water and heavy water in condensed states. *Can. J. Chem.* **1956**, *34*, 798-808.

78. Lappi, S. E.; Smith, B.; Franzen, S. Infrared spectra of H<sub>2</sub><sup>16</sup>O, H<sub>2</sub><sup>18</sup>O and D<sub>2</sub>O in the liquid phase by single-pass attenuated total internal reflection spectroscopy. *Spectrochim. Acta Mol. Biomol. Spectrosc.* **2004**, *60*, 2611-2619.
79. McIntyre, J. D. E.; Aspnes, D. E. Differential reflection spectroscopy of very thin surface films. *Surf. Sci.* **1971**, *24*, 417-434.
80. Waegele, M. M.; Doan, H. Q.; Cuk, T. Long-Lived Photoexcited Carrier Dynamics of d–d Excitations in Spinel Ordered Co<sub>3</sub>O<sub>4</sub>. *J. Phys. Chem. C* **2014**, *118*, 3426-3432.
81. Giustino, F.; Pasquarello, A. Infrared Spectra at Surfaces and Interfaces from First Principles: Evolution of the Spectra across the Si(100)\SiO<sub>2</sub> Interface. *Phys. Rev. Lett.* **2005**, *95*, 187402.
82. Eisenberg, R.; Gray, H. B. Preface on Making Oxygen. *Inorg. Chem.* **2008**, *47*, 1697-1699.
83. García-Mota, M.; Vojvodic, A.; Abild-Pedersen, F.; Nørskov, J. K. Electronic Origin of the Surface Reactivity of Transition-Metal-Doped TiO<sub>2</sub>(110). *J. Phys. Chem. C* **2013**, *117*, 460-465.
84. Waegele, M. M.; Chen, X.; Herlihy, D. M.; Cuk, T. How Surface Potential Determines the Kinetics of the First Hole Transfer of Photocatalytic Water Oxidation. *J. Am. Chem. Soc.* **2014**, *136*, 10632-10639.
85. Herlihy, D. M.; Waegele, M. M.; Chen, X.; Pemmaraju, C. D.; Prendergast, D.; Cuk, T. Detecting the oxyl radical of photocatalytic water oxidation at an n-SrTiO<sub>3</sub>/aqueous interface through its subsurface vibration. *Nat Chem* **2016**, *8*, 549-555.
86. Yamada, Y.; Sato, H. K.; Hikita, Y.; Hwang, H. Y.; Kanemitsu, Y. Measurement of the Femtosecond Optical Absorption of LaAlO<sub>3</sub>/SrTiO<sub>3</sub> Heterostructures: Evidence for an Extremely Slow Electron Relaxation at the Interface. *Phys. Rev. Lett.* **2013**, *111*, 047403.
87. McGuire, J. A.; Shen, Y. R. Ultrafast Vibrational Dynamics at Water Interfaces. *Science* **2006**, *313*, 1945-1948.
88. Gilijamse, J. J.; Lock, A. J.; Bakker, H. J. Dynamics of confined water molecules. *Proc. Natl. Acad. Sci.* **2005**, *102*, 3202-3207.
89. Laenen, R.; Simeonidis, K.; Laubereau, A. Subpicosecond Spectroscopy of Liquid Water in the Infrared: Effect of Deuteration on the Structural and Vibrational Dynamics. *J. Phys. Chem. B* **2002**, *106*, 408-417.
90. Kresse, G.; Furthmüller, J. Efficiency of ab-initio total energy calculations for metals and semiconductors using a plane-wave basis set. *Computational Materials Science* **1996**, *6*, 15-50.

91. Kresse, G.; Furthmüller, J. Efficient iterative schemes for ab initio total-energy calculations using a plane-wave basis set. *Phys. Rev. B* **1996**, *54*, 11169-11186.
92. Sun, Y.; Pignatello, J. J. Evidence for a surface dual hole-radical mechanism in the titanium dioxide photocatalytic oxidation of 2,4-D. *Environ. Sci. Technol.* **1995**, *29*, 2065-2072.
93. Grabner, L. Photoluminescence in SrTiO<sub>3</sub>. *Phys. Rev.* **1969**, *177*, 1315-1323.
94. Herman, I. P. *Optical Diagnostics for Thin Film Processing*; Academic Press, Inc.: San Diego, CA, 1996; .
95. Shayduk, R.; Herzog, M.; Bojahr, A.; Schick, D.; Gaal, P.; Leitenberger, W.; Navirian, H.; Sander, M.; Goldshteyn, J.; Vrejoiu, I.; Bargheer, M. Direct time-domain sampling of subterahertz coherent acoustic phonon spectra in SrTiO<sub>3</sub> using ultrafast x-ray diffraction. *Phys. Rev. B* **2013**, *87*, 184301.
96. Janotti, A.; Varley, J. B.; Choi, M.; Van de Walle, C. G. Vacancies and small polarons in SrTiO<sub>3</sub>. *Phys. Rev. B* **2014**, *90*, 085202.
97. Sponza, L.; Véniard, V.; Sottile, F.; Giorgetti, C.; Reining, L. Role of localized electrons in electron-hole interaction: The case of SrTiO<sub>3</sub>. *Phys. Rev. B* **2013**, *87*, 235102.
98. Mochizuki, S.; Fujishiro, F.; Minami, S. Photoluminescence and reversible photo-induced spectral change of SrTiO<sub>3</sub>. *J. Phys. Condens. Matter* **2005**, *17*, 923.
99. Steinel, T.; Asbury, J. B.; Zheng, J.; Fayer, M. D. Watching Hydrogen Bonds Break: A Transient Absorption Study of Water. *J. Phys. Chem. A* **2004**, *108*, 10957-10964.
100. Kropman, M. F.; Nienhuys, H.; Woutersen, S.; Bakker, H. J. Vibrational Relaxation and Hydrogen-Bond Dynamics of HDO:H<sub>2</sub>O. *J. Phys. Chem. A* **2001**, *105*, 4622-4626.
101. Ramasesha, K.; De Marco, L.; Mandal, A.; Tokmakoff, A. Water vibrations have strongly mixed intra- and intermolecular character. *Nat Chem* **2013**, *5*, 935-940.
102. Fecko, C. J.; Loparo, J. J.; Roberts, S. T.; Tokmakoff, A. Local hydrogen bonding dynamics and collective reorganization in water: Ultrafast infrared spectroscopy of HOD/D<sub>2</sub>O. *J. Chem. Phys.* **2005**, *122*, 054506.
103. Asbury, J. B.; Steinel, T.; Stromberg, C.; Corcelli, S. A.; Lawrence, C. P.; Skinner, J. L.; Fayer, M. D. Water Dynamics: Vibrational Echo Correlation Spectroscopy and Comparison to Molecular Dynamics Simulations. *J. Phys. Chem. A* **2004**, *108*, 1107-1119.
104. Lock, A. J.; Bakker, H. J. Temperature dependence of vibrational relaxation in liquid H<sub>2</sub>O. *J. Chem. Phys.* **2002**, *117*, 1708-1713.

105. Eftekhari-Bafrooei, A.; Borguet, E. Effect of Hydrogen-Bond Strength on the Vibrational Relaxation of Interfacial Water. *J. Am. Chem. Soc.* **2010**, *132*, 3756-3761.
106. Cheng, J.; VandeVondele, J.; Sprik, M. Identifying Trapped Electronic Holes at the Aqueous TiO<sub>2</sub> Interface. *J. Phys. Chem. C* **2014**, *118*, 5437-5444.
107. Kolesov, G.; Grånäs, O.; Hoyt, R.; Vinichenko, D.; Kaxiras, E. Real-Time TD-DFT with Classical Ion Dynamics: Methodology and Applications. *J. Chem. Theory Comput.* **2016**, *12*, 466-476.
108. Harriman, A.; Pickering, I. J.; Thomas, J. M.; Christensen, P. A. Metal oxides as heterogeneous catalysts for oxygen evolution under photochemical conditions. *J. Chem. Soc., Faraday Trans. 1* **1988**, *84*, 2795-2806.
109. Limburg, J.; Vrettos, J. S.; Liable-Sands, L. M.; Rheingold, A. L.; Crabtree, R. H.; Brudvig, G. W. A Functional Model for O-O Bond Formation by the O<sub>2</sub>-Evolving Complex in Photosystem II. *Science* **1999**, *283*, 1524-1527.
110. Sivasankar, N.; Weare, W. W.; Frei, H. Direct Observation of a Hydroperoxide Surface Intermediate upon Visible Light-Driven Water Oxidation at an Ir Oxide Nanocluster Catalyst by Rapid-Scan FT-IR Spectroscopy. *J. Am. Chem. Soc.* **2011**, *133*, 12976-12979.
111. Oloo, W. N.; Fielding, A. J.; Que, L. Rate-Determining Water-Assisted O-O Bond Cleavage of an FeIII-OOH Intermediate in a Bio-inspired Nonheme Iron-Catalyzed Oxidation. *J. Am. Chem. Soc.* **2013**, *135*, 6438-6441.
112. Li, F.; Fan, K.; Wang, L.; Daniel, Q.; Duan, L.; Sun, L. Immobilizing Ru(bda) Catalyst on a Photoanode via Electrochemical Polymerization for Light-Driven Water Splitting. *ACS Catal.* **2015**, *5*, 3786-3790.
113. Zaharieva, I.; Dau, H.; Haumann, M. Sequential and Coupled Proton and Electron Transfer Events in the S<sub>2</sub> → S<sub>3</sub> Transition of Photosynthetic Water Oxidation Revealed by Time-Resolved X-ray Absorption Spectroscopy. *Biochemistry (N. Y.)* **2016**, *55*, 6996-7004.
114. Saavedra, J.; Doan, H. A.; Pursell, C. J.; Grabow, L. C.; Chandler, B. D. The critical role of water at the gold-titania interface in catalytic CO oxidation. *Science* **2014**, *345*, 1599-1602.

## Appendices

Here shows the photocurrent vs potential curve for steady state light excitation of n-SrTiO<sub>3</sub> in 0.1M NaOH solutions. Similar behavior is observed compared to single wavelength laser excitation as a supplemental for chapter 3.

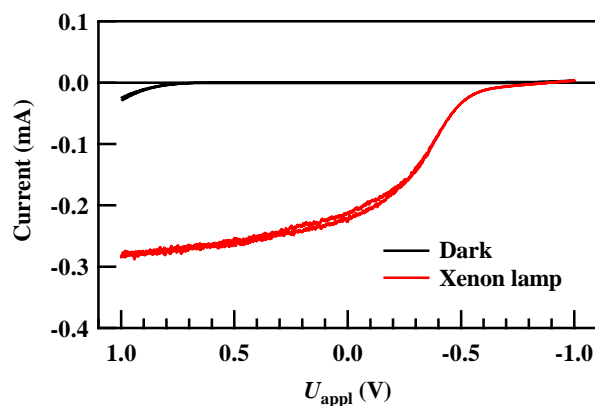


**Figure A1:** Cyclic voltammogram of n-SrTiO<sub>3</sub> in the dark and under irradiation by a 150 W Xenon lamp. Similar to the current-voltage curve under laser irradiation, a diode-like behavior was observed under Xenon lamp irradiation. Note that compared to the data in Figure 1a, the photo-current is less potential independent in the range of  $-0.5$  V to 1 V. The reason for this is that under Xenon lamp irradiation, a broad range of UV wavelengths was used, all with separate efficiencies for generating photocurrent.

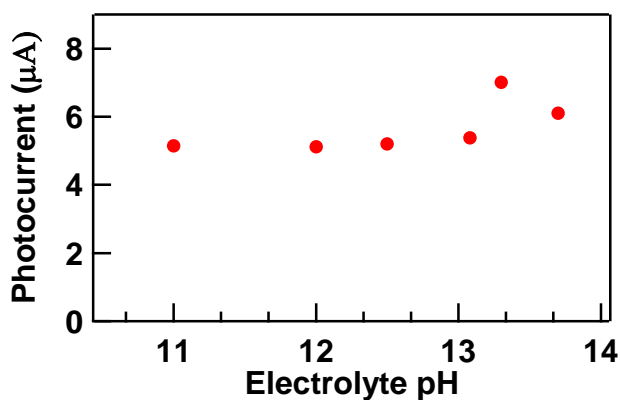


**Figure A2:** Steady state photocurrent of n-SrTiO<sub>3</sub> under an incident laser fluence of  $0.04$  mJ/cm<sup>2</sup> as a function of pH. The steady state photocurrent is not changing significantly with the pH of the solution, suggesting the reaction is not mass diffusion limited.

Here shows supplemental for chapter 4.

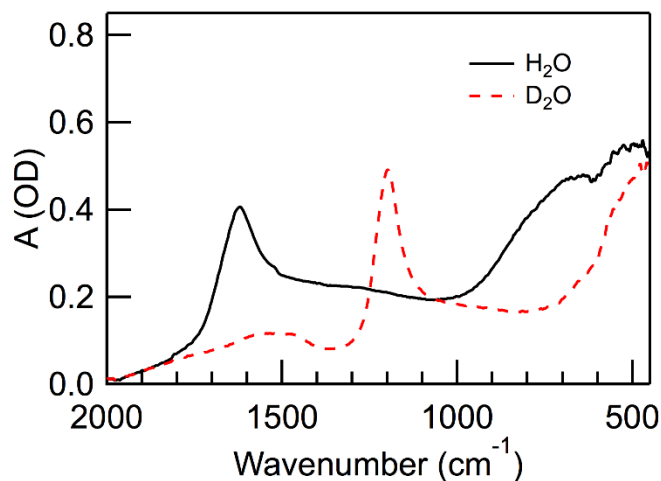


**Figure A3: Attenuated total reflection of H<sub>2</sub>O and D<sub>2</sub>O**

This spectrum shows that the librational frequency changes from H<sub>2</sub>O to D<sub>2</sub>O. With H<sub>2</sub>O, the librational frequency centers around 500 cm<sup>-1</sup> and extending to 1000 cm<sup>-1</sup>. In D<sub>2</sub>O, the librational frequency shows a red shift and centers at below 500 cm<sup>-1</sup>. The relative spectral weight at c.a. 800 cm<sup>-1</sup> is lower for D<sub>2</sub>O than H<sub>2</sub>O.

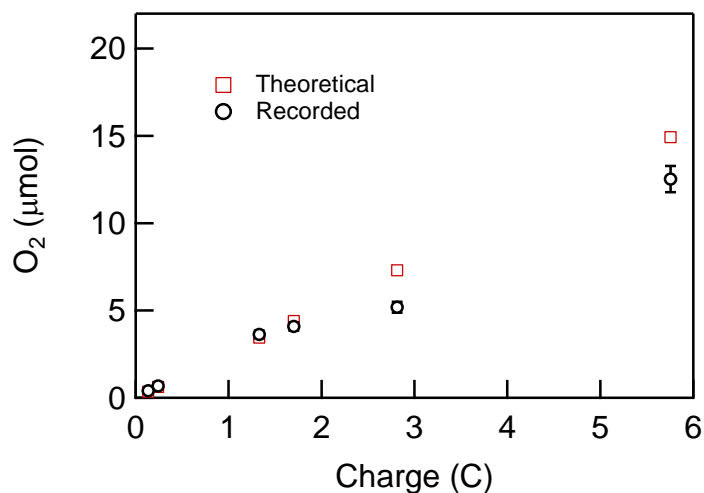


**Figure A4: Observed O<sub>2</sub> Evolution.** The theoretical (100% faradaic efficiency) and observed oxygen evolution at the SrTiO<sub>3</sub> single crystal are nearly identical. Deviation in longer experiments is attributed to O<sub>2</sub> leaks into the oxygen-free environment.

A 5 x 5 mm sample of 0.1% Nb-doped SrTiO<sub>3</sub> was enclosed in a two-electrode spectroelectrochemical cell with Pt wire counter electrode and 1.0M NaOH electrolyte. The polished side of the sample was irradiated with UV light from a 300W Xe lamp with IR-cut filter. A potentiostat was used to measure the charge passed, and an electrochemical O<sub>2</sub> gas sensor (RapidOx 1100L, Cambridge Sensotec, Cambridge, UK) with built in circulation pump and temperature/pressure correction software recorded the partial pressure of molecular oxygen with ppb resolution. After correcting for oxygen dissolved in the electrolyte (10 mL) the partial pressure was converted to moles using the ideal gas law (144 mL headspace, 1.05 atm, 298K). The entire experiment was performed in a pressure-controlled dry-nitrogen (O<sub>2</sub> < 1 ppb) glove box. The slight deviation from 100% faradaic efficiency at the longest experiments (17 hours, 5.8 C) is attributed to loss of O<sub>2</sub> due to leakage into the oxygen-free glove box.

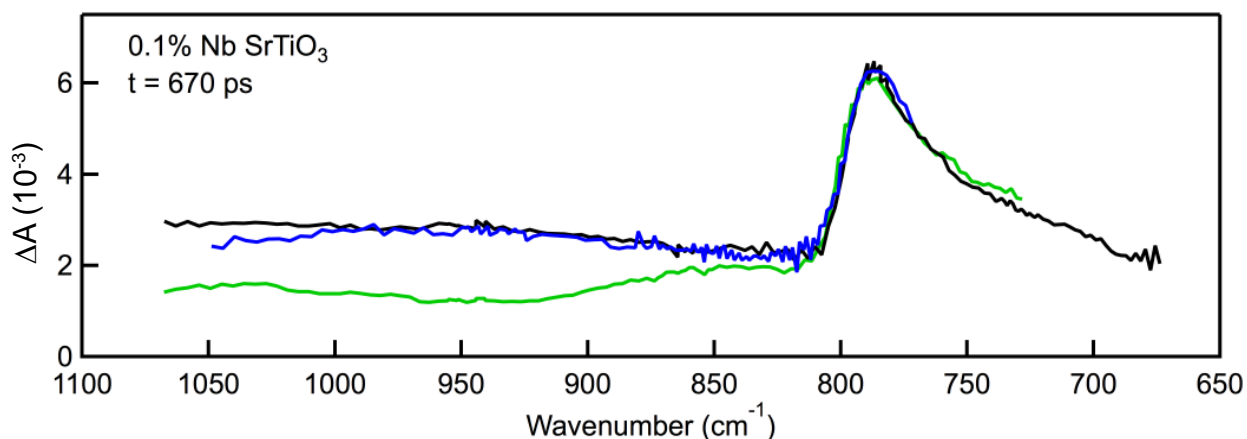


**Figure A5: Transient-Infrared Spectra from 675 – 1070 cm<sup>-1</sup>.** In the course of the investigation a broader energy range was initially probed in search of significant features. Traces were taken in air (green), open circuit in 1.0M NaOH electrolyte (black) and at closed circuit, 0V vs. Ag/AgCl (blue) with Pt counter electrode. The figure above confirms that there are no additional features in the broader spectral range of 675 – 1070 cm<sup>-1</sup>. The difference in the broad background absorption between air and electrolyte above 850 cm<sup>-1</sup> was not reproducible.